

FEASIBILITY STUDY OF THE
TRANSONIC BIPLANE CONCEPT FOR
TRANSPORT AIRCRAFT APPLICATION
LG74ER0077

By

R. H. Lange
J. F. Cahill
E. S. Bradley
R. R. Eudaily
C. M. Jenness
D. G. MacWilkinson

June 1974

Prepared Under Contract NAS1-12413

By

THE LOCKHEED-GEORGIA COMPANY
A Division of the Lockheed Aircraft Corporation
Marietta, Georgia

For

NATIONAL AERONAUTICS AND SPACE ADMINISTRATION

FOREWORD

Contract NAS1-12413 between the National Aeronautics and Space Administration and the Lockheed-Georgia Company, effective June 19, 1973, provided for a preliminary study of the transonic biplane concept for transport aircraft application. Richard A. Langhans of the Aeronautical Systems Office at the Langley Research Center was the technical monitor for this contract during its initial phase. He was ably succeeded by Allen H. Whitehead, Jr., for the completion of this contract.

At the Lockheed-Georgia Company, the study was performed under the direction of Roy H. Lange, Transport Design Department Manager. J. F. Cahill had overall responsibility for the aerodynamic configuration work. Efforts in the areas of structures and design integration were under the direction of R. R. Eudaily and E. S. Bradley, respectively. Other contributors in this study included H. J. Abbey, D. P. Bierce, S. D. Higham, J. F. Honrath, C. M. Jenness, D. G. MacWilkinson, R. W. Patterson and J. S. Petkas.

Measurement values contained in this report are in both SI and customary units with the former stated first and the latter in parentheses. The principal measurements and calculations have been made in the customary system of units.

CONTENTS

	<u>Page</u>
FOREWORD	iii
SYMBOLS	viii
ABBREVIATIONS	x
ABSTRACT	xi
SUMMARY	xiii
PHASE I. INITIAL STUDY CONFIGURATIONS	1
1.0 INTRODUCTION	3
2.0 STUDY APPROACH	6
3.0 BASIC DATA AND ANALYSES	8
3.1 AERODYNAMIC CONFIGURATIONS	8
3.1.1 BASIC DATA - CRUISE	8
3.1.1.1 Biplane Theory	8
3.1.1.2 Initial Study Configuration	12
3.1.1.3 Non-Planar Lifting Surface and Induced Drag Programs	12
3.1.1.4 Parametric Studies	14
3.1.1.5 Lateral Control Requirements	28
3.1.2 BASIC AERODYNAMIC DATA - HIGH LIFT	29
3.1.2.1 Wind Tunnel Data Sources	29
3.1.2.2 Stall Matching and $C_{L_{MAX}}$ Definition	29
3.1.2.3 $C_{L_{MAX}}$ Estimation	31
3.1.2.4 High-Lift Drag	43
3.2 DESIGN INTEGRATION	43
3.2.1 INITIAL STUDY INTEGRATION	48
3.2.2 INTERIM CONFIGURATION	51
3.2.2.1 Configuration Development	51
3.2.2.2 Wing, Tip-Fin, and Vertical Stabilizer Structure	51

	<u>Page</u>
3.2.2.3 Fuselage Structures and Internal Layout	57
3.2.2.4 Flap Mechanisms	59
3.2.2.5 Landing Gear	62
3.3 STRUCTURAL ANALYSIS	62
3.3.1 DESIGN LOADS CRITERIA	65
3.3.2 STRUCTURAL MODELING CONCEPTS AND RESULTS	69
3.3.3 PARAMETRIC WEIGHT PROGRAM	73
3.3.3.1 Wing and Tip-Fin Weight	73
3.3.3.2 Vertical Tail Weight	76
3.3.3.3 Fuselage Weight	78
3.3.3.4 Surface-Controls Weight	79
3.3.3.5 Other Components Weights	79
3.3.3.6 Weight Summary	79
3.3.4 FLUTTER ANALYSIS	81
3.3.4.1 Math Model for Flutter Analysis	81
3.3.4.2 Results for Initial Study Configuration	83
3.3.4.3 Results for Configuration 5	85
4.0 CONFIGURATION STUDIES	91
4.1 SIZING AND PERFORMANCE PROGRAM	91
4.2 PARAMETRIC STUDY RESULTS	91
PHASE II. REVISED STUDY PROGRAM	97
1.0 RE-DEFINED STUDY PLAN	99
2.0 ALTERNATE CONFIGURATION	100
2.1 FLUTTER CONSIDERATIONS	100
2.2 AERODYNAMIC CONFIGURATION	101
2.2.1 INDUCED DRAG ANALYSIS - ALTERNATE CONFIGURATION SELECTION	101

	<u>Page</u>
2.2.2 ANALYSIS OF ALTERNATE CONFIGURATION	101
2.2.2.1 Cruise	101
2.2.2.2 High Lift	105
2.2.2.3 Lateral/Directional Stability	109
3.0 STRUCTURAL ANALYSIS	113
3.1 STRENGTH	113
3.2 WEIGHTS	113
3.3 FLUTTER ANALYSIS	115
3.4 FUNDAMENTAL FLUTTER PHENOMENA	116
4.0 COMPARISON WITH ATT $M = 0.95$ CONFIGURATION	122
5.0 RESEARCH AND TECHNOLOGY RECOMMENDATIONS	123
REFERENCES	125

SYMBOLS

AR	Aspect ratio
b	Wing span, meters (feet)
b_1, b_2	Span of upper and lower wings, respectively, meters (feet)
\bar{c}	Mean aerodynamic chord, meters (feet)
\bar{c}_1, \bar{c}_2	Mean aerodynamic chord for upper and lower wings, respectively, meters (feet)
\bar{c}_{avg}	Average mean aerodynamic chord, meters (feet)
C_D	Total drag coefficient
C_{D_i}	Total induced drag coefficient
$C_{D_{i\ min}}$	Minimum induced drag coefficient
C_L	Total lift coefficient
C_{L_1}, C_{L_2}	Lift coefficient for upper and lower wings, respectively
$C_{L_{max}}$	Maximum total lift coefficient
$C_{L_{\alpha_1}}, C_{L_{\alpha_2}}$	Lift-curve slope of the upper and lower wings, respectively
C_l	Section lift coefficient
C_{l_β}	Change in rolling moment with change in sideslip angle, newton-meters/radian (foot-pounds/degree)
C_m	Total pitching moment coefficient
C_{m_0}	Zero-lift pitching moment coefficient
$C_{m_{o_1}}, C_{m_{o_2}}$	Zero-lift pitching moment coefficient for upper and lower wings, respectively
C_{n_β}	Change in yaw moment with change in sideslip angle, newton-meters/radian (foot-pounds/degree)

$C_{y\beta}$	Change in side force with change in sideslip angle, newtons/radian (pounds/degree)
D_i	Induced drag, newtons (pounds)
$D_{i\min}$	Minimum induced drag, newtons (pounds)
E	Tensile modulus of elasticity, newtons/meter ² (pounds/foot ²)
G	Shearing modulus of elasticity, newtons/meter ² (pounds/foot ²)
h	Vertical displacement between wings, meters (feet)
h_n	Neutral point position, meters (feet)
h_{o1}, h_{o2}	Neutral point position for the upper and lower wings, respectively, meters (feet)
h_{xx}	Radius of gyration, meters (feet)
Δh_n	Static margin, percent
I	Moment of inertia, meter ⁴ (foot ⁴)
J	Polar moment of inertia, meter ⁴ (foot ⁴)
K	Lift-curve-slope ratio
K_Λ	Sweep angle factor
L	Total lift, newtons (pounds)
L_1, L_2	Lift force on upper and lower wings, respectively, newtons (pounds)
L/W	Lift to gross weight ratio per unit span
L_1/W	Lateral lift to gross weight ratio per unit span
l_A	Distance between the lift forces on the forward and aft wings, meters (feet)
l_2	Distance between leading edges of forward and aft wings, meters (feet)
M	Mach number
R_N	Reynolds number
S	Total biplane wing area, meter ² (foot ²)

S_1, S_2	Area of upper and lower wings, respectively, meter ² (foot ²)
T	Thrust, newtons (pounds)
t	Wing surface material thickness, meters (feet)
\bar{t}	Equivalent wing surface material thickness, meters (feet)
V	Velocity, meters/second (feet/second)
W	Gross weight, kilograms (pounds)
W/S	Wing loading, kilograms/meter ² (pounds/foot ²)
x	Distance measured upward on vertical fin, meters (feet)
y	Distance measured outward from wing center, meters (feet)
α	Angle of attack, radians (degrees)
α_1, α_2	Angle of attack of upper and lower wings, respectively, radians (degrees)
β	Sideslip angle, radians (degrees)
δ_f	Flap deflection angle, radians (degrees)
ϵ	Downwash angle at the rear wing, radians (degrees)
η	Wing semi-span position, $\eta = 2y/b$
η_f	Non-dimensional flap position
η_v	Fin vertical position, $\eta_v = x/h$
ρ	Density, kilograms/meter ³ (pounds/foot ³)
σ	Function of h, also, altitude ratio
Λ	Sweep angle, radians (degrees)

ABBREVIATIONS

ATT	Advanced Transport Technology
FAMAS	Flutter and Matrix Algebra System
FAR	Federal Aviation Regulations
MAC	Mean aerodynamic chord

ABSTRACT

Investigations were conducted to evaluate the feasibility of a transonic biplane consisting of a forward-mounted swept-back lower wing, a rear-mounted swept-forward upper wing, and a vertical fin connecting the wings at their tips. This wing arrangement results in significant reductions in induced drag relative to a monoplane designed with the same span, and it allows for a constant-section fuselage shape while closely matching an ideal area distribution curve for $M = 0.95$ cruise. However, no significant reductions in ramp weight were achieved for the biplane relative to a monoplane with the same mission capability. Flutter analyses of the biplane revealed both symmetric and antisymmetric instabilities that occur well below the required flutter speed. Further studies will be required to determine if acceptable flutter speeds can be achieved through the elimination of the instabilities by passive means or by active controls. Configurations designed for other missions, especially those with lower Mach numbers and lower dynamic pressures, should be examined since the geometries suitable for those design constraints might avoid the weight penalties and flutter instabilities which prevent exploitation of induced drag benefits for the configuration studied.

SUMMARY

A feasibility study of the transonic biplane concept for transport aircraft application has been conducted by the Lockheed-Georgia Company under NASA contract NAS1-12413. This novel aircraft configuration consists of a forward-mounted swept-back lower wing and a rear-mounted swept-forward upper wing connected through vertical fins at the wing tips. Because of the physical arrangement of the wings as verified by limited test results, significant reductions are expected in induced drag, trim drag, wake-vortex characteristics, and aircraft size relative to comparable monoplane configurations. Brief comparisons are made of the overall characteristics of the design evolved in this study with those of the $M = 0.95$ monoplane transport configuration developed in the Advanced Transport Technology (ATT) study by Lockheed in Contract NAS1-10701.

An initial study configuration was selected to provide a baseline for detailed engineering analyses. This initial configuration has the same cruise lift/drag ratio, cruise Mach number, payload, range, and airport performance as the $M = 0.95$ ATT monoplane. Technology and noise levels are identical for the two configurations. The initial study configuration has untapered wing planforms and 0.70 radians (40°) sweep of each wing. Parametric studies of significant configuration variables revealed that the optimum sweep combination for minimum drag corresponding to equal lift on both wings and also respecting constraints imposed by adequate longitudinal stability is 0.79 radians (45°) forward-wing sweep and -0.54 radians (-31°) aft-wing sweep. A tapered wing planform with root-chord extensions provides the minimum weight structure. The configuration arrangement allows for a constant-section fuselage shape (no indentations) and still provides a close match of the ideal area-distribution curve for $M = 0.95$ cruise.

Flutter analyses of the various configurations developed showed both symmetric and antisymmetric instabilities occurring at speeds well below the required flutter speed of 270 m/sec (525 KEAS). A configuration with the wing tip spacing reduced by one-half showed a flutter speed increase of about 25 percent over that for the initial and interim configurations but also showed a large drag increase, and was, therefore, eliminated. The interim selected configuration, while achieving ramp weights about the same as for the $M = 0.95$ ATT monoplane, also exhibited flutter instabilities that occur well below the required flutter speed.

After a review of the study results, NASA and the contractor agreed to direct the remainder of the study toward gaining a better understanding of the flutter instability phenomena and passive means for elimination of it. Limited resources allowed the complete flutter analysis of only one additional biplane configuration; selection of the additional configuration was determined on the basis of minimum induced drag. The selected alternate configuration is characterized by a rear wing with a gull-like inboard section, which allows use of that portion of the wing as a vee-tail. The alternate configuration still exhibits flutter instabilities at speeds well

below that required for a $M = 0.95$ cruise transport, and offers no advantage in ramp weight as compared to the $M = 0.95$ ATT monoplane. However, because of the nature of the instabilities, it is reasonable to assume that active controls would provide significant increases in flutter speeds.

Recommendations are presented for studies of other mission applications for which benefits of the transonic biplane concept might be larger than those shown in this report, and for R&D studies which should be conducted if those benefits are proved cost effective.

PHASE I. INITIAL STUDY CONFIGURATIONS

1.0 INTRODUCTION

Preservation of this country's lead in the development of commercial transport aircraft requires a continual enhancement of the technologies on which that development is based. Recent technological advances in a number of disciplines related to aircraft design were studied and evaluated in considerable detail by several contractors in the NASA's Advanced Transport Technology (ATT) program completed in 1972. The ATT program and other similar studies have as their primary objective the evaluation of practical benefits which can be realized from exploitation of technological advances by subjecting these advances to a close scrutiny by all of the disciplines concerned in the total aircraft design process. From the results of such evaluations, proper decisions can be made in the planning of research and development programs to assure optimum expansion of the design technology base. The basic objective of this study is to evaluate the feasibility of an unconventional aircraft concept, called the transonic biplane, to determine the worth of continuing research and development activity on this concept.

An artist's concept of the transonic biplane is shown in Figure 1. The two primary lifting surfaces are a swept-back wing attached to the lower portion of the forward fuselage and a swept-forward wing attached to the top of the vertical tail. These two wings are connected by tip fins. With such a wing arrangement, substantial reductions in induced drag below that of a monoplane configuration of the same aspect ratio are known to be possible. The capability of capitalizing on this drag reduction can only be determined by an airplane design study in which special attention is given to the practical structural and design problems of such a configuration.

The essential aerodynamic foundation for this configuration concept was established as early as 1934 when it was shown that a closed rectangular lifting system (a biplane with connecting tip fins) would produce the "smallest possible induced resistance for given span and height." (Reference 1). Drag reductions of as much as 50 percent of the monoplane induced drag (for a vertical separation between the wings equal to the semispan) are predicted in Reference 1. While that particular reference gave no consideration to wing sweep, addition of the stagger theorem of biplanes would indicate that sweep has no effect on the induced drag effectiveness. Low speed wind tunnel tests at the Lockheed-California Company (Reference 2) in 1972 confirmed these analytical results by demonstrating induced drag values matching the theory of Reference 1 for a swept biplane of the type considered in this study. High subsonic and low supersonic speed wind tunnel tests of a somewhat similar configuration were conducted by NACA (Reference 3) in 1953 but with the primary objective of eliminating pitch-up at high lift coefficients. Vertical separation between the two wings in that case was quite small, and no drag advantage was observed, nor would it have been predicted by the theory.

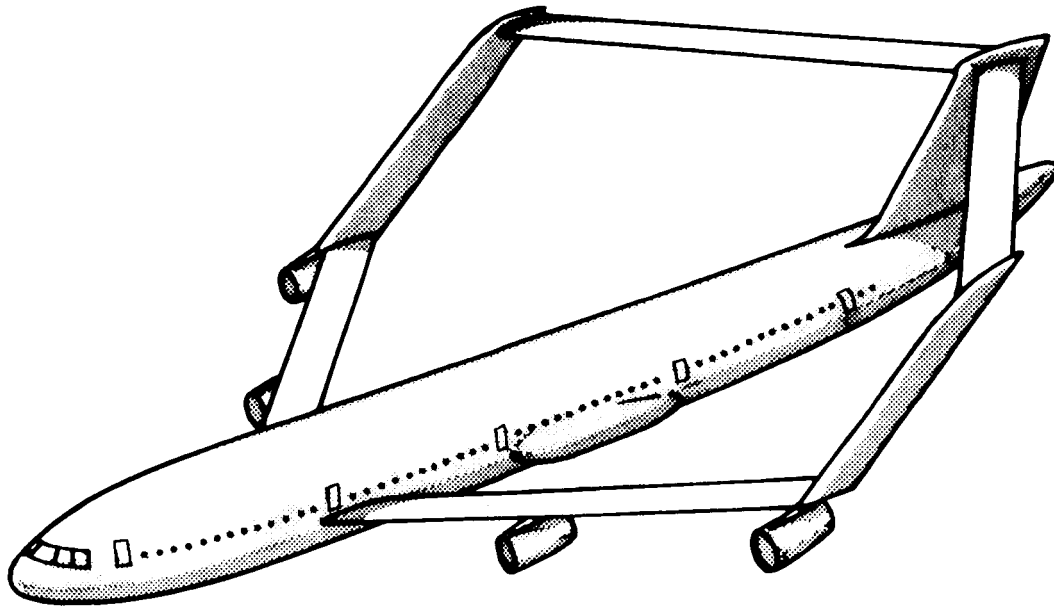


Figure 1. Transonic Biplane Concept.

In addition to the substantial reduction in drag demonstrated for the transonic biplane concept, several other aerodynamic advantages can be anticipated and are listed here.

- o Since the rear wing is in the downwash field of the forward wing, it will stall later and, therefore, insure nosedown pitching moments.
- o Since sweep-forward and sweep-back effects tend to compensate each other, the objectionable increase of dihedral effect with lift coefficient is avoided.
- o Fuselage indentation requirements for area ruling are substantially reduced from those for a monoplane wing.
- o For flight at supersonic speed, wave drag will be reduced because of the greater longitudinal spread of the lift distribution.
- o Community noise reduction can be anticipated because of an improved lift-to-drag ratio during take-off and landing.

This study was undertaken to determine the feasibility of using this unconventional wing arrangement in the design of a high subsonic-speed transport aircraft and to quantify any ensuing benefits. Design objectives for the transonic biplane were the same as those for the final configuration developed in the Lockheed-NASA

ATT study (Reference 4) to facilitate a determination of benefits through direct comparisons. These design objectives are as follows:

- o Range: 10 186 kilometers (5500 nautical miles)
- o Payload: 400 passengers
- o Cruise speed: Mach number of 0.95
- o Runway length: 3048 meters (10 000 feet) or less

Such advanced technologies as supercritical wings, composite structures, and advanced engines which were considered in the ATT studies, were used in this study also.

2.0 STUDY APPROACH

A broad outline of the Transonic Biplane Feasibility Study is indicated by the block diagram shown in Figure 2. An initial study configuration was selected at the start of the program to provide a baseline for conduct of detailed engineering analyses. This initial configuration was established by utilizing existing aerodynamic information to define a biplane wing having the same area and lift-to-drag ratio as the ATT airplane (Reference 4) which was to be used as a basis for comparison. Extensive engineering analyses were conducted on this biplane configuration, first to obtain a complete assessment of the configuration, and second to provide a base for subsequent configuration studies.

With the objective of developing a minimum-weight configuration for the design mission, a parametric study was made of those configuration characteristics which have a significant influence on airplane performance. It was initially planned that the configuration selected during the parametric study would be subjected to rather intensive refinement in order to best display benefits for this configuration concept. As the program developed, however, results dictated that the latter portion of the study be devoted to a search for configuration modifications which might eliminate flutter instabilities disclosed by analyses of the initial configurations. Since no satisfactory solution for flutter instabilities was obtained, no selection of a final configuration was possible, and comparisons of performance capabilities with the ATT results were minimized.

Because of the complexity of the transonic biplane configuration, proper assessments of airplane characteristics utilizing this concept can only be accomplished by use of rather elaborate analytical procedures for aerodynamic, structural loading, and aeroelastic characteristics. Computer programs developed for previous studies were utilized for these purposes with only minor modifications to recognize the characteristics of the transonic biplane concept. Basic aerodynamic data from rather scant experimental programs confirm the analytical results quite well with respect to basic aerodynamic characteristics and airload distributions. In the structures areas, no experimental data are available for correlation, but the analytical techniques incorporated in the computer programs can be relied upon to produce results suitable for this feasibility evaluation.

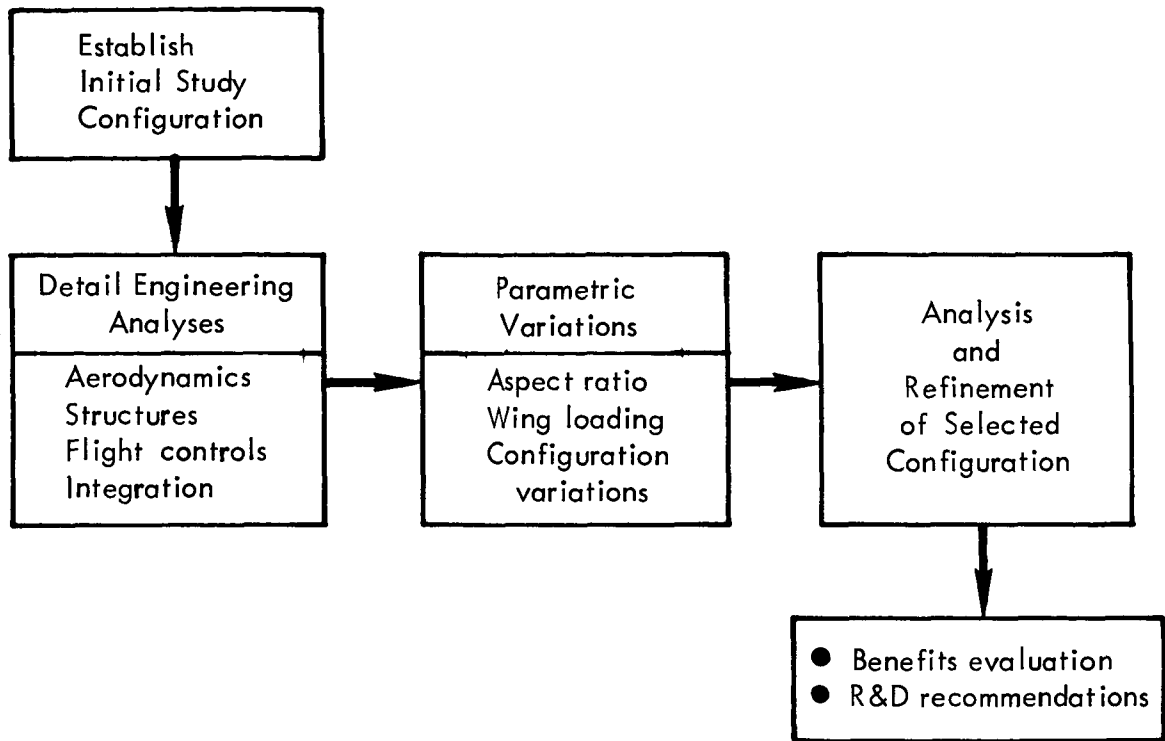


Figure 2. Proposed study program outline.

3.0 BASIC DATA AND ANALYSES

The three principal technical disciplines which form the background to this study are those of aerodynamics, design integration, and structural analysis. Development of the optimum transonic biplane configuration was planned to proceed from an initial study configuration, and to be attained through inputs from parametric studies in cruise aerodynamics, airport performance, initial structural design concepts and overall layout design. The fundamental approach and methodology used in each of the three technical areas and the analyses of transonic biplane characteristics are discussed in this section.

3.1 AERODYNAMIC CONFIGURATIONS

3.1.1 BASIC DATA - CRUISE

Although classical biplane theory is well established and has been available for many years, the application to a long-range cruise configuration to operate at transonic speeds is entirely new. Therefore, the approach to this feasibility study is to use established biplane theory, in particular the known benefits to induced drag, together with theoretical computer programs for non-planar lifting systems. While some low-speed wing tunnel data are available from tests on a closed-biplane arrangement, no experimental data exist for the unique, fully optimized biplane arrangement being considered in this study. Determining the feasibility and merits of the transonic biplane design are the prime objectives of this study.

3.1.1.1 Biplane Theory

Since the fundamental aerodynamic characteristic of this concept is the reduction in induced drag offered by the biplane arrangement, biplane theory is briefly reviewed in order to point out the pertinent factors which influence configuration selection.

Early work by Prandtl and Munk (References 1 and 5) established the theoretical aspects of biplane wings. It can be shown from Prandtl's theory that the total vortex induced drag, D_i , of an unstaggered biplane system, shown in Figure 3, can be written as

$$D_i = \frac{2L_1^2}{\pi b_1^2 \rho V^2} + \frac{2L_2^2}{\pi b_2^2 \rho V^2} + \frac{4\sigma L_1 L_2}{\pi b_1 b_2 \rho V^2} \quad (1)$$

where the 3rd term represents the mutual interference between the trailing vortices of each system. The factor σ can be shown to be a function of the vertical displacement, h , between the wings and the spans, b_1 and b_2 , of the upper and lower wings, respectively. For a given total lift, where $L = L_1 + L_2$, the total vortex induced drag is a minimum when

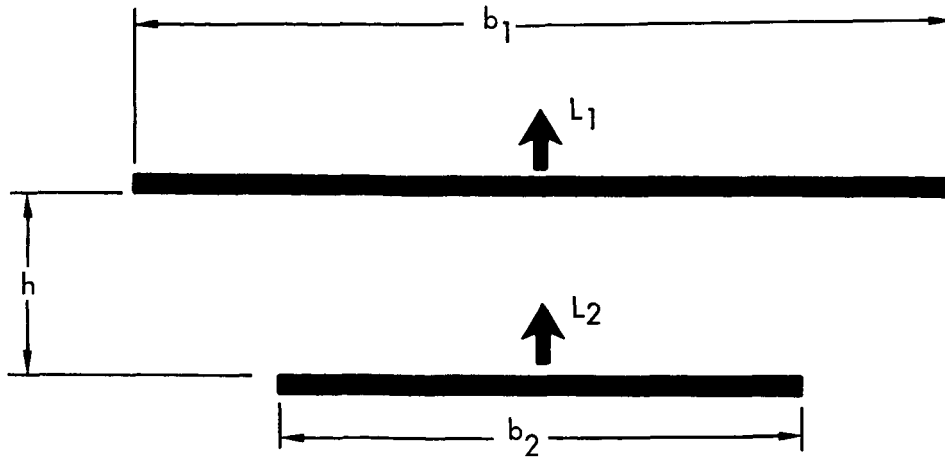


Figure 3. General biplane system schematic.

$$\frac{L_1}{L_2} = \frac{b_1(b_1 - \sigma b_2)}{b_2(b_2 - \sigma b_1)} \quad (2)$$

or, when $b_1 = b_2$ and consequently

$$L_1 = L_2 \quad (3)$$

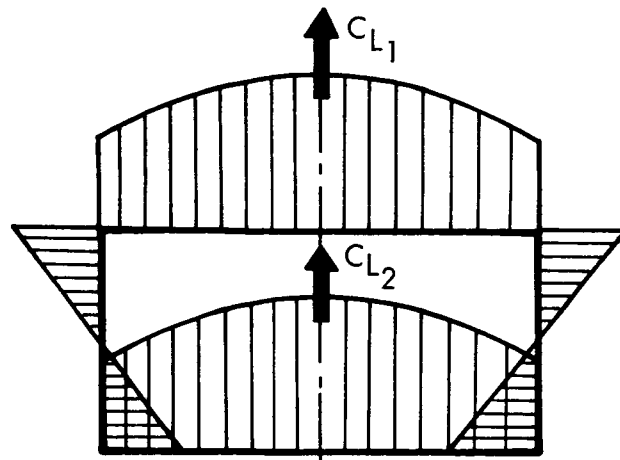
Then, the minimum induced drag, $D_{i \min}$, can be expressed as

$$D_{i \min} = \frac{2L^2}{\pi b^2 \rho V^2} \frac{(1 + \sigma)}{2}$$

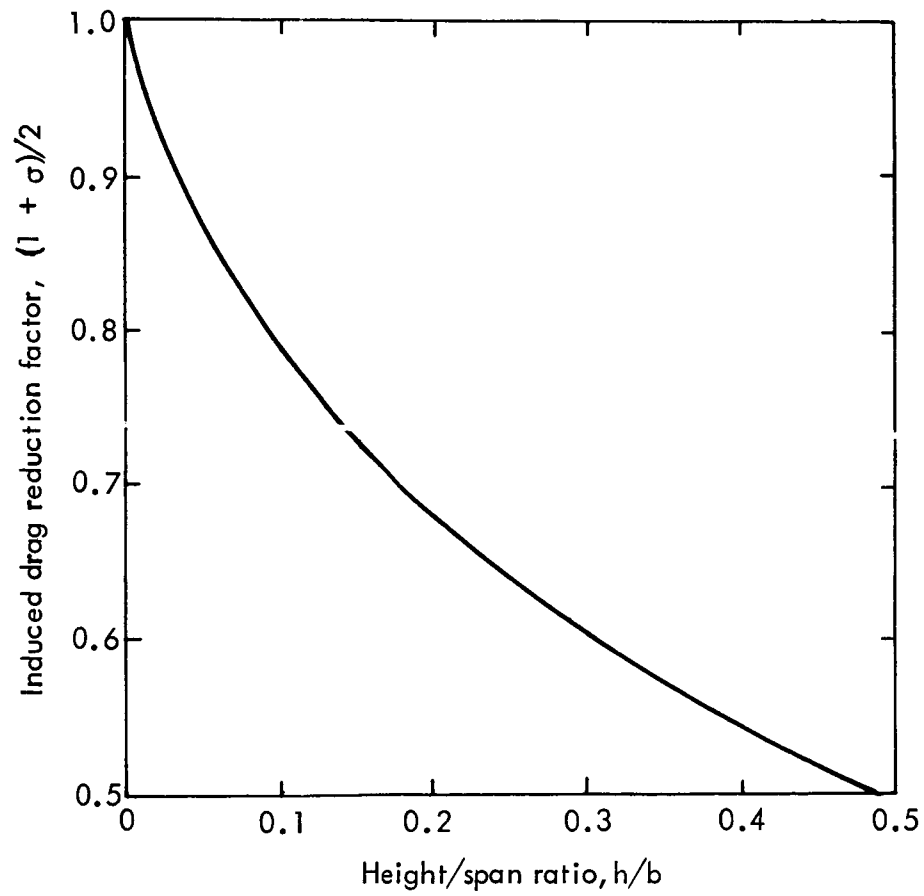
or in coefficient form by

$$C_{D_{i \min}} = \frac{C_L^2}{\pi AR} \frac{(1 + \sigma)}{2} \quad (4)$$

where AR is the total aspect ratio of the lifting system. From equation (4) it is seen that if a biplane arrangement has the same total aspect ratio and lift coefficient as a monoplane, the induced drag is reduced by the factor $(1 + \sigma)/2$. Reference 1 shows that the optimum solution for minimum induced drag is that of the closed-box arrangement. Figure 4a shows a front view of two equal-span lifting surfaces joined at the tips by vertical surfaces of length h. As the gap between the wings increases, the load distributions become more uniform. This is because the forces on the end fins are effective in reducing the conventional trailing vortices which would appear at the wing tips if they were not joined. Figure 4b shows the significant reductions in



a) Biplane lift distribution



b) Effect of biplane geometry on drag reduction

Figure 4. Closed biplane lift distribution and drag reduction.

induced drag that can be obtained with the closed biplane arrangement. For example, for a height/span ratio of 0.3, the value of induced drag is only 60 percent of that for an equivalent monoplane with the same aspect ratio.

Implied in the theoretical analysis for minimum induced drag is an optimum load distribution which produces equal values of load on each wing and a corresponding load for the tip fins. Reference 6 gives such a wing load distribution which is reproduced in Figure 5. Sensitivity studies on the induced drag penalties incurred due to deviations from these criteria are given in Section 3.1.1.4.

The generalized theory for unstaggered biplanes can be extended to staggered cases through use of Munk's equivalence theorem (Reference 5), which states that the total induced drag of any multiplane system is unaltered if any of the lifting elements are moved in the direction of motion, provided the lift distribution remains constant. By staggering the wings, the induced flow between the wings automatically changes, with the forward wing experiencing an upwash while the aft wing is subject to a downwash field. As a result, the installed lift-curve slope of the aft wing will be less than the forward wing for identical geometries. Studies of methods to achieve equal lift between the wings are reviewed in Section 3.1.1.4.

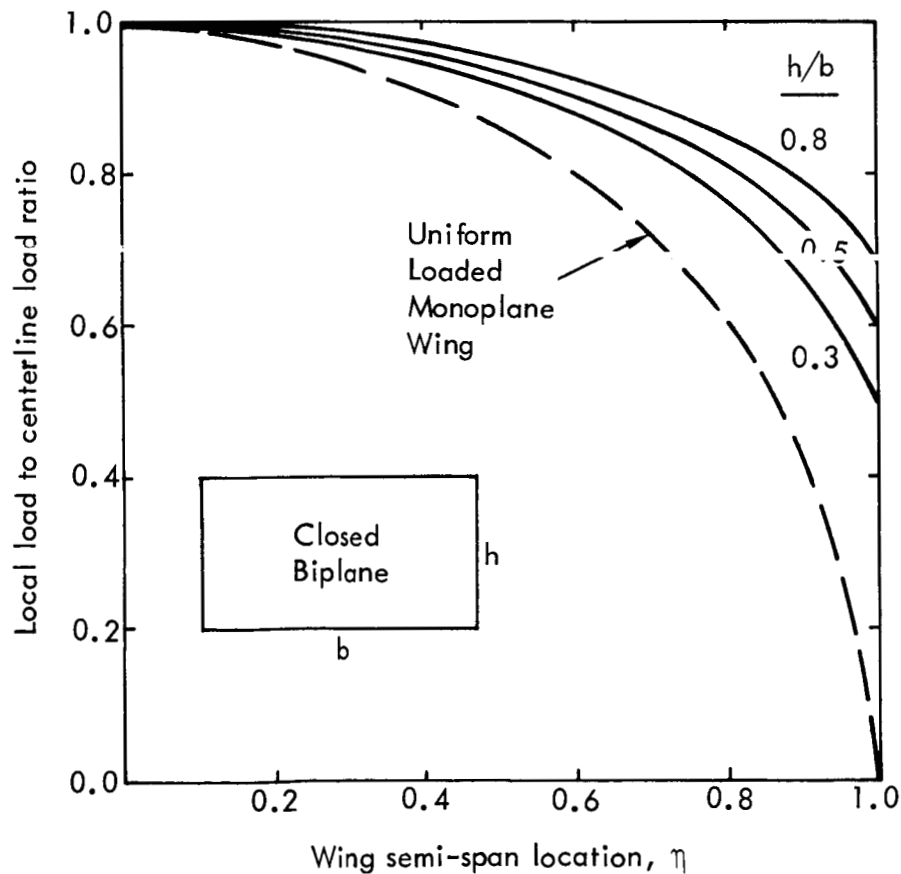


Figure 5. Optimum load distribution for minimum induced drag.

3.1.1.2 Initial Study Configuration

Figure 6 presents a three-view arrangement of the initial study configuration. In order to establish this initial arrangement, the biplane was configured to have the same cruise lift-to-drag ratio as the Lockheed M = 0.95 ATT monoplane. Drag coefficients were evaluated for both configurations for equal wing loadings during cruise. Corrections were made to the monoplane data to account for differences in zero-lift drag due to different wetted areas of the monoplane horizontal stabilizer and biplane end-fins, and to include the differences in wing-chord Reynolds numbers. The 4.12 equivalent aspect ratio of the biplane was then obtained using equation (4) in Section 3.1.1.1, assuming a value of 0.30 for the wing-tip vertical-displacement/wing-span ratio. The total wing area of the biplane is equal to that of the ATT configuration and the two wings of the biplane are of equal areas. The arrangements of the wings, nacelles, vertical tail, and landing gear were developed primarily to satisfy the following objectives:

- o Obtain the best match to an ideal area distribution with a cylindrical fuselage
- o Achieve a minimum static margin of 3 percent
- o Minimize the center-of-gravity spread

3.1.1.3 Non-Planar Lifting Surface and Induced Drag Programs

The development of an optimized closed-boxplane configuration was accomplished by using two theoretical computer programs which had previously been developed by the Lockheed-Georgia Company especially for non-planar lifting systems. Total loads were calculated based on vortex collocation lifting-surface theory.

Figure 7 shows a typical representation of the biplane layout. The wings, end fins and fuselage are approximated by flat-plate panels which are in turn divided into a series of multiple plates. Each plate is then represented by a constant-circulation bound vortex of span equal to the plate width and located at the quarter chord of the plate. This theory is essentially an extension of the non-planar theory presented in Reference 7. A fundamental assumption in the present theory is that the vortex panel is assumed to be a stream surface with the vortex sheet rigid and trailing aft in the direction of the stream surface.

Preliminary correlation studies were made between experimental and theoretical data on a simplified closed-biplane configuration in order to validate the lifting-surface theory for the current studies. The experimental data available were from the Lockheed-California Company (Reference 2), where low-speed wind tunnel tests were made on a non-optimized configuration primarily to substantiate the induced-drag benefits from this arrangement. Figure 8 presents the geometrical layout of the model. It has a forward-mounted, constant-chord, swept-back wing of 0.61 rad (35°) sweep that is joined by tip fins to a 0.37 rad ($21^\circ 8'$) swept-forward wing mounted on top of

Wing area: 442.58 m² (4764 ft²)
 T.O.G.W.: 302 283 kg (666 424 lb)
 Operating weight: 128 083 kg (282 376 lb)
 Payload 38 465 kg (84 800 lb)

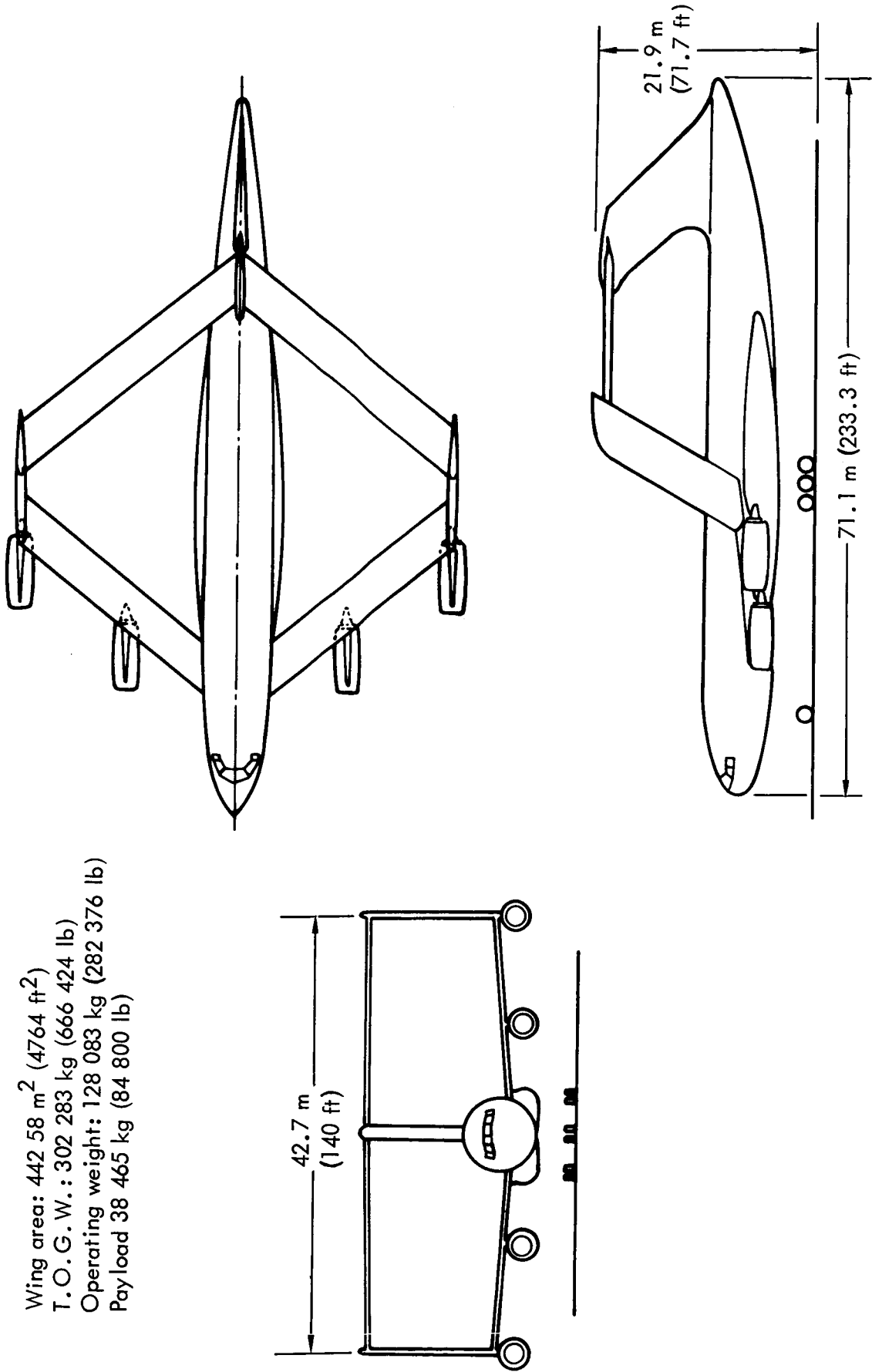


Figure 6. Initial study configuration.

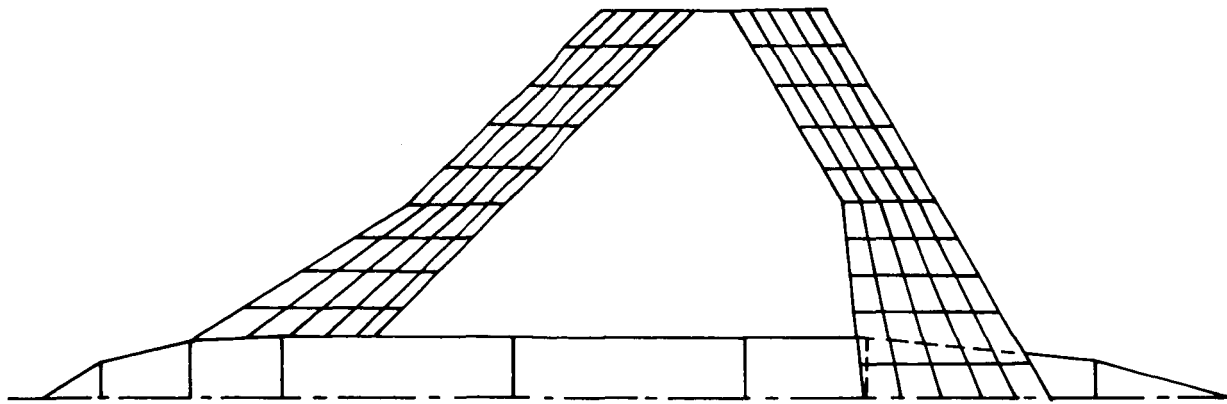


Figure 7. Panel representation for lifting surface theory computations.

a vertical fin. Both wings incorporated NACA 6409 sections, but were of zero twist. The total aspect ratio was 2.5, and the wing height/span ratio was 0.35.

Examples of force and loads data for this configuration were computed by the vortex-collocation program and are presented in Figure 9. The end fin and fore and aft wing contributions to the total load at zero angle of attack are shown in Figure 9a. Figure 9b depicts the biplane lift distribution for changes in angle of attack. Comparisons of theoretical and experimental data for lift and pitching moment are given in Figure 10. The effects on lift of decalage angle, that is, the relative incidence setting between the two wings, appear to be reasonably well predicted by the theory, although the angles for zero lift are in poor agreement due to an incomplete simulation of the fuselage and wing camber lines and the lack of any viscous corrections to the theory. Results from the pitching moment computations, presented in Figure 10, indicate that the initial stability level is reasonably well predicted, particularly with the body represented. The good agreement in the increment due to decalage angle is of significance since it indicates that the theory accounts for a realistic downwash pattern and load distribution between the two wings.

The second computer program used in this analysis was the Lockheed-Georgia method for calculating induced drag of multi-planar lifting systems.

3.1.1.4 Parametric Studies

A detailed study was conducted to establish a data base for selection of a refined configuration. Parametric variations in a number of basic parameters were developed, notably the wing planform geometries in order to establish optimum neutral point, trim drag and cruise induced drag.

Induced Drag Sensitivity to C_{L1}/C_{L2} - Equation (1) in Section 3.1.1.1 can be reduced to coefficient form for the general case as

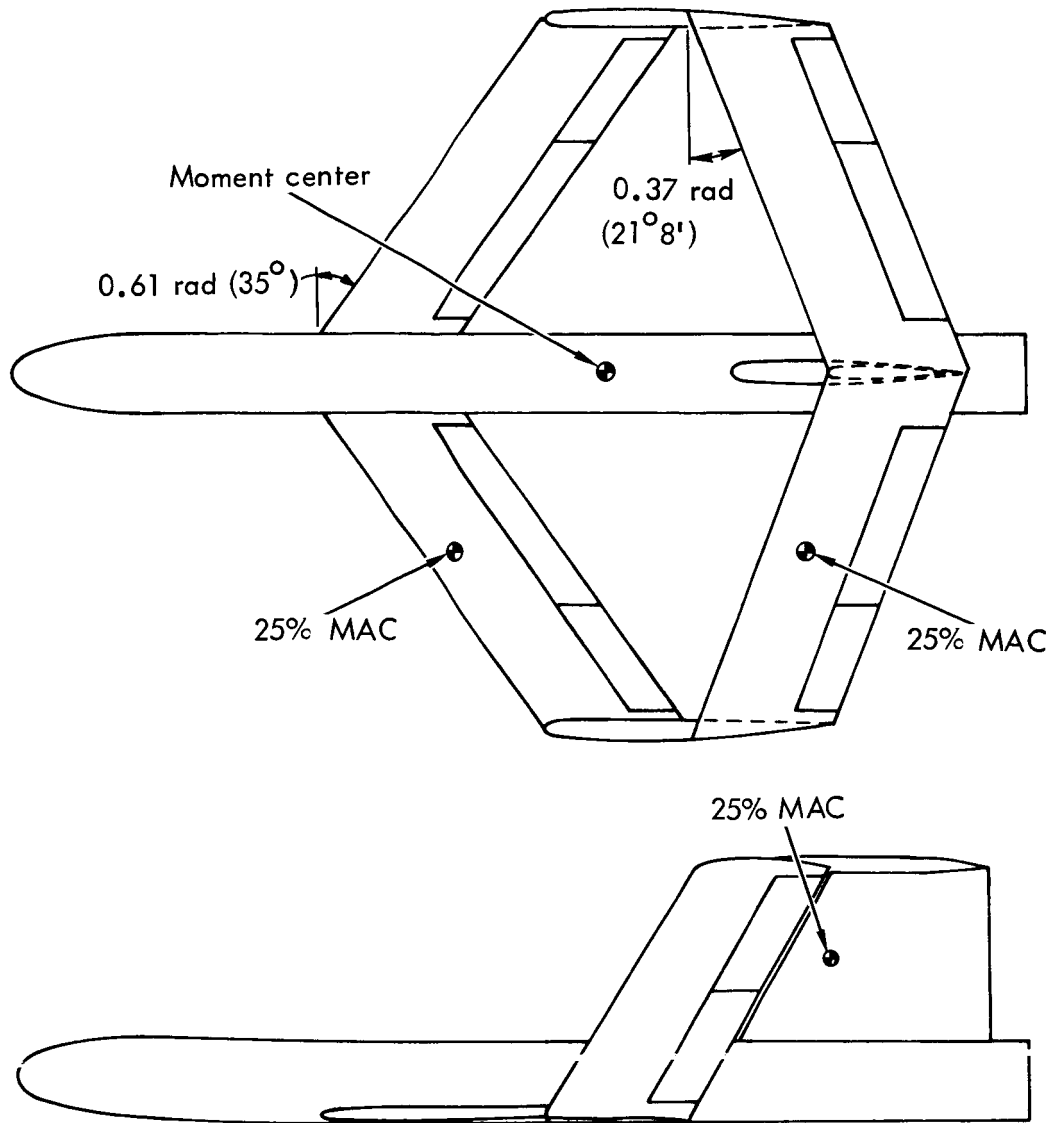


Figure 8. Boxplane wind tunnel model.

$$C_{D_i} = \frac{1}{\pi AR} (C_{L_1}^2 + C_{L_2}^2 + 2\sigma C_{L_1} C_{L_2}) \quad (5)$$

By combining equations (4) and (5), the incremental induced drag relative to the ideal case (for which $C_{L_1} = C_{L_2}$) can be expressed as

$$\frac{C_{D_i}}{C_{D_{i \min}}} = \frac{2(C_{L_1}^2 + C_{L_2}^2 + 2\sigma C_{L_1} C_{L_2})}{C_L^2 (1 + \sigma)} \quad (6)$$

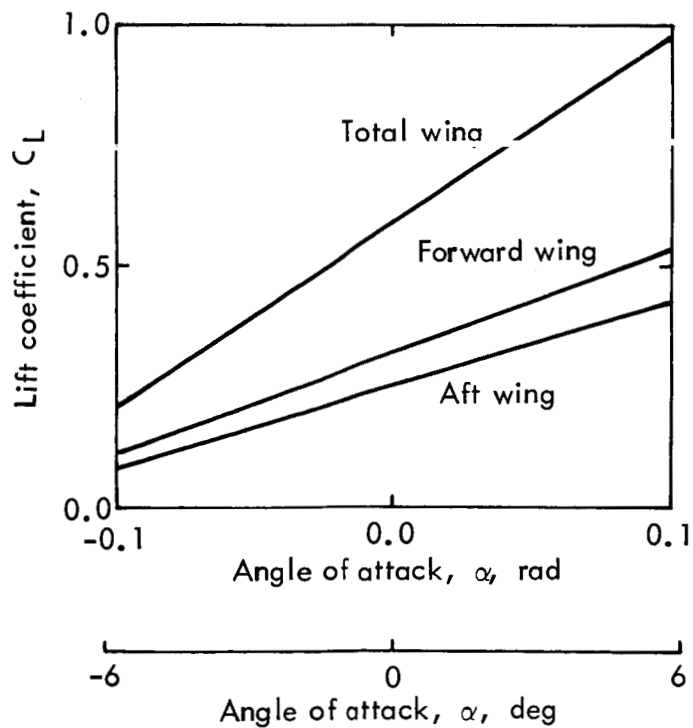
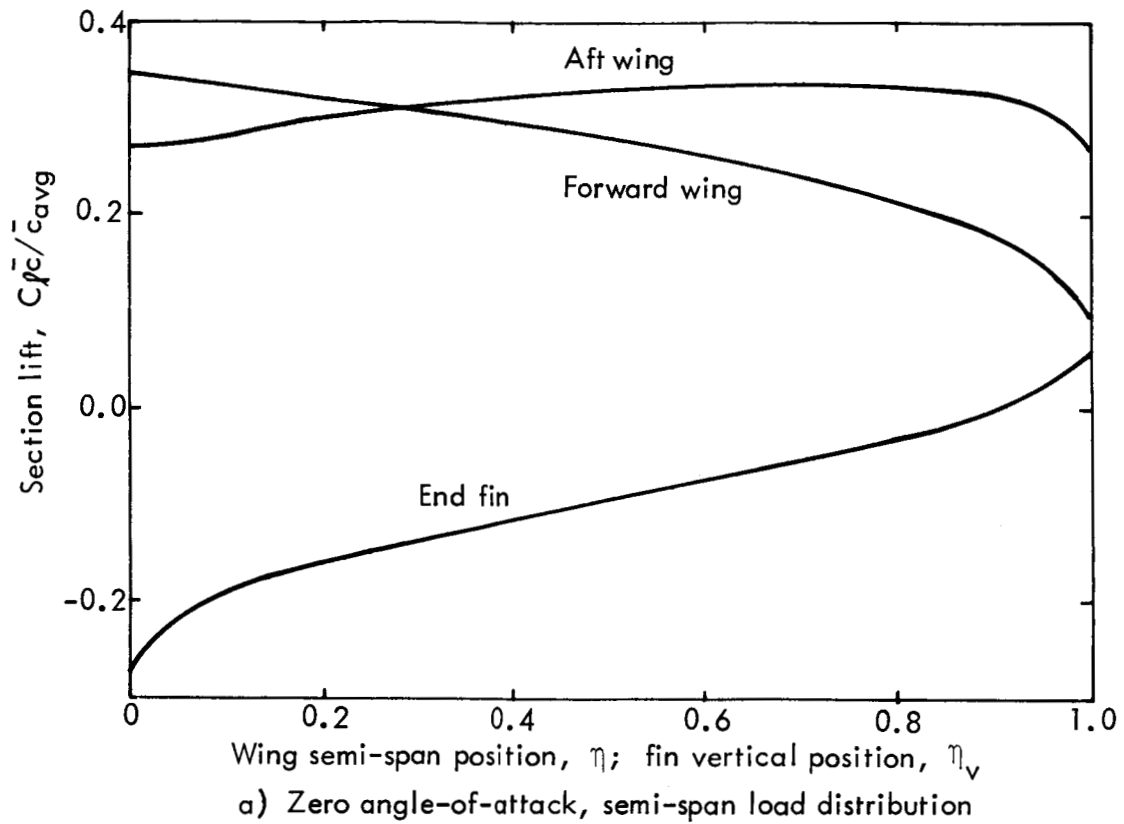


Figure 9. Boxplane configuration aerodynamic characteristics.

Theoretical:

Experimental:

Wing alone ——— 0(0)
 - - - - - 0.05(-3)
With body - - - - - 0(0)

□ 0(0)
○ -0.05(-3)
△ -0.10(-6)

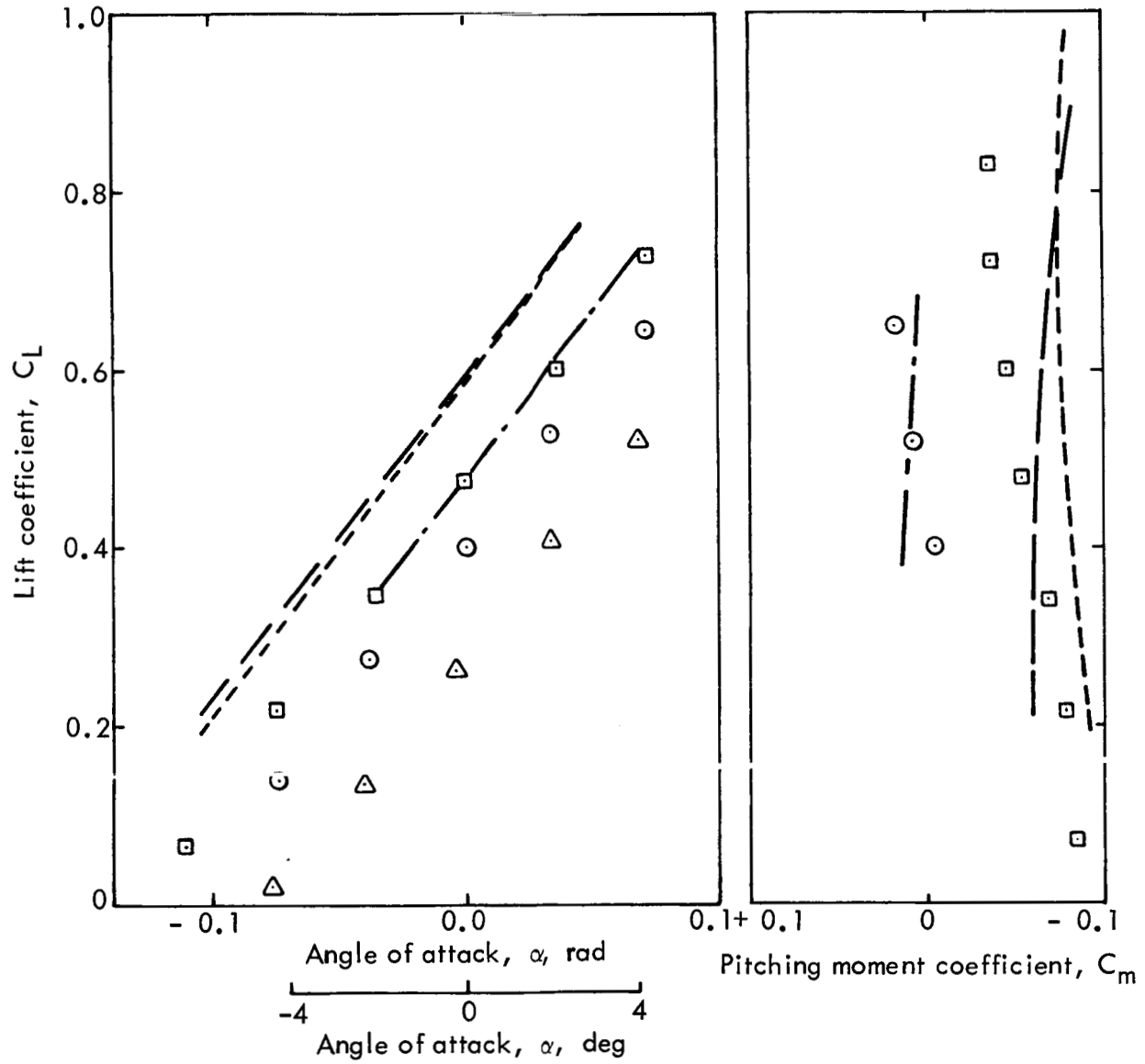


Figure 10. Correlation of theory with test data for boxplane, $M = 0.2$.

Optimum span-load distributions are assumed for both conditions. Figure 11 shows the sensitivity of the induced drag ratio to variations in lift distribution for different wing displacement geometries. This figure shows that increases up to 40 percent above the optimum lift-coefficient ratio incur only a two-percent penalty in induced drag. This has significance with respect to off-design conditions, since neutral point and trim drag considerations dictate equal loads at cruise.

Neutral Point & Trim - The basic longitudinal static stability was assessed in order to determine the influence of parameters such as lift-coefficient ratio and basic zero-lift pitching moment coefficient. Referring to Figure 12, it can be shown that the neutral point position, h_n , in terms of total mean aerodynamic chord, \bar{c} , is

$$h_n = h_{o_1} + \frac{(l_2 + h_{o_2} \bar{c}_2 - h_{o_1} \bar{c}_1)(1 - \partial \epsilon / \partial \alpha) C_{L\alpha_2} / C_{L\alpha_1}}{1 + (1 - \partial \epsilon / \partial \alpha) C_{L\alpha_2} / C_{L\alpha_1}} \quad (7)$$

The balance between static margin, Δh_n , and zero-lift pitching moment coefficient, C_{m_o} , is given by the equation

$$\frac{\Delta h_n - C_{m_o} / 2C_L}{l_A / \bar{c}_1} = \frac{(1 - \partial \epsilon / \partial \alpha) C_{L\alpha_2} / 2C_{L\alpha_1}}{1 + (1 - \partial \epsilon / \partial \alpha) C_{L\alpha_2} / C_{L\alpha_1}} - 0.25 \quad (8)$$

The graphical representation of equation (8) on Figure 13 points out that positive values of the zero-lift pitching moment coefficient are necessary to meet the requirement for equal lift on both wings for a static margin of five percent. In more specific terms, the range of C_{m_o} / C_L for a value of $l_A / \bar{c} = 5.0$ and a five-percent margin is given in Figure 14 for wings of equal area. Figure 14a shows that for values of the lift-coefficient ratio, C_{L_1} / C_{L_2} , close to unity, high values of the installed lift-curve-slope ratio, K , are desirable if the balance in longitudinal stability is to be achieved with realistic values of the zero-lift pitching moment coefficient. Two important facts are pointed out on Figure 14b. As the ratio of lift-curve slopes increases, the neutral-point location moves rearwards, and, also, the effect of varying the wing area ratio is small. Studies were next conducted to determine the effects of increasing the lift-curve-slope ratio through an increase in forward-wing sweep and a reduction in aft-wing sweep. It was assumed for the purpose of these preliminary studies that a satisfactory value of the zero-lift pitching moment coefficient could be obtained during design refinement through the application of wing twist and a wing leading-edge glove similar to that developed for the ATT configuration.

Sweep Studies - Results from lifting-surface theory computations with differing fore and aft-wing sweep combinations are given in Figure 15. These configurations are for a family of sweep combinations with a constant end-fin sweep of 0.52 rad (30°). Results are summarized in Figure 16 for extreme ends of the speed range. The optimum sweep combination for minimum drag (that is when $C_{L_1} / C_{L_2} = 1.0$) is seen to be close

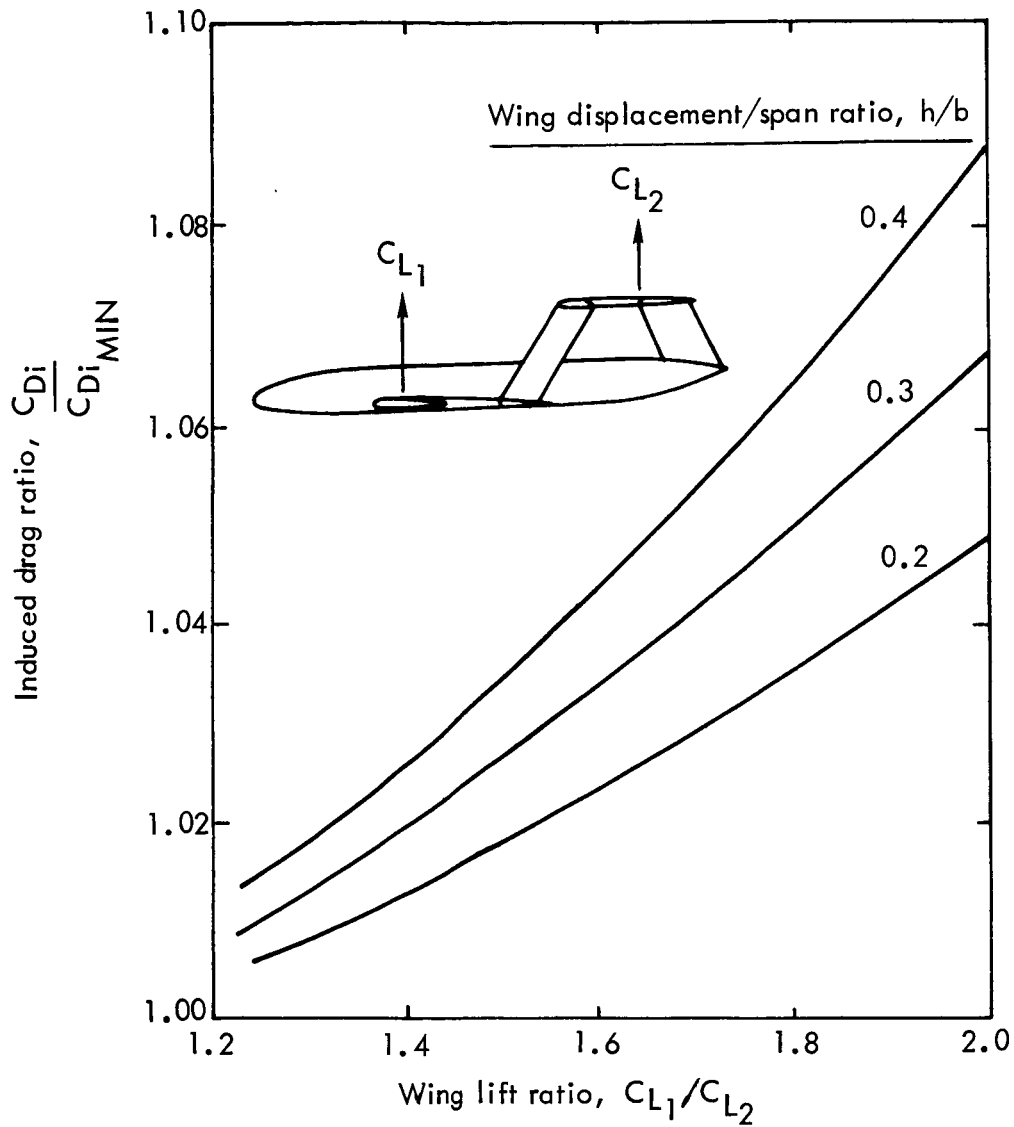


Figure 11. Sensitivity of induced drag to non-optimum lift distributions.

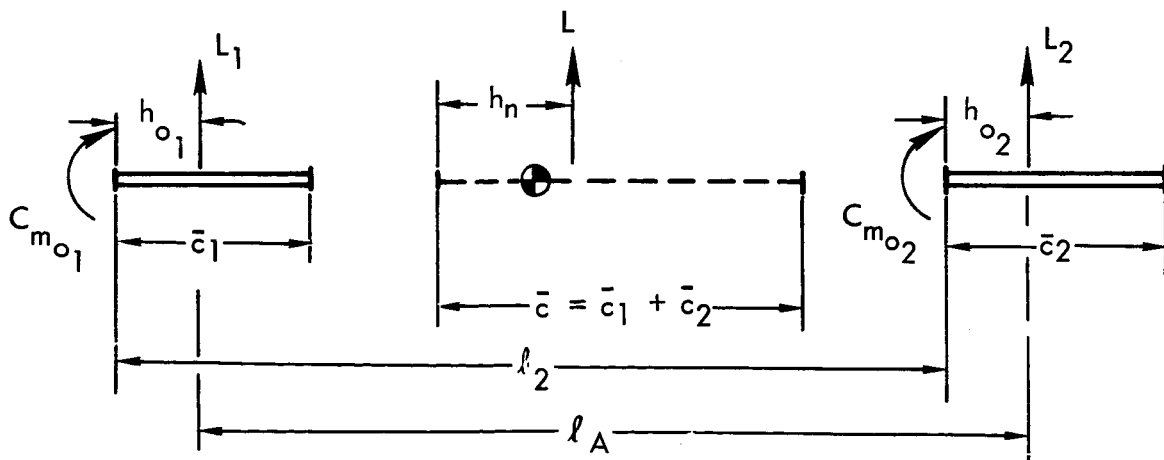


Figure 12. Force and moment representation.

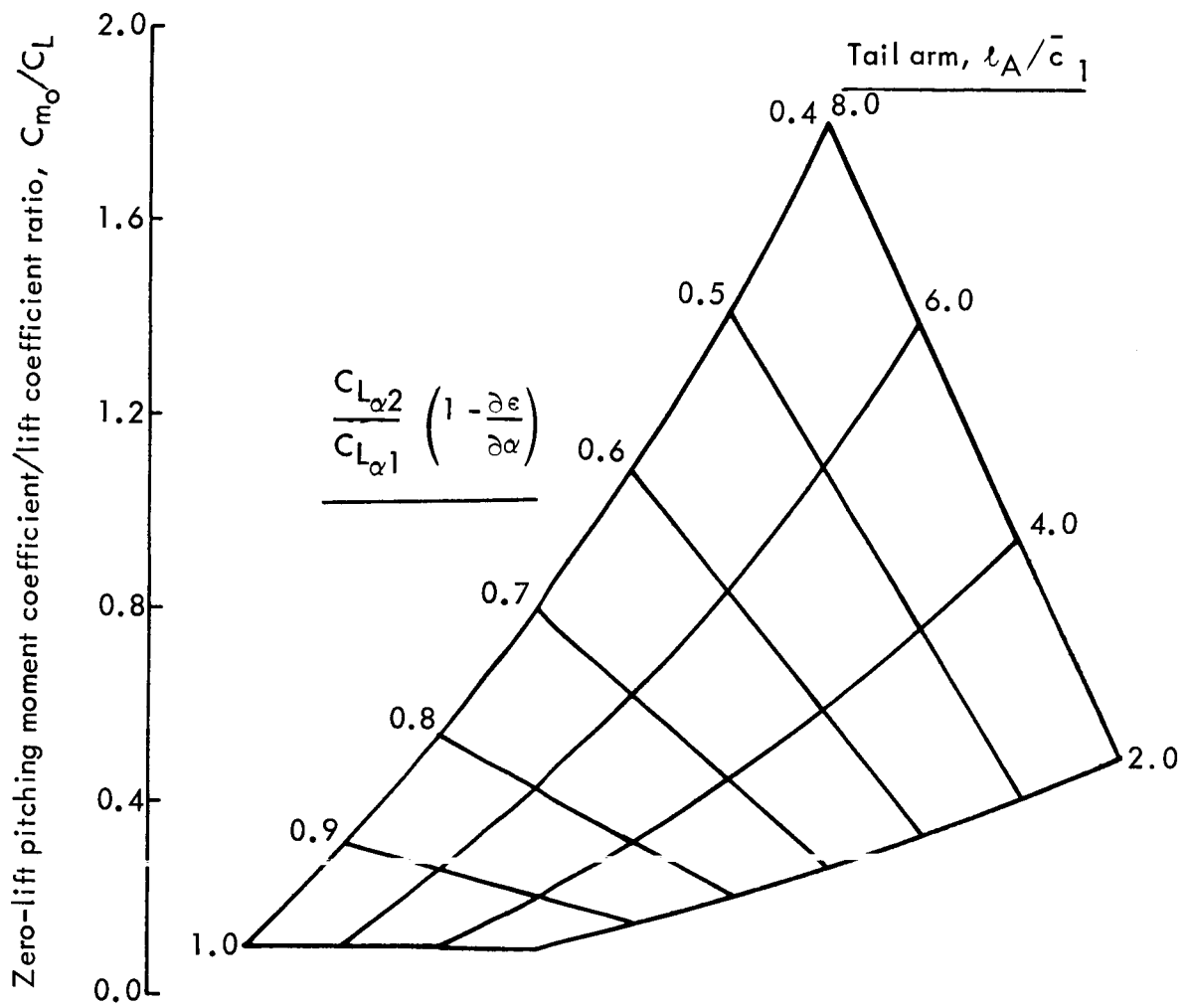


Figure 13. C_{m_0}/C_L required for trim, 5% static margin, $C_{L_1} = C_{L_2}$,
 $MAC = \bar{c}_1 + \bar{c}_2$.

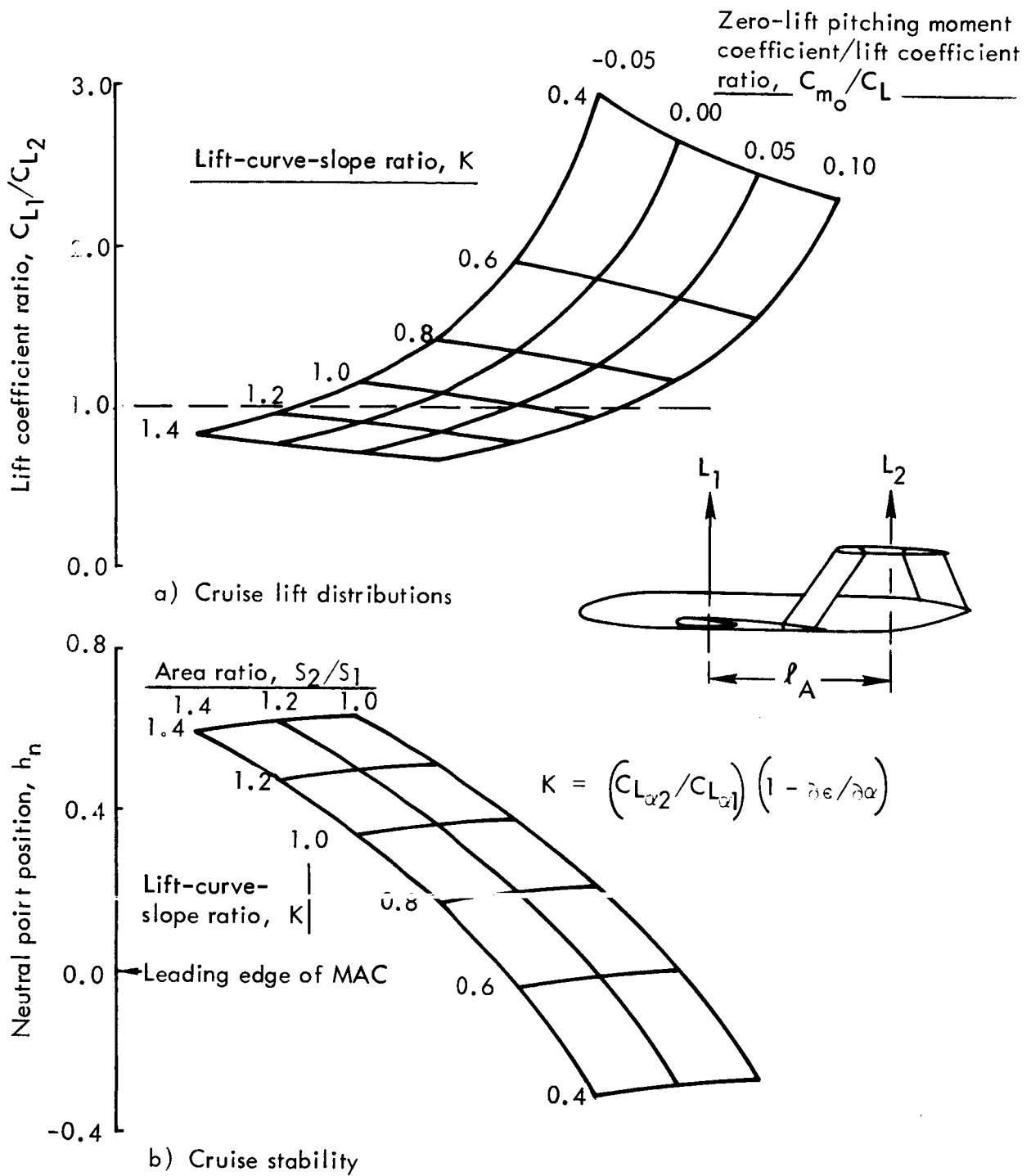


Figure 14. Aerodynamic parameters for optimum cruise, 5% static margin, $l_A/\bar{c} = 3.0$.

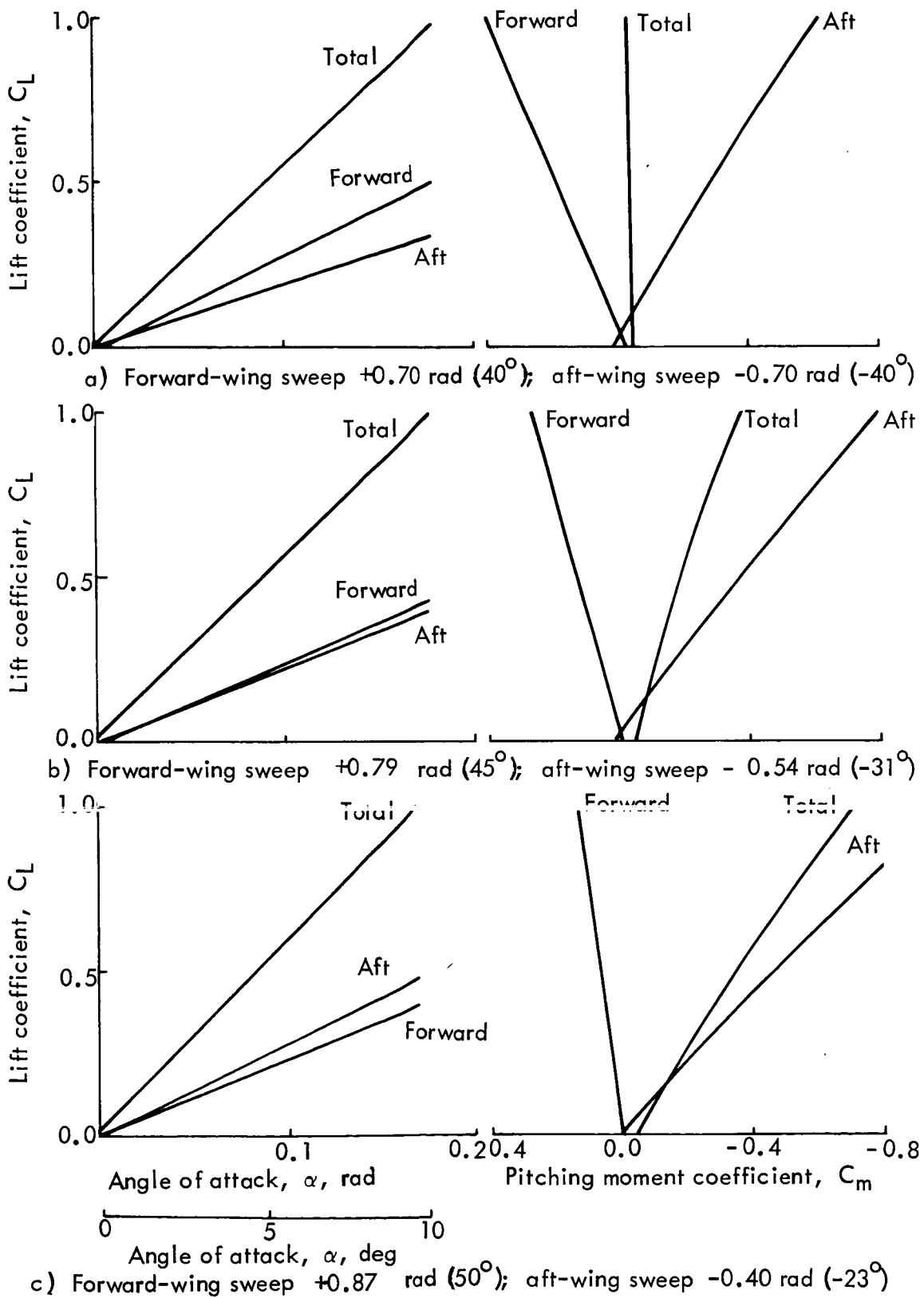


Figure 15. Effect of wing sweep on lift and pitch parameters, $M = 0.95$.

to $0.79 \text{ rad } (45^\circ)$ forward-wing sweep and $-0.54 \text{ rad } (-31^\circ)$ aft-wing sweep. The variation of neutral point with both sweep and Mach number is also shown in Figure 16. The low speed condition will determine the center of-gravity limit, but this results in a relatively large static margin at cruise because of the greater increase in lift-curve slope for the lower-sweep aft wing. In order to compensate for this adverse effect on cruise trim, it is desirable to configure the trailing-edge flap system (discussed in Section 3.2.2.4) to give full area extension of zero flap angle for all low-speed flight cases. Figure 17 indicates that the transonic neutral-point shift with Mach number is reduced from $11.5\% \bar{c}$ to $6\% \bar{c}$ with the flap area extended 20 percent of the chord. Active control systems might also be used to minimize this change in stability with Mach number

Induced Drag Studies - A series of computations was made using the non-planar induced drag program to evaluate span efficiency for a number of candidate configurations. In view of the importance of demonstrating the potential benefits from this component on biplane performance, trimmed-drag data from the wind tunnel tests of Reference 2 are presented in Figure 18. These refer to a closed-biplane configuration with a total aspect ratio of 2.5 and a wing displacement/span ratio of 0.35. Data for an equivalent monoplane with the same aspect ratio are also shown. The induced drag of the biplane test configuration closely approximates the theoretical value predicted by the theory in Reference 1. The excess drag at high lift coefficients is due to wing-flow separation at the fuselage junction, and also to a basic non-optimum span-wise load distribution which occurred since no twist was built into the wing. The difference between the induced drags of the monoplane and biplane at $C_L = 0.50$ is 210 counts or 3 percent of the total configuration drag. This drag reduction for the biplane is achieved when both configurations have the same aspect ratio. A more practical approach would be to reduce the aspect ratio of the biplane, thus giving a shorter-span configuration, while maintaining lift/drag ratios comparable to those of a monoplane.

The non-planar lifting-surface theory was used to calculate span-load distributions for the initial study configuration. Figure 19 presents an example of the load distributions for a biplane with a cruise Mach number of 0.95 and a lift coefficient of 0.45. The load distributions for both wings and the end fin are plotted on a common axis to show the relative loads carried by each. Also shown is a curve of optimum load for minimum induced drag which was derived based on the theory in Reference 6. The differences between the computed load data for zero wing twist and the idealized load suggest that a small wash-out (decreasing incidence towards the wing tip) in twist is required on the forward wing and some wash-in in twist angle (increasing incidence towards the tip) is needed on the aft wing. Also, the tip-fin should be set at some toe-in angle. Refinement of the wing, end-fin twist angles, and junction designs will be required, but no difficulty is anticipated in achieving the optimum load distributions.

The wing-span efficiencies of several biplane wing configurations are summarized in Figure 20 for optimum loading. An initial height/span ratio, h/b , of 0.27 was chosen for a box configuration with a small dihedral on the lower wing. The efficiency of 1.614 for this configuration is reduced only slightly to 1.607 when a simulated body is included. The significance of retaining a box configuration to minimize vortex intensity is illustrated by the third configuration on which the height of the tip-fins is

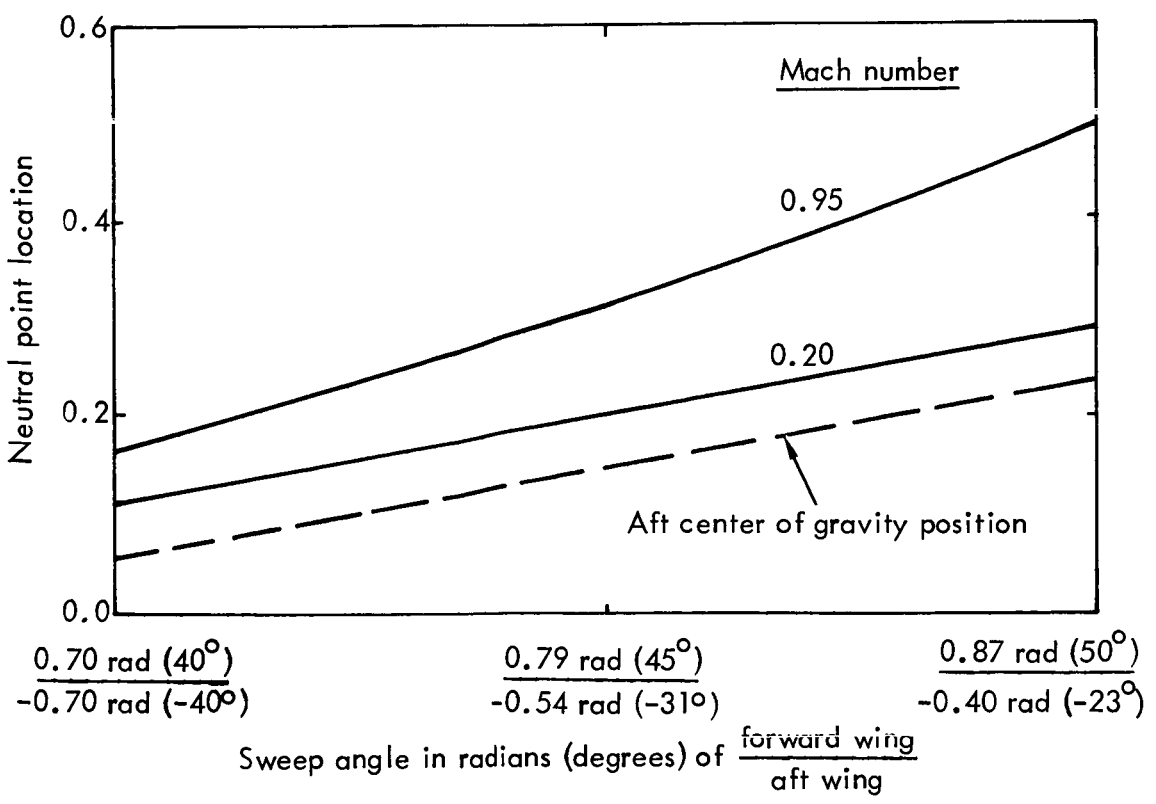
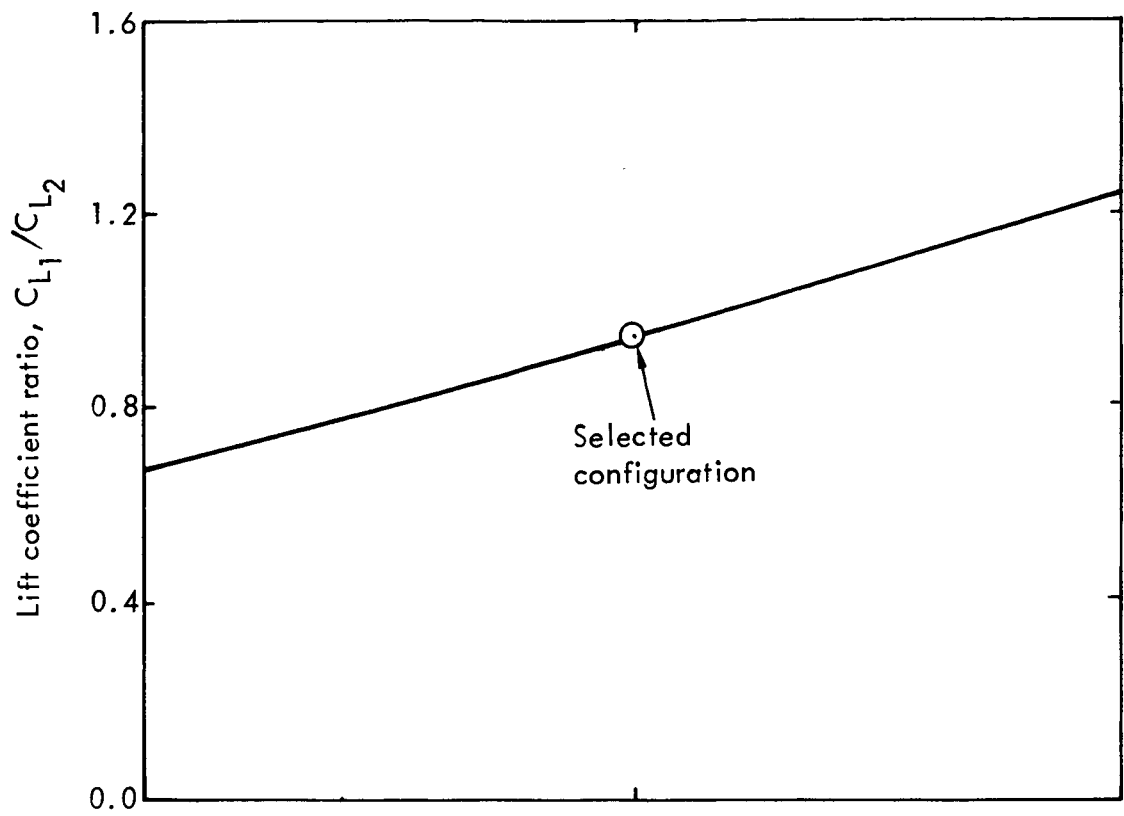


Figure 16. Results of wing-sweep analysis. Mach number of 0.95.

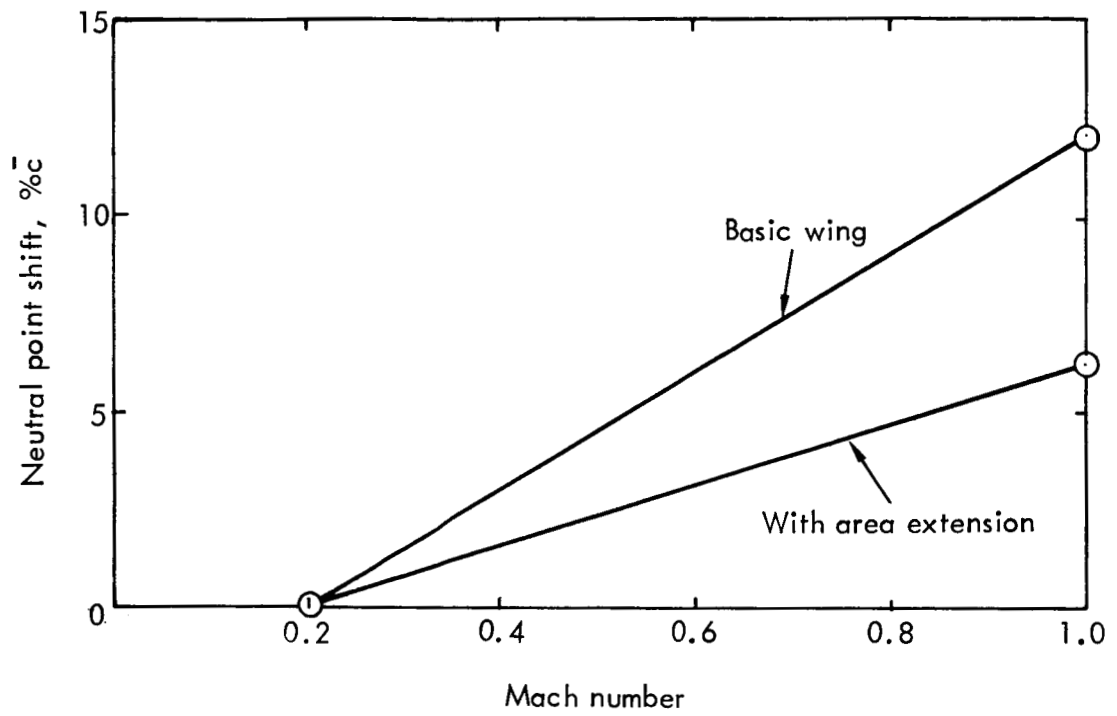


Figure 17. Effect of flap area extension on neutral point.

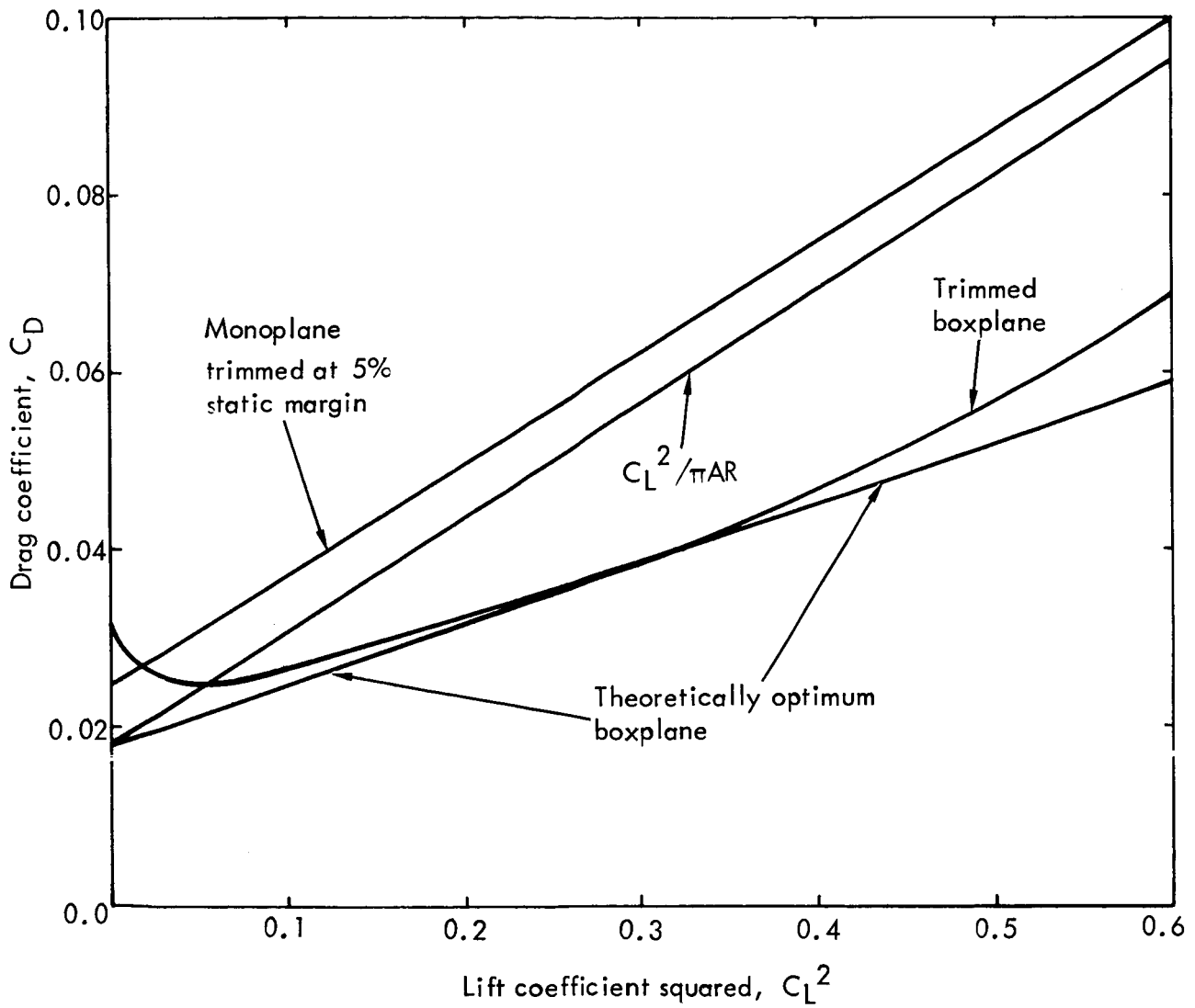


Figure 18. Boxplane trimmed drag characteristics.

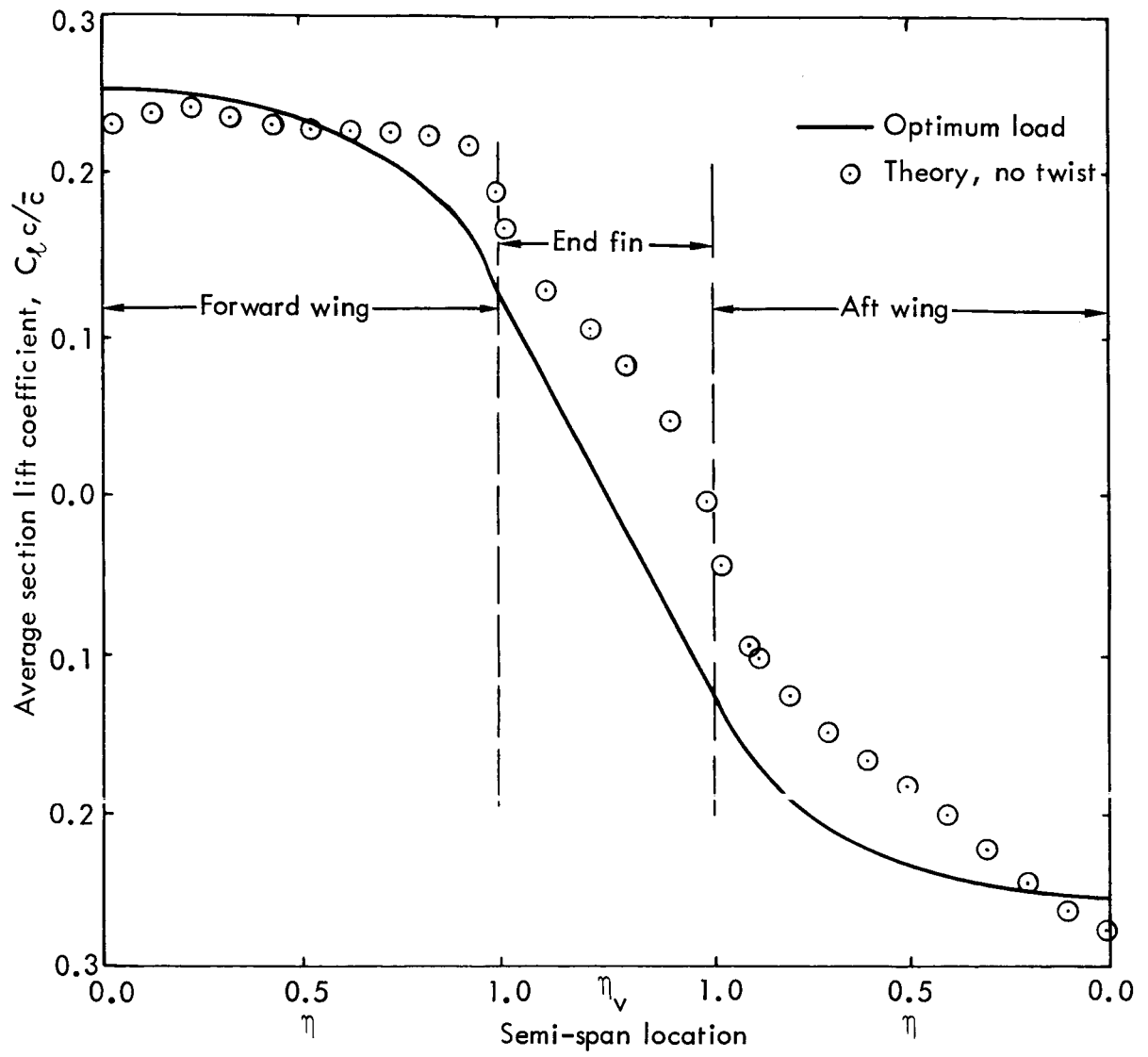


Figure 19. Biplane span-load distribution for cruise, $M = 0.95$, $C_L = 0.45$.

Wing front view and vertical displacement to span ratio, h/b

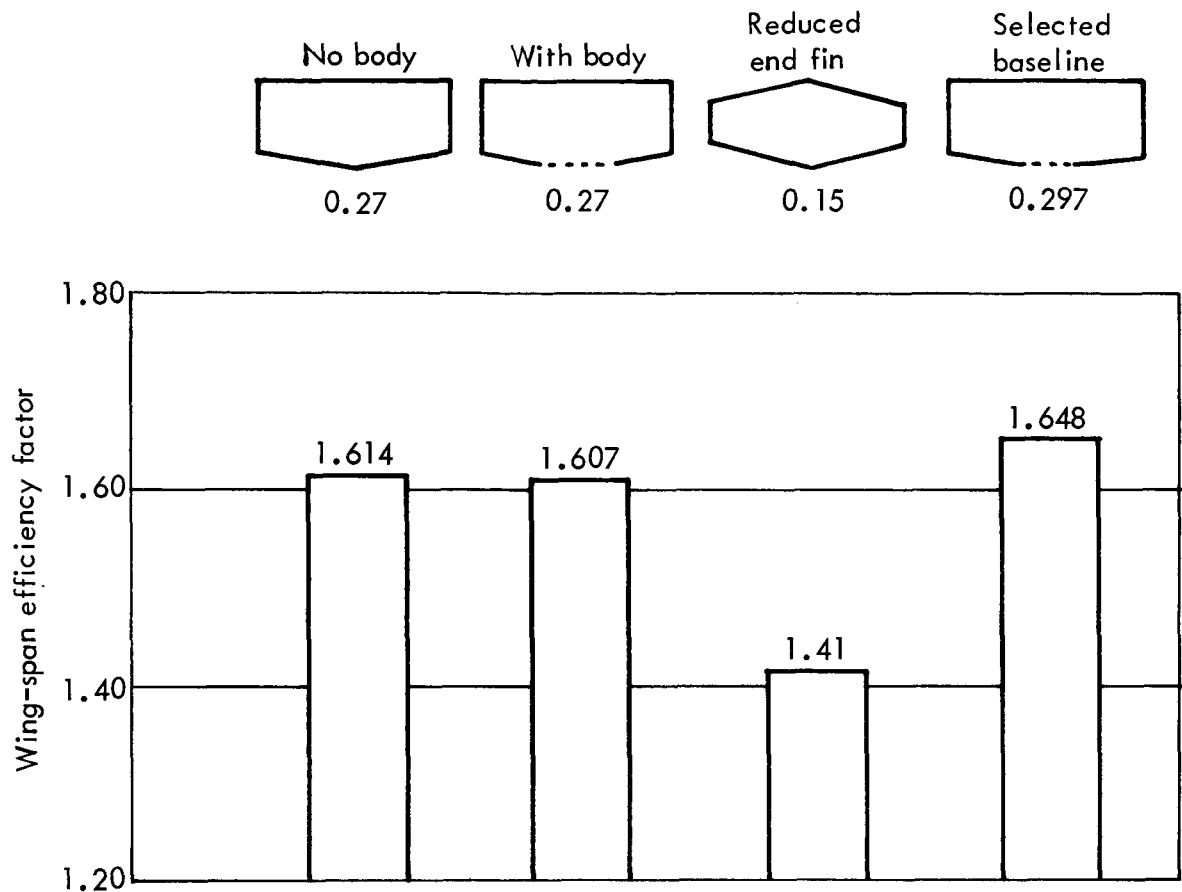


Figure 20. Wing configuration efficiency comparison for optimized loading.

only 15 percent of the wing span. In this case, the lower efficiency of 1.41 is equivalent to a drag penalty of 15 counts during cruise relative to the ideal box. The calculated efficiency of 1.648 for the selected baseline configuration is within one percent of the theoretical result indicated in Reference 1.

3.1.1.5 Lateral Control Requirements

A preliminary assessment was made of the aileron roll effectiveness required to meet the MILF 8785B requirement for achieving a 0.52 rad (30°) bank in 2.4 seconds in the landing configuration. This allows for a recovery from runway offset during approach. The control deflection time history was represented by 0.1-second transport lag in the system, with a linear application to maximum deflection. Assuming full control in one second, the value of rolling moment due to aileron deflection required at an approach speed of 72 m/sec (150 knots) was estimated to be 0.208. To determine available roll effectiveness for a typical aileron located between the 70-percent and 95-percent wing semi-span positions and having a chord length equal to 35 percent of the wing chord, a value of the non-dimensional radius of gyration, h_{xx}/b , was

assumed to be 0.20. This allowed for adjustments due to wing-mounted nacelles and tip fins. The corresponding value of rolling moment due to aileron deflection was 0.127, indicating that lateral control through wing-tip aileron alone was insufficient to meet the requirements. In order to minimize the loss in flap effectiveness for the maximum lift coefficient requirement, the aileron span was assumed to be limited to 25 percent of the wing semi-span. Previous studies have shown that a side-force capability of only 0.1-g is sufficient to accomplish the offset maneuver with existing roll power. It was assumed that "rudders" on the tip fins would provide the necessary side-force capability.

3.1.2 BASIC AERODYNAMIC DATA - HIGH LIFT

The development of basic aerodynamic data for the biplane high-lift performance was based on:

- (1) Theoretical methods which account for mutual interference between the two wings and give total loads on the configuration.
- (2) Maximum lift and drag data from wing tunnel results on a conventional monoplane with an advanced technology wing and a high-lift system.

One of the inherent requirements for this unique configuration is the degree of stall matching necessary between the two wings in order to achieve maximum lift coefficients comparable to the equivalent monoplane. This section contains a description of the procedures and methodology used for the biplane to estimate high-lift characteristics which could be compared directly with those of the ATT monoplane.

3.1.2.1 Wind Tunnel Data Sources

Since the biplane is to have field performance and cruise wing loading comparable to those of the ATT monoplane, preliminary evaluation indicated that this design would require sophisticated high-lift devices. Wind tunnel results for a mono-wing with an advanced technology section design, a double-slotted trailing edge flap, and a leading-edge slat of advanced design were used for the necessary data base. The double-slotted trailing-edge flaps have a 35-percent chord main segment and a 15-percent chord vane. The leading-edge slat is a slotted Krueger with a chord length equal to 15 percent of the wing chord.

No wind tunnel data are currently available on a closed-biplane configuration with the degree of refinement necessary to obtain the maximum performance benefits from an installed high-lift system.

3.1.2.2 Stall Matching and C_{LMAX} Definition

The maximum lift characteristics of the biplane system were evaluated by estimating the individual lift capability of each wing while recognizing the mutual interference due to induced upwash on the forward wing and downwash over the aft wing. Figure 21 presents a definition of C_{LMAX} for the total system. Each wing is

assumed to have the same basic area, and C_L values are based on the gross area S , where $S = S_1 + S_2$. The effective C_{LMAX} is defined by the stall of the forward wing. For satisfactory handling at the stall, it is desirable to obtain a forward-wing stall at a slightly lower angle of attack than the aft wing in order to obtain a nose-down pitch and good recovery characteristics. Slats on both wings are, therefore, desirable. As indicated on Figure 21, it is also necessary to achieve as high a value of C_L on the aft wing as possible at the corresponding stall angle of attack of the forward wing. This is obtained through optimum lift matching of the two wings by selecting equal wing-lift-curve slopes and by adjusting the decalage angle. The requirement for nearly equal $C_{L\alpha}$ values is consistent with the cruise optimization given in Section 3.1.1.4. For design of an optimum trailing-edge-flap system, the objective is to minimize the difference in zero-lift angle between the wings, and to maximize the total lift of the configuration without creating large adverse trim effects.

The untrimmed value of C_{LMAX} , as shown in Figure 21, is defined as

$$C_{LMAX} = (C_{LMAX1} + C_{LMAX2})/2 \quad (9)$$

for $S_1 = S_2 = S/2$.

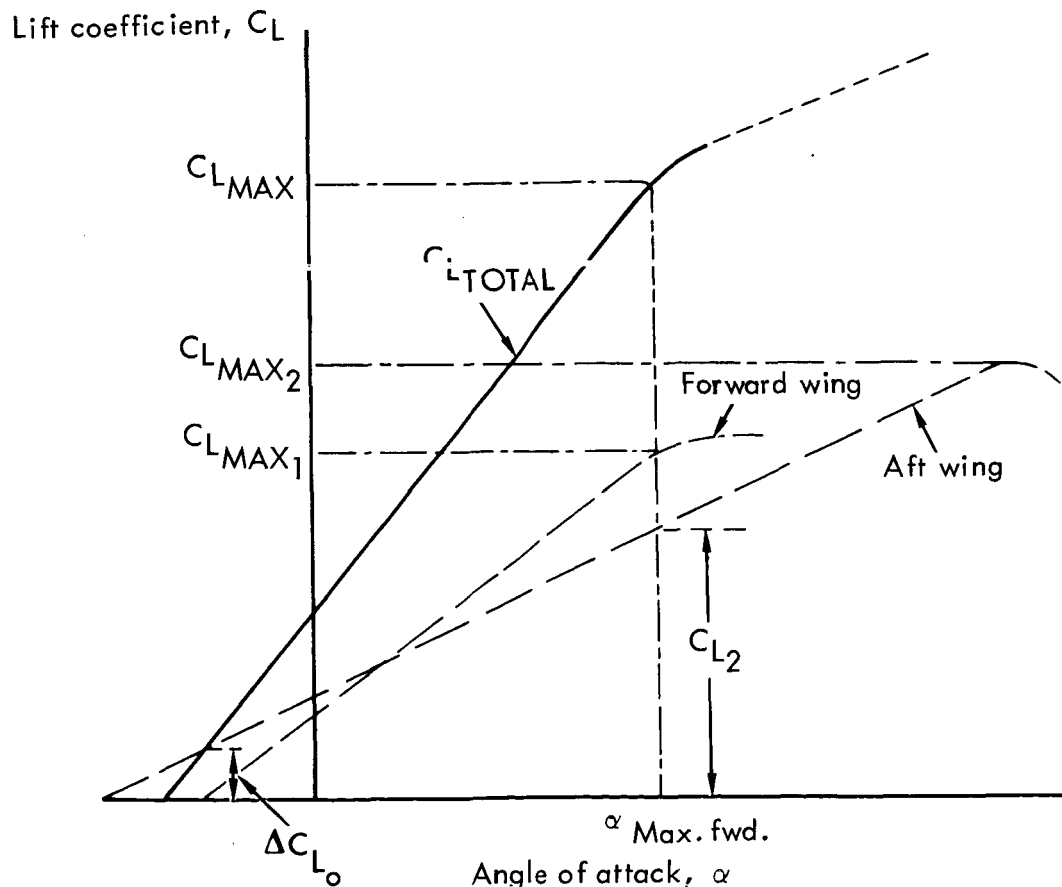


Figure 21. C_{LMAX} definition for biplane.

3.1.2.3 C_{LMAX} Estimation

Basic Methods - The predicted values of C_{LMAX} for the biplane configuration were derived from the following expression.

$$C_{LMAX} = C_{LMAX_{clean}} \left(\frac{\cos \Lambda}{0.743} \right) + \Delta C_{LMAX_{slat}} \left(\frac{\cos^2 \Lambda}{0.552} \right) + \Delta C_{LMAX_{flap}} \left(\frac{K_{\Lambda}}{0.76} \right) \quad (10)$$

Each term on the right-hand side of the equation contains a sweep factor correction; no aspect ratio correction was considered necessary. The cosine factor applied to the clean C_{LMAX} term is consistent with correlation studies made at Lockheed on results of equivalent two-dimensional tests on similar airfoils. Sweep corrections for the slat increments are based on empirical data given in Reference 8, and the flap sweep correction factor is taken from Reference 9. The flap chord is assumed to be the same as the basic design.

Part-span corrections predicted by the empirical method in Reference 10 were used extensively during the study in order to develop an optimum design. Incremental flap-lift data are given in Figure 22.

Since the application of these data to the biplane configuration considers both high-wing and low-wing configurations, corrections must be made for losses in $\Delta C_{LMAX_{flap}}$ from fuselage carry-over effects on the low forward-mounted wing. These were obtained by comparing test data for a high-wing and low-wing configurations for an identical flap span. Figure 23 presents a derived incremental value of C_{LMAX} due to body effects.

The basic slat increment to C_{LMAX} was derived from test data for a flap angle of 0.52 rad (30°). Results indicated that the slat increment in C_{LMAX} was constant over the range of flap angles under consideration. The incremental C_{LMAX} due to the slat was measured at an optimum slat angle of 0.87 rad (50°).

Preliminary Configurations - Development of a satisfactory flap arrangement occurred in three stages. In configuration (A), shown in Figure 24, the initial elevator and aileron sizing requirements dictated mid-span single-segment flaps on each wing. The estimates of the required maximum lift coefficients were based on the same criteria as those for the ATT study, namely, a C_{LMAX} of 2.44 for a landing approach speed of 77.17 m/sec (150 knots) and a C_{LMAX} of 2.38 for takeoff at 3048 m (10 000 ft). It was found that the flap design of configuration (A) produced values of full-scale C_{LMAX} in the region of 1.8 to 2.0 in the landing configuration. Further, elevator power was found to be insufficient to trim at the high-lift condition as a result of the large nose-down pitching moments incurred by the aft-wing flap. Arrangement (B) was designed to relieve the adverse trim effects by introducing flap segments on the forward wing. Figure 25 presents typical results from the lifting-surface computer program giving $C_L - \alpha$ and $C_m - C_L$ characteristics for different flap panel schedules on configurations (A) and (B). Based on these results the configuration

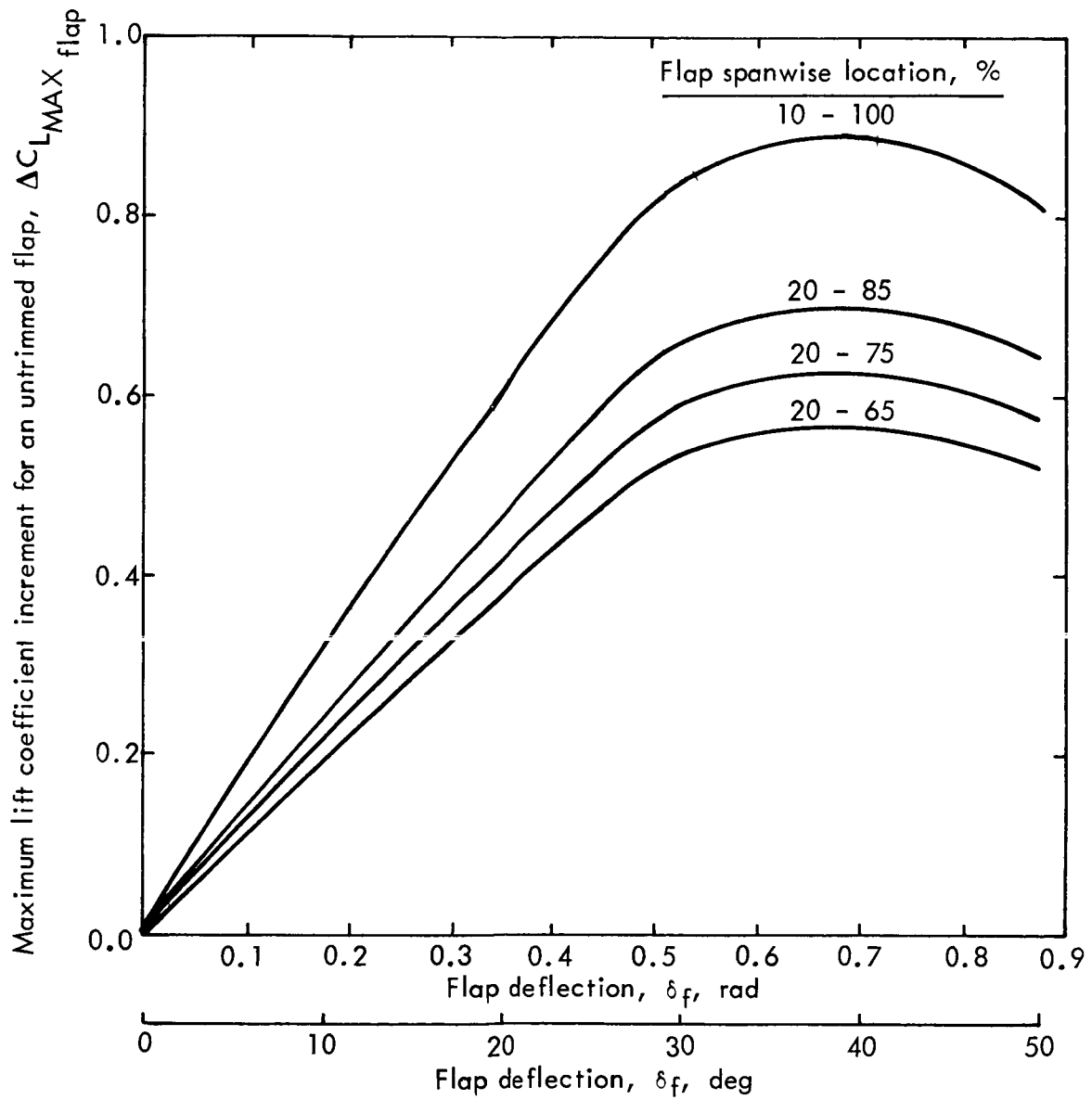


Figure 22. Part-span flap $C_{L_{MAX}}$ increments.

(B) forward-wing inboard and outboard flap segments are set at 0.4 rad (25°) and used as pitch and roll controls, respectively. This configuration produced values of C_{LMAX} close to the requirements, but the necessity for full area extension on both wings to minimize transonic neutral-point shift dictated full-span controls on the aft wing. This was adopted on configuration (C).

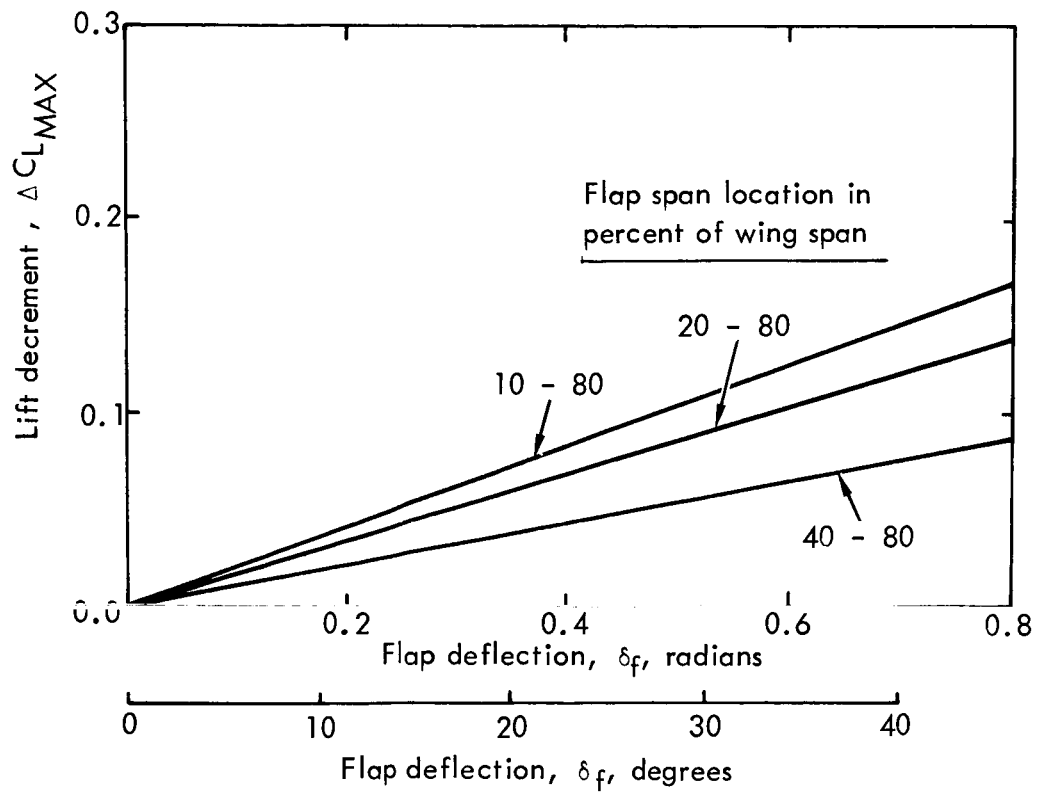


Figure 23. C_{LMAX} decrement due to fuselage effects.

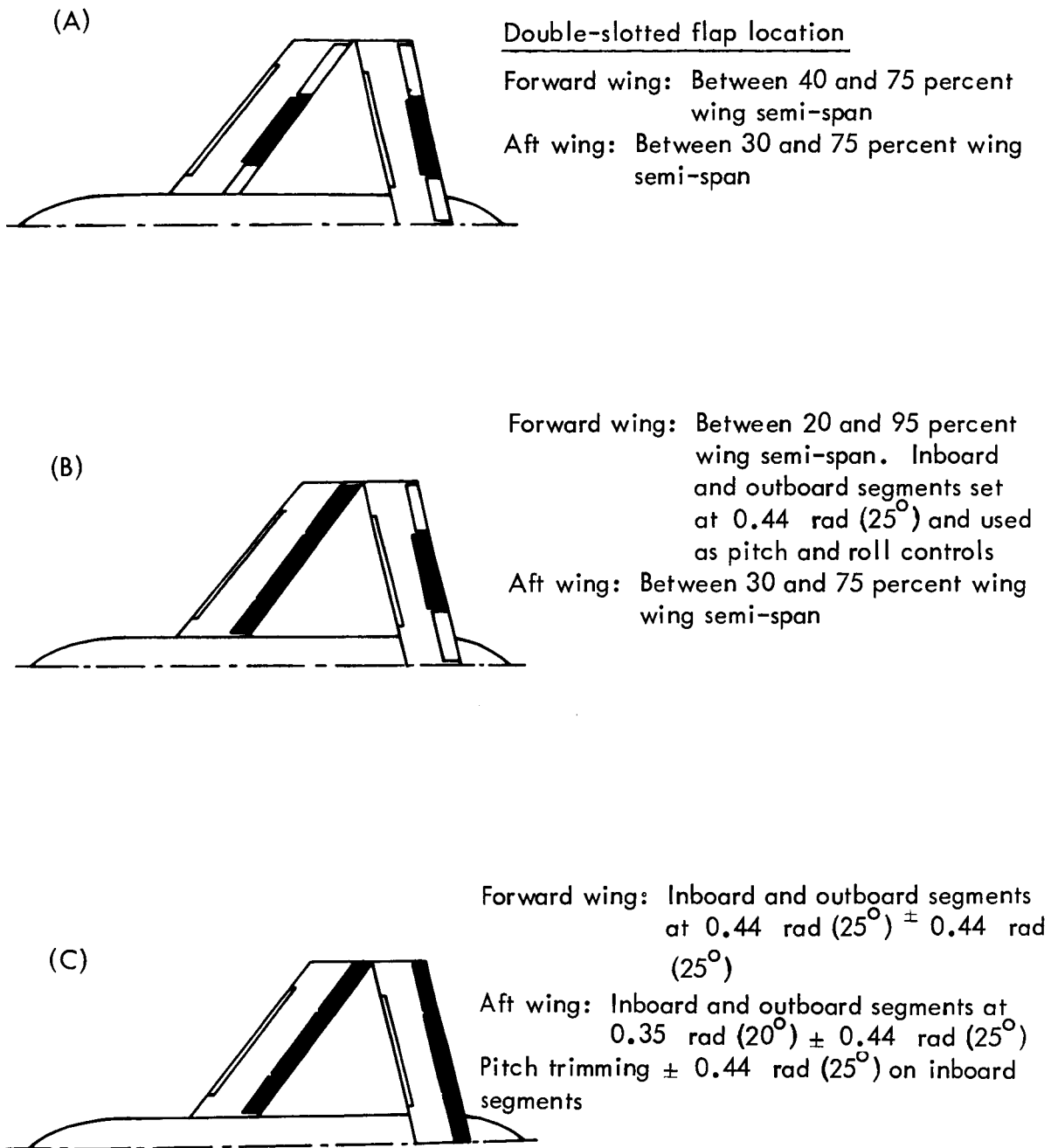


Figure 24. Biplane high-lift development. Slotted Krueger slat between 32 and 80 percent wing semi-span; slat angle of $0.87 \text{ rad } (50^\circ)$.

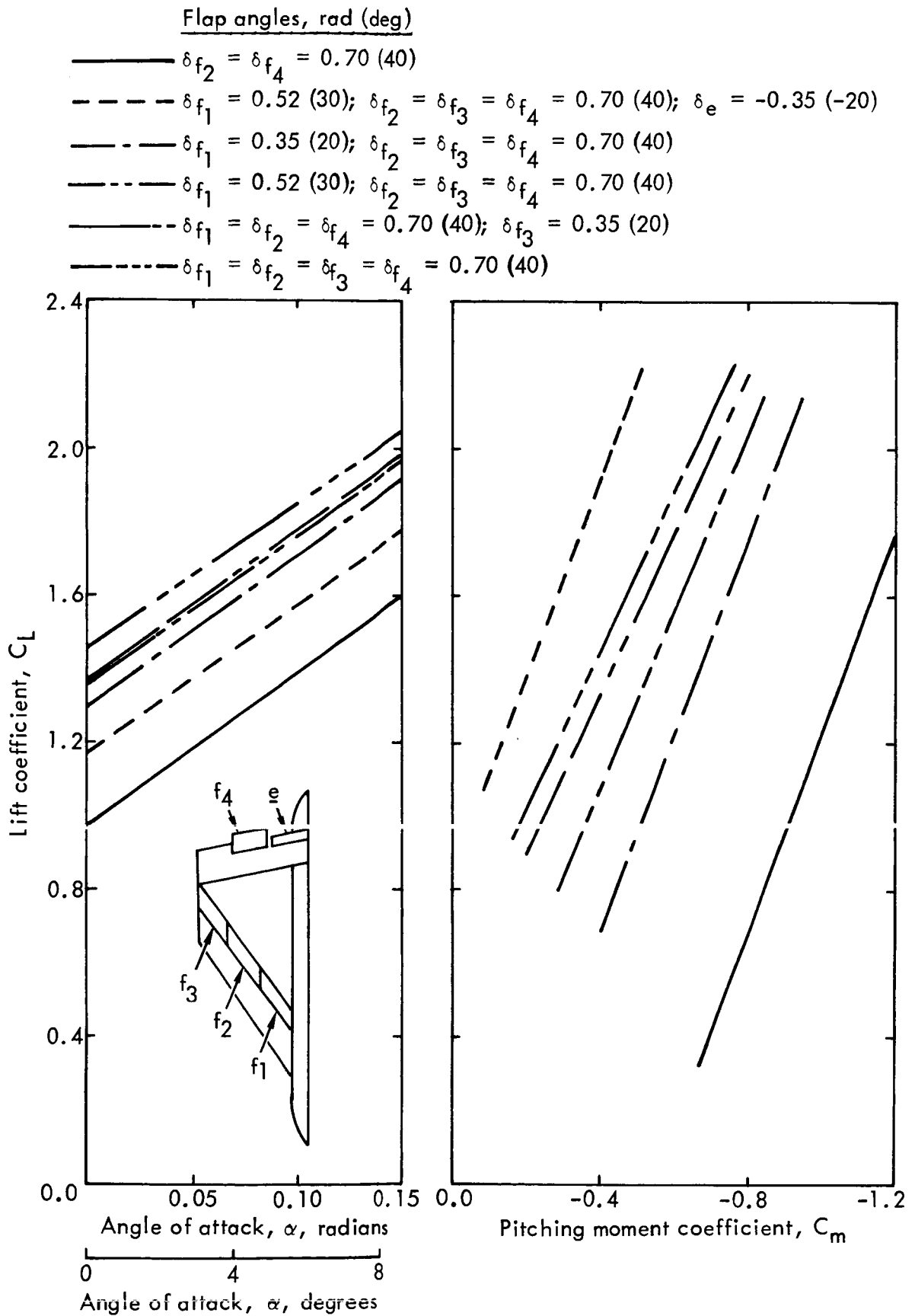


Figure 25. High-lift trim study results.

Selected Flap Configuration - Each wing of configuration (C) has a full-span, three-segment, double-slotted flap. On the forward wing, the inboard and outboard segments are set at 0.44 rad (25°), with a ±0.44 rad (25°) movement for controls. The aft-wing inner and outer segments are also used as pitch and roll controls. For high-speed maneuvers, the trailing-edge position of the aft-wing inner and outer segments are actuated ±0.35 rad (20°).

Results from lifting-surface theory computations are shown in Figure 26 for three aft-wing flap-angle settings when the forward-wing flap angles are 0.44 rad (25°)/0.70 rad (40°)/0.44 rad (25°). Values of the lift coefficient for each wing at angles of attack less than the stall value were combined with the estimated C_{LMAX} data to develop the $C_L - \alpha$ curves shown in Figure 27. Analysis of the high-lift data for a monoplane and that for the lifting-surface computations for a biplane indicate that the effects of mutual interference between the wings of a closed-biplane configuration are responsible for an induced upwash influence of 0.05 rad (3°) to the forward wing. Thus, the stall angle of attack of the forward wing was estimated to be 0.26 rad (15°), rather than 0.31 rad (18°) for a similar monoplane wing. For the cases considered, the highest untrimmed maximum lift occurs for the 0/0.70 rad (40°)/0.35 rad (20°) aft-flap configuration. The pitching moment results given in Figure 28, however, indicate that trimming from deflection of both fore and aft elevators is insufficient for the aft center-of-gravity case. (It was assumed in this preliminary analysis that clean values of $C_{m_0} = 0$ are obtainable from refined design.) With a flap deflection of 0.35 rad (20°) for the entire span of the aft wing, sufficient trim power is available but at a loss of 0.13 in C_{LMAX} . For aft-wing flap deflections of 0/0.35 rad (20°)/0.35 rad (20°), it was found that trimming with the forward elevators only would give a favorable increment to C_{LMAX} .

Scale Effects & Dynamic Stall Corrections to C_{LMAX} - An analysis of Reynolds number corrections and dynamic stall effects for a number of transport aircraft was made in order to substantiate a realistic full-scale correction for this study. Two transport aircraft data points, other than Lockheed configurations, are taken from References 11 and 12. The ratio C_{LSTALL}/C_{LMAXWT} presented in Figure 29 includes scale effects between the wind-tunnel-measured C_{LMAX} in the 1-g condition and the corresponding flight-equivalent 1-g data, and also the increment obtained from the Federal Aviation Regulations (FAR) stall requirement of minimum speed in a 0.514 m/sec² (1 knot per second) entry rate. Although scale effects for slatted configurations are shown to be considerably reduced, particularly for the slotted Krueger configuration (Reference 11) representative of the design assumed for the biplane configuration, values of C_{LFAR}/C_{LMAXWT} of the order of at least 1.12 are indicated. Thus, for the present study, a conservative full-scale correction of 10 percent was assumed to correct the predicted maximum lift coefficient values from a wind-tunnel Reynolds number of 2.5×10^6 /mean-aerodynamic-chord (MAC) to full-scale values.

Predicted Full-Scale Maximum Lift Coefficient - The table of numbers given in Table I indicates the build-up of maximum lift coefficient for the landing configuration. Figure 30 presents estimated full-scale maximum lift coefficient data for the selected high-lift system. These values are competitive with those for the ATT configuration.

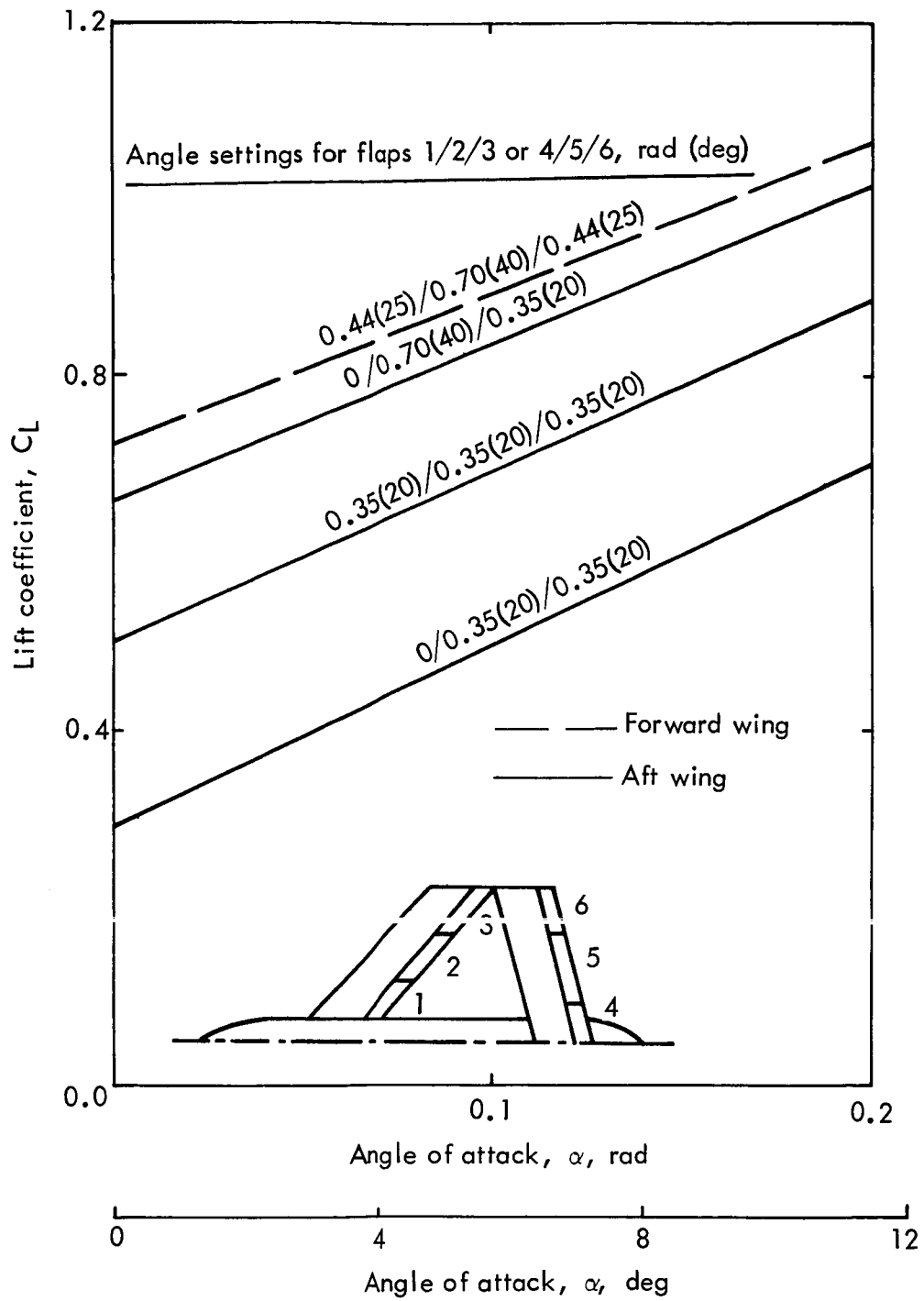


Figure 26. Effect of aft-wing flap settings on wing-lift matching for configuration (C).

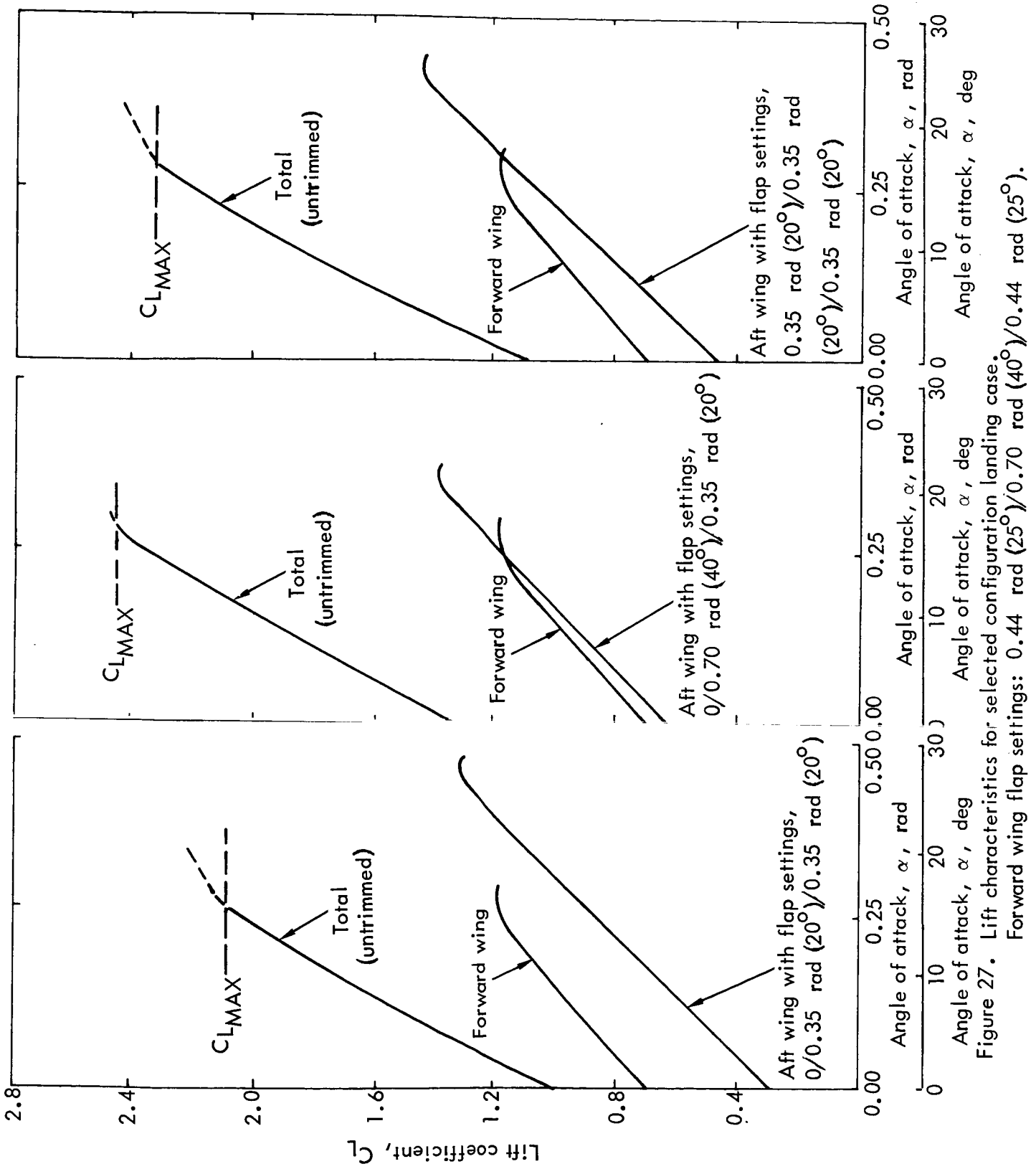


Figure 27. Lift characteristics for selected configuration landing case.

Forward wing flap settings: 0.44 rad (25°)/ 0.70 rad (40°)/ 0.44 rad (25°).

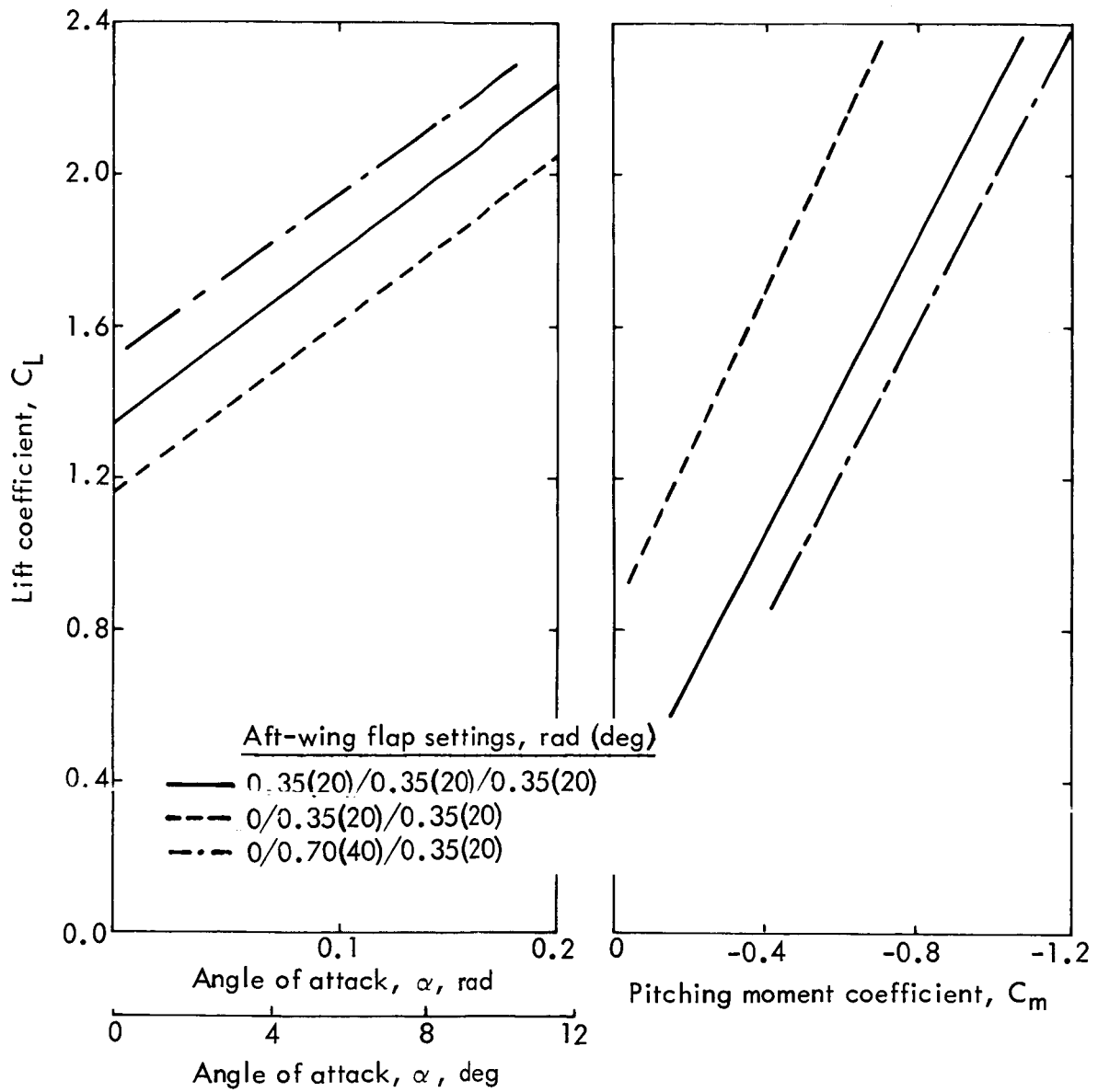


Figure 28. Lift and pitch characteristics for selected configuration.
 Forward-wing flap settings: 0.44 rad (25°)/0.70 rad (40°)/
 0.44 rad (25°)

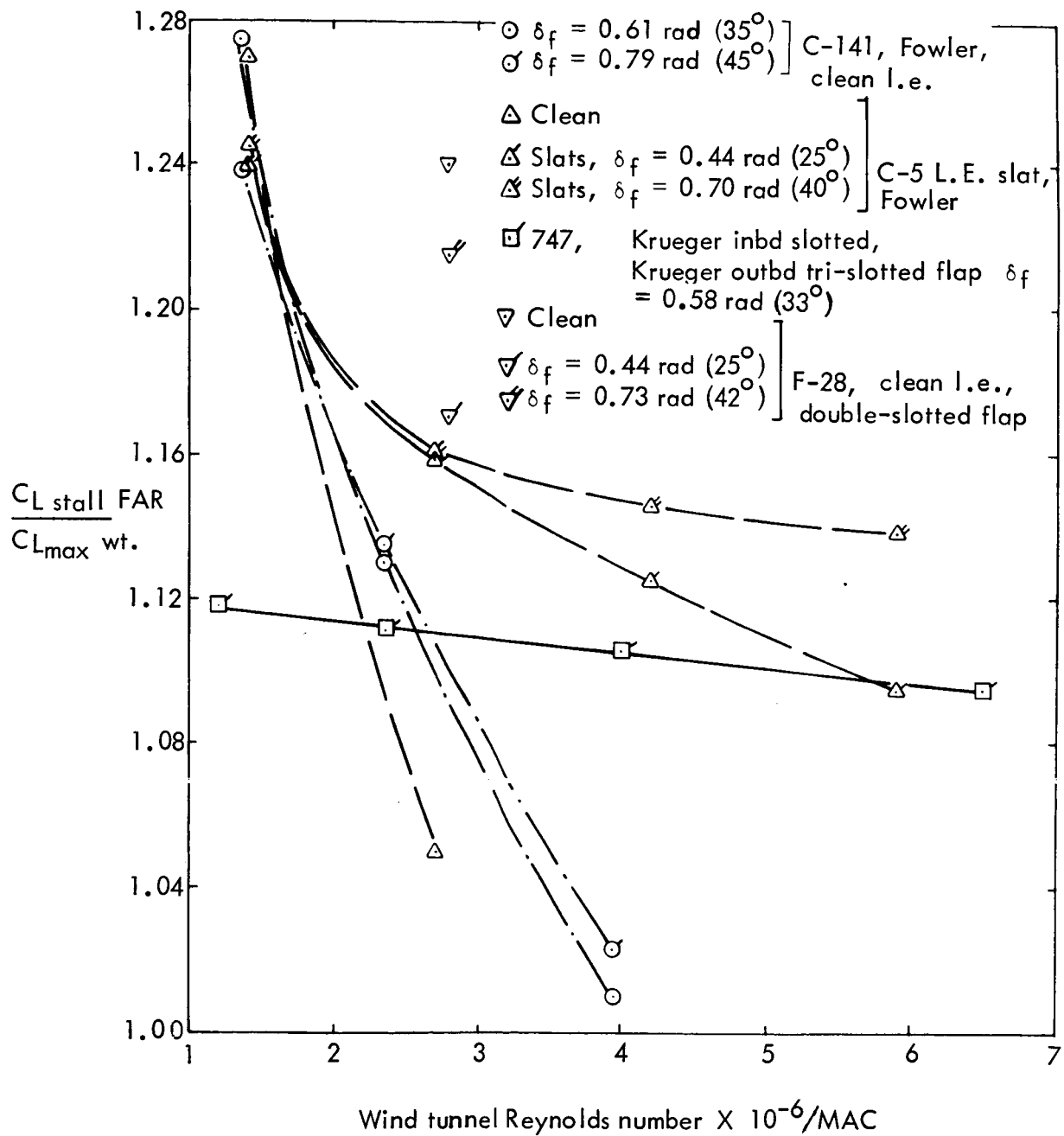


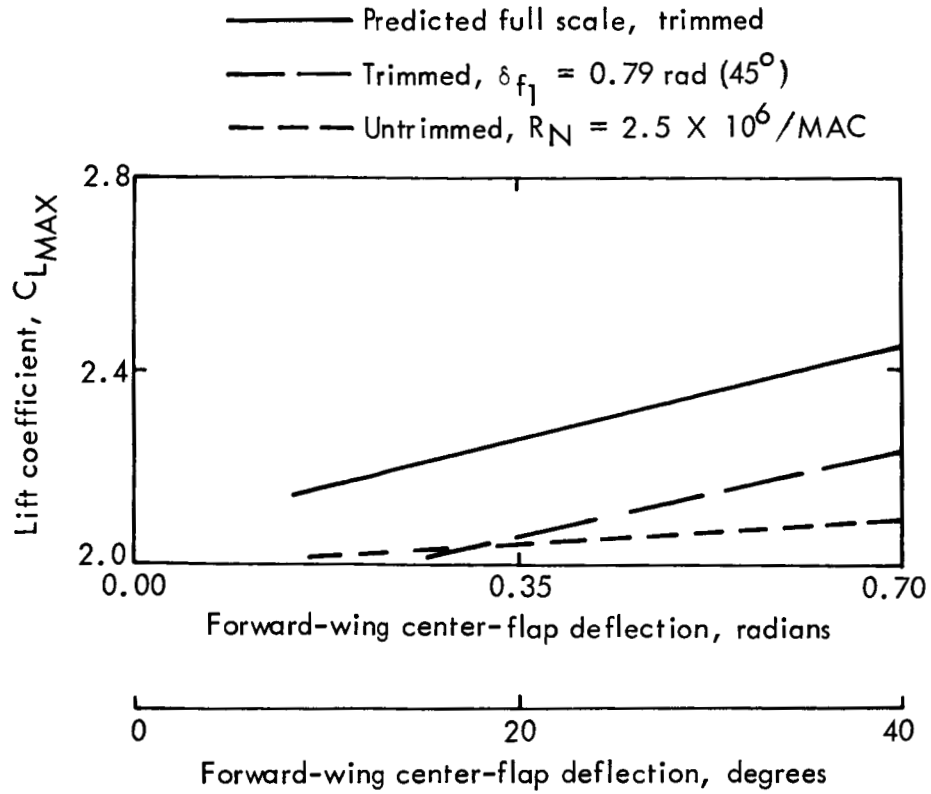
Figure 29. Full-scale corrections to maximum lift coefficient.

TABLE I. $C_{L_{MAX}}$ SUBSTANTIATION

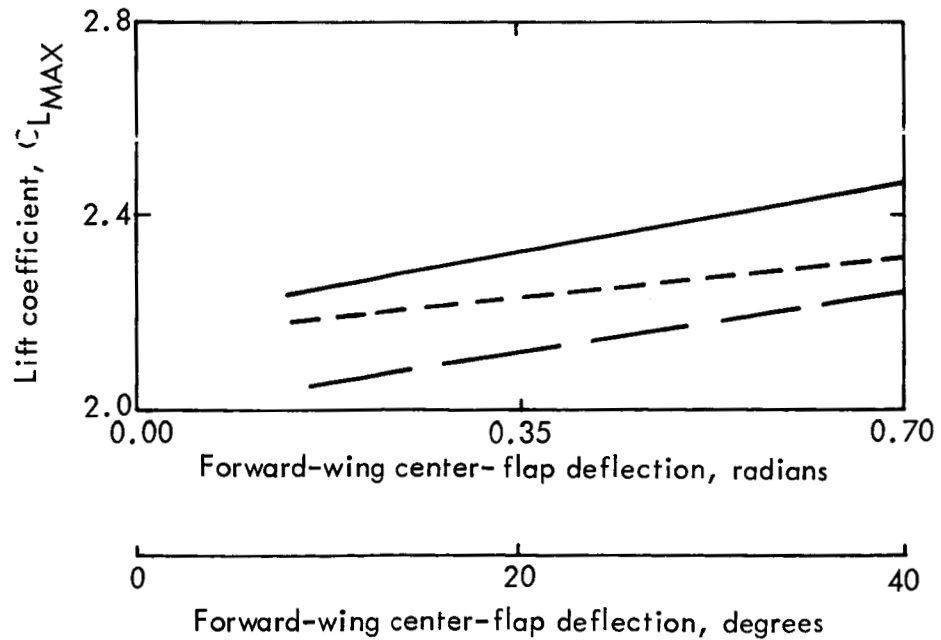
<u>Forward wing</u>	<u>$\Delta C_{L_{MAX}}$</u>
Clean	1.142
Flaps (0.44 rad(25°)/0.70 rad (40°)/0.44 rad (25°))	0.662
Slats	<u>0.580</u>
$C_{L_{MAX}}$ (untrimmed, based on forward wing area)	2.384
$C_{L_{MAX}}$ (untrimmed, based on total wing area)	1.192
<u>Aft wing (lift coefficient at forward-wing stall angle)</u>	
A. Total, untrimmed, based on total wing area with aft flap setting of 0/0.35 rad (20°)/0.35 rad (20°)	0.900
B. Total, untrimmed, based on total wing area with aft flap setting of 0.35 rad (20°)/0.35 rad (20°)/0.35 rad (20°)	1.110

Maximum Lift Coefficient Values for Various Aircraft Conditions

Condition	Wing combinations	
	Forward + aft A	Forward + aft B
Untrimmed at $R_N = 2.5 \times 10^6 / MAC$	2.092	2.312
Trimmed	2.220	2.245
Full scale	2.445	2.465
ATT M = 0.95 configuration	2.38	



a) Aft-wing flap angles $0 \text{ rad } (^\circ) / 0.35 \text{ rad } (20^\circ) / 0.35 \text{ rad } (20^\circ)$



b) Aft-wing flap angles $0.35 \text{ rad } (20^\circ) / 0.35 \text{ rad } (20^\circ) / 0.35 \text{ rad } (20^\circ)$

Figure 30. Predicted full-scale lift characteristics.

3.1.2.4 High-Lift Drag

Drag with high-lift devices was calculated by modifying test data from the same source as the maximum-lift data base. Sweep and part-span factors from References 13 and 14, respectively, were used to obtain equivalent data for the biplane. The slat and flap zero-lift drag increment is thus defined as

$$\Delta C_{D_{0_{f+s}}} = \frac{1}{2} f(\Lambda, \eta_f) (\Delta C_{D_{0_1}} + \Delta C_{D_{0_2}}) \quad (11)$$

The equation for total drag in the high-lift condition is

$$C_D = C_{D_{0_{\text{clean}}}} + \Delta C_{D_{0_{f+s}}} + \Delta C_{D_{p_{C_L}}} + C_{D_i} \quad (12)$$

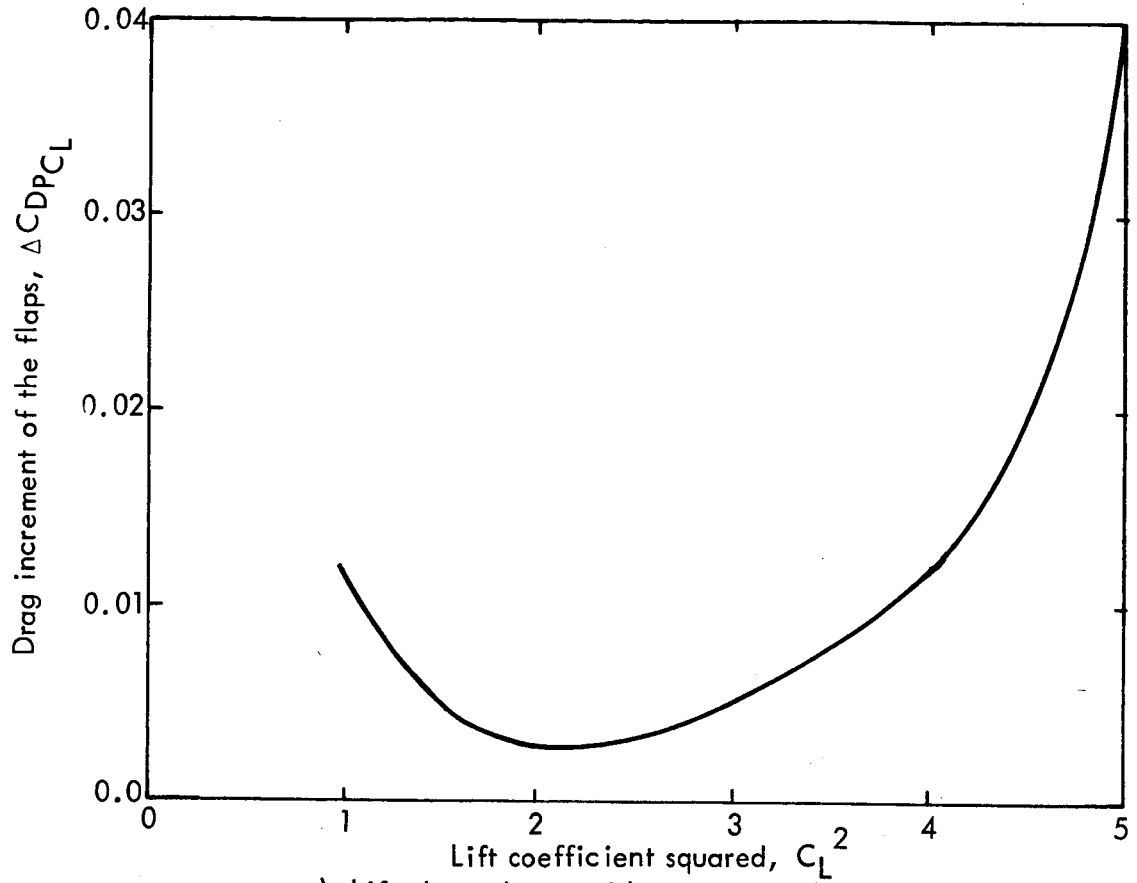
The variation of profile drag with lift, $\Delta C_{D_{p_{C_L}}}$, was derived by comparing total drag with estimated values of vortex drag from the basic wing and flap system. Values of $\Delta C_{D_{0_{f+s}}}$ and $\Delta C_{D_{p_{C_L}}}$ for use in the current study are shown in Figure 31. These are for a flap spanning the region between 10 percent and 80 percent of the wing semi-span and for a slat of approximately 50 percent of the wing semi-span.

Fuselage Interference Correction - Estimates are also provided for the effects of the fuselage on the low-mounted forward wing with flaps deployed. Evidence of wing height effects on flaps-down drag is indicated in Figure 32. For identical flap spans and a value of 0.6 for the ratio of body-width to basic wing chord, a drag increment of 0.030 is experienced at typical operating lift coefficient values. Over the range of flap angles of interest, this is approximately constant. For the biplane configuration the effects of the ratio of body-width to basic wing chord were assumed to be linear and modified by part-span correction factors for smaller flap-span values.

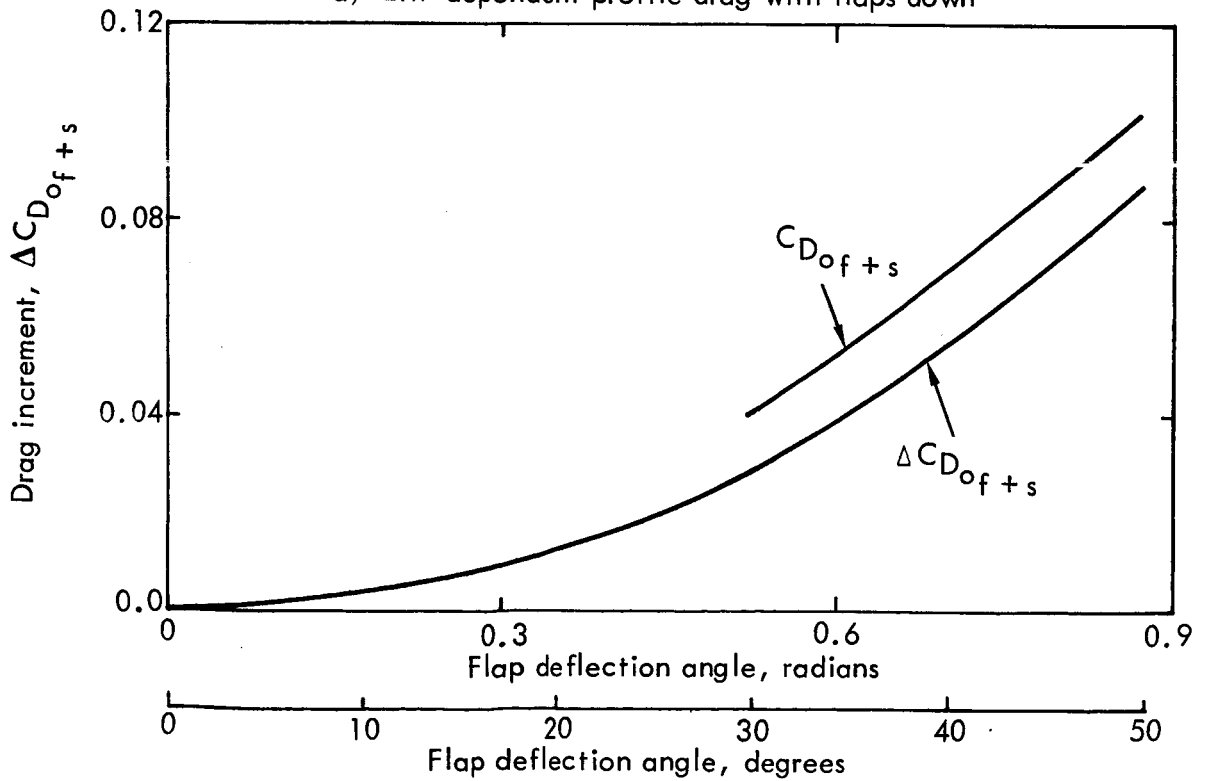
Flaps-Down Load Distributions - Comparative span-load distributions for mid-segment and full-span flaps are presented in Figures 33 and 34, respectively. The former indicates the incremental load due to flaps with an overall span efficiency factor of 0.985. Figure 34 shows significantly improved load distributions through use of full span flaps. These studies were continued during Phase II of the program to determine minimum induced drag for airfield performance.

3.2 DESIGN INTEGRATION

Seating for 400 passengers (a design objective discussed in Section 1) was the determining factor in sizing the fuselage which is configured on the basis of 20-percent first class and 80-percent tourist class passengers. One advantage of the transonic biplane configuration is that a cross-sectional area distribution which satisfies a defined curve can be accomplished without indentation of the fuselage and without adverse



a) Lift-dependent profile drag with flaps down



b) Drag increment of the flaps and slats

Figure 31. High-lift system drag increments.

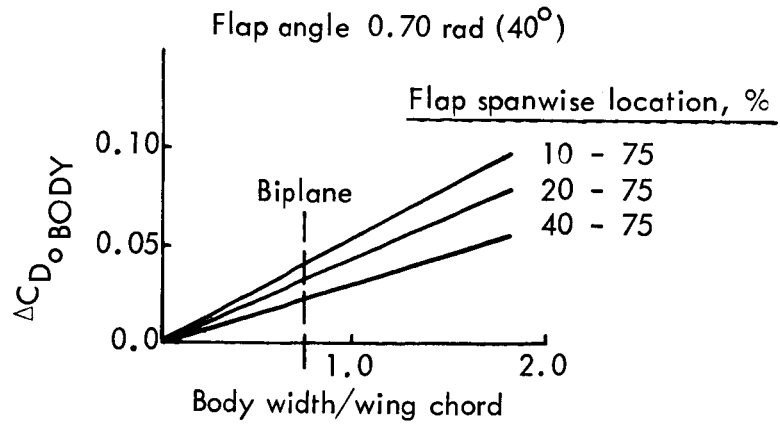


Figure 32. Effect of wing location on flaps-down drag.

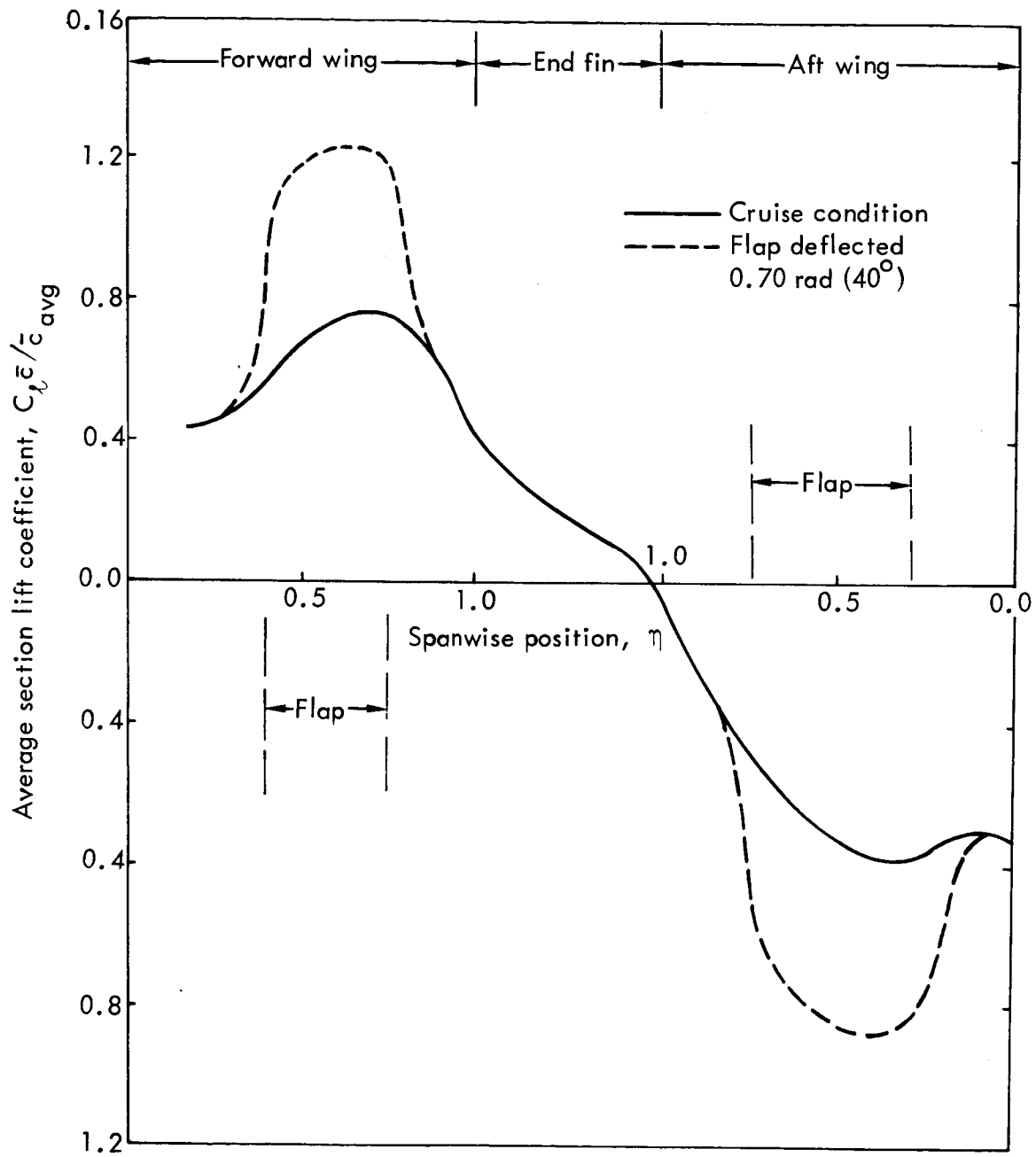


Figure 33. Spanwise load distribution with mid-segment flaps.

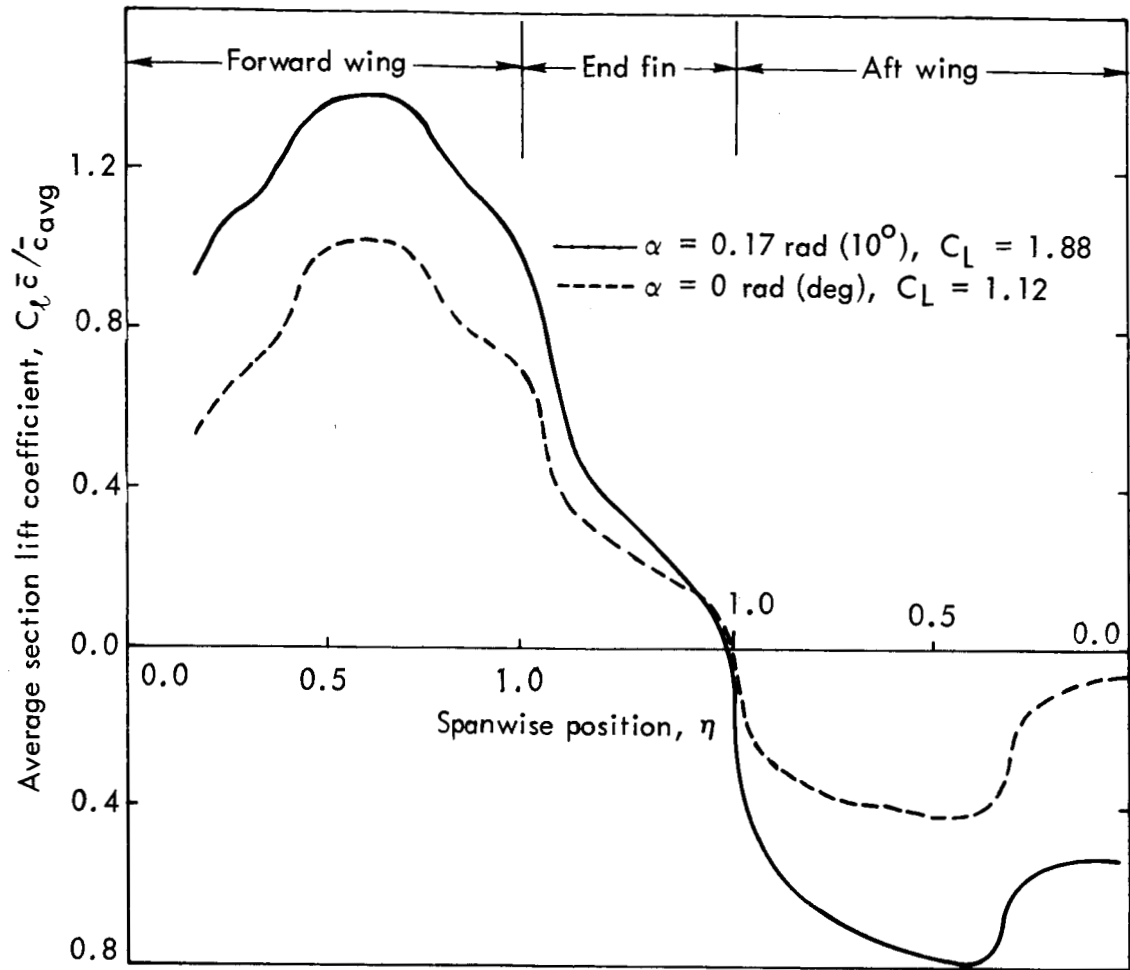


Figure 34. Spanwise load distribution with full-span flaps.
 Mach number 0.20.

effects upon the seating arrangement. An initial study configuration was developed and subsequently improved based on aerodynamic and structural analysis results to achieve an interim configuration.

3.2.1 INITIAL STUDY CONFIGURATION

The development of the initial study configuration, shown earlier in Figure 6, is based upon the ATT monoplane final configuration which was designed for the same mission parameters listed in Section 1. The biplane has the same wing area and was assumed to have the same gross weight as the ATT monoplane configuration but the aspect ratio has been adjusted to provide the initial biplane configuration with the same lift-to-drag ratio during cruise as the monoplane counterpart. The preliminary aerodynamic analyses indicated that equal-area, equal-sweep fore and aft wings having quarter-chord sweeps of 0.70 rad (40°) would be required. The fore and aft wing geometric relationship is arranged to provide a balanced configuration and a smooth area distribution conforming to that of the ATT $M = 0.95$ monoplane but with slight modifications to account for the stream tube effects of the forward-wing/fuselage intersection. Each of the wings has a planform gross area of 221.3 m^2 (2382 ft^2) and a constant thickness-to-chord ratio of 10 percent.

The wings are connected at the tips by vertical fins whose vertical separation is established by the aerodynamic considerations that provide improved levels of induced drag (see Section 3.1.1.1). The vertical tip-fins are swept aft 0.52 rad (30°) at the quarter-chord generator and have a thickness/chord ratio of 10 percent. Initially, these elements were considered to be potential locations for the fuel tanks. Support for the aft wing is provided by a vertical stabilizer mounted on the aft fuselage. The vertical stabilizer has a taper ratio of 0.8, is swept forward 0.75 rad (43°) at the quarter-chord position, and has a thickness/chord ratio of 12 percent.

The propulsion system consists of four fan-jet engines developing 199 005-N ($44\ 738\text{-lb}$) thrust at sea-level standard conditions and having a bypass ratio of 5. These engines are mounted on the forward wing at the 50-percent semi-span and tip positions.

The area distribution data presented on Figure 35 show the relationship of the various components and demonstrate that the area "bubble" that would occur as the result of a constant-section fuselage is eliminated by the addition of ventral pods which are required for the stowage of the main landing gears and to provide volume for the stowage of part of the mission fuel.

The two main landing gears are of the single-strut, six-wheeled truck type. They are located to provide ground stability at operating weight and a ground-clearance angle of 0.21 rad (12°) for the rear fuselage.

A weight breakdown and the geometric characteristics for the initial study configuration are shown on Tables II and III, respectively. The data for the initial configuration were used to provide the input information necessary to generate weight estimation equations for biplane configurations through the use of computerized structural analyses.

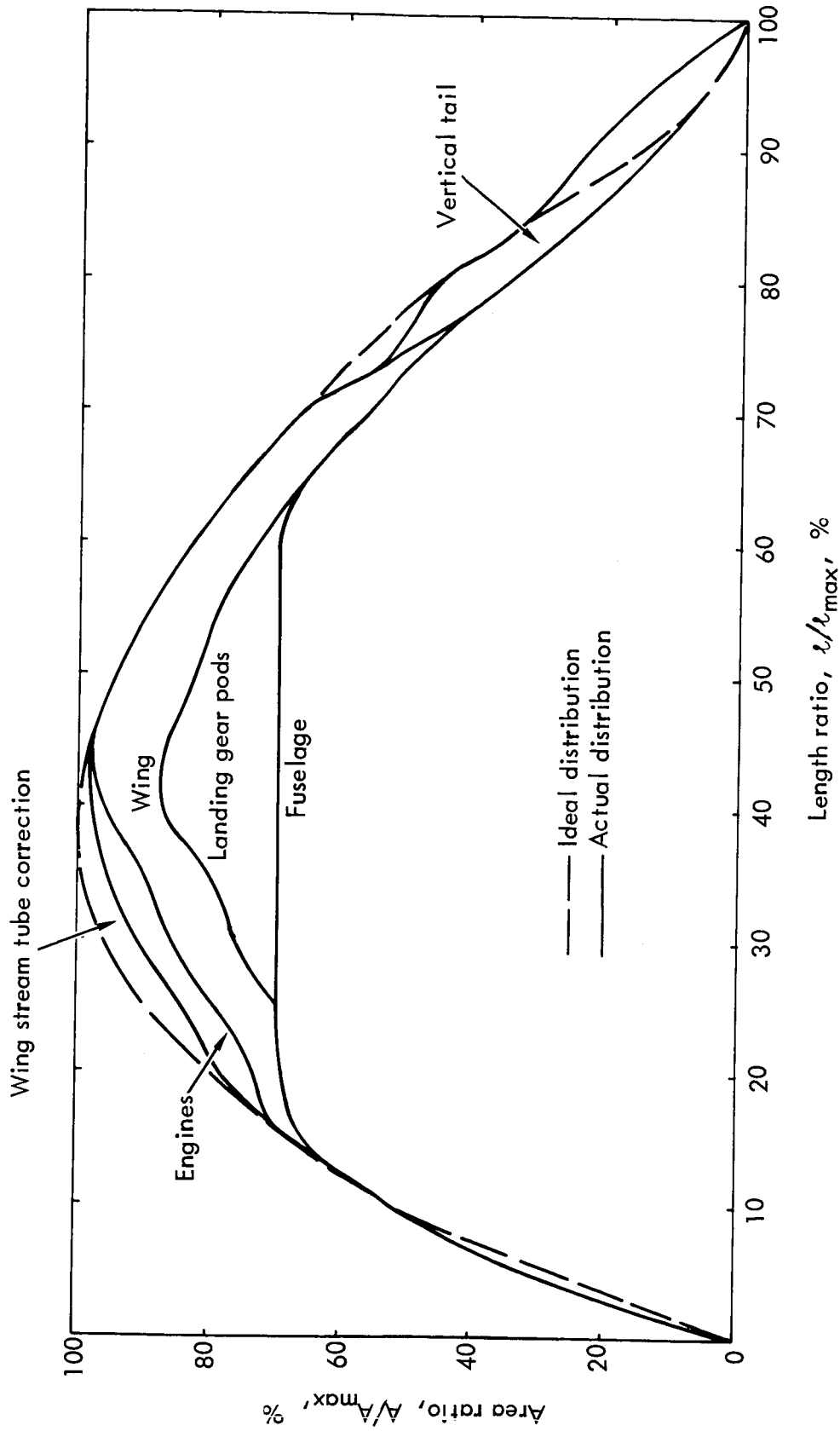


Figure 35. Biplane area distribution. $A_{max} = 51.4 \text{ m}^2$ (553.6 ft^2), equivalent diameter = 8.09 m (26.55 ft), length = 71.1 m (233.3 ft).

TABLE II. INITIAL STUDY CONFIGURATION WEIGHT STATEMENT

Item	Weight	
	kg	lb
Weight empty	115 219	254 015
Operating equipment	12 864	28 361
Operating weight	128 084	282 376
Passenger payload	38 465	84 800
Zero fuel weight	166 548	367 176
Fuel	135 737	299 248
Gross takeoff weight	302 285	666 424

TABLE III. INITIAL STUDY CONFIGURATION GEOMETRIC CHARACTERISTICS

Wing area	442.6 m ² (4764 ft ²)
Aspect ratio	4.12
Wing span	42.7 m (140 ft)
Fuselage length	71.1 m (233.3 ft)
Forward-wing sweep	0.70 rad (40°)
Aft-wing sweep	-0.70 rad (-40°)
End plate area total	138.1 m ² (1486 ft ²)
Vertical tail sweep	-0.82 rad (-47°)
Vertical tail area	90 m ² (968.5 ft ²)

3.2.2 INTERIM CONFIGURATION

3.2.2.1 Configuration Development

Wings of tapered planform were considered for this study as were extended root-chord arrangements and combinations of tapered inboard and constant-chord outboard. The selected wing planform on both wings consists of a tapered planform out to the 50-percent semi-span position and a constant-section outboard panel. Since structural studies indicated that the selected planform yielded the lowest takeoff gross weight airplane, it was used on the interim configuration shown on Figure 36. Weights and geometric characteristics for this configuration are listed on Tables IV and V, respectively.

The propulsion system consists of four fan-jet engines mounted on the forward wing at the tips and at the mid-point of each semi-span. Each engine develops 199 005 N (44 738 lb) of thrust at sea-level static conditions. The landing gear system consists of two main gears and a single-strut, two-wheeled nose gear. Each main gear has a single shock-absorbing strut with a six-wheeled track. The main gears are located to provide stability at weight-empty conditions and are retracted into ventral pods mounted on the fuselage.

Constraints imposed by balance, stability, and aerodynamic performance in the location of the various aircraft components were recognized in developing this configuration and their effects are reflected in the shape of the area distribution curve shown on Figure 37. As in the case of the initial study configuration, a fuselage of essentially constant section is attainable and the addition of the various components matches the ideal distribution curve closely except for the area "bubbles" that occur at 25 percent and 75 percent of the body length. These area excesses could be eliminated by configuration refinement. However, this curve is considered to be sufficiently accurate for configuration analysis at this point of the study.

Mission fuel is located in integral tanks in the fore and aft wings and in the vertical tip fins.

3.2.2.2 Wing, Tip-Fin and Vertical-Stabilizer Structure

The boxed-plane structural system in Figure 38 consists of a swept-back forward wing mounted beneath the passenger deck at the forward end of the fuselage and a swept-forward aft wing mounted on the rear fuselage through a swept-forward vertical stabilizer. Wing separation is dictated by aerodynamic considerations which require the fore and aft wings to form an aerodynamically closed system through the use of swept-back vertical tip fins which form end plates. Rigid structural connections are provided for the interfaces of the wings and tip fins to enable carry-over of forces and moments.

The forward-wing planform gross area is 318.9 m^2 (3433 ft^2) and that of the aft wing is 268.4 m^2 (2889 ft^2), giving a total wing area of 587.3 m^2 (6322 ft^2). Of this amount, only 442.3 m^2 (4762 ft^2) belong to the basic wing, that is the region covered

Payload: 38 465 kg (84 800 lb)
 Range: 10 186 km (5500 n. mi.)
 Ramp weight: 301 592 kg (664 897 lb)
 Operating weight: 127 638 kg (281 393 lb)
 Mission fuel: 131 408 kg (289 704 lb)
 Basic wing area: 442.4 m² (4762 ft²)

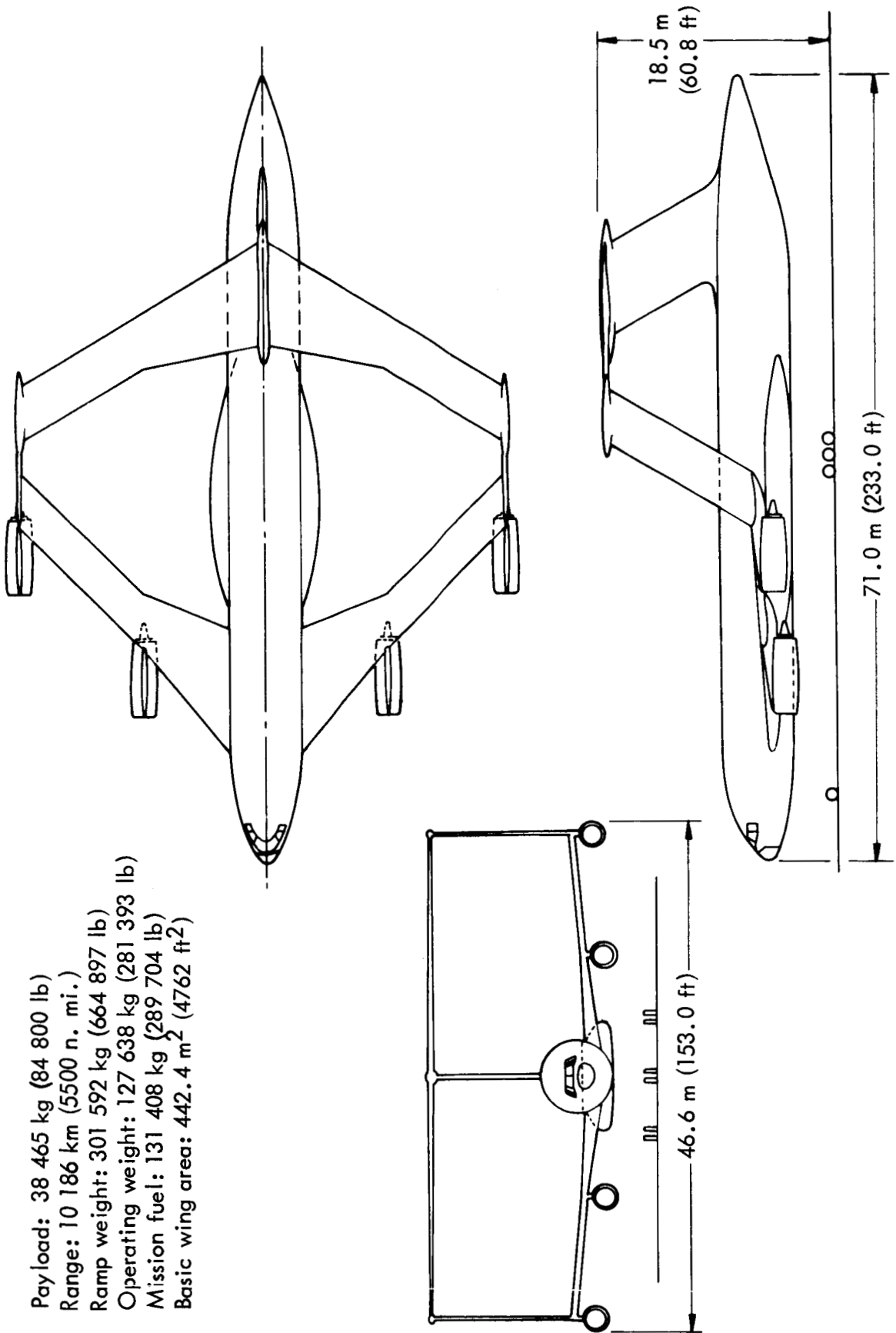


Figure 36. Selected interim configuration.

TABLE IV. INTERIM CONFIGURATION WEIGHT STATEMENT

Item	Weights	
	kg	lb
Forward wing	5 924	13 060
Aft wing	6 155	13 570
End plate	4 097	9 033
Vertical tail	6 386	14 079
Fuselage	26 748	58 970
Landing gear	11 898	26 231
Nose	1 428	3 148
Main	10 470	23 084
Nacelles/pylons	9 358	20 631
Nacelles	2 227	4 909
Pylons	2 566	5 656
Noise treatment	1 769	3 900
Thrust reversers	2 794	6 160
Propulsion system	17 811	39 266
Engines	14 104	31 093
Fuel system	1 647	3 631
Miscellaneous	2 060	4 541
Auxiliary power system	638	1 406
Surface controls	4 620	10 186
Instruments	602	1 327
Hydraulics and pneumatics	1 672	3 686
Electrical	2 545	5 611
Avionics	918	2 024
Furnishing	12 393	27 321
Air-conditioning	3 067	6 762
Weight empty	114 832	253 163
Operating equipment	12 804	28 229
Operating weight	127 637	281 393
Passenger payload	38 465	84 800
Zero fuel weight	166 101	366 192
Fuel	135 490	298 704
Takeoff gross weight	301 591	664 896

TABLE V. INTERIM CONFIGURATION GEOMETRIC CHARACTERISTICS

Wing area	448.1 m ² (4823 ft ²)
Aspect ratio	4.40
Wing span	44.4 m (145.7 ft)
Fuselage length	71.1 m (233.3 ft)
Forward-wing sweep	0.79 rad (45°)
Aft-wing sweep	-0.54 rad (-31°)
End plate area	133.1 m ² (1432.6 ft ²)
Vertical tail sweep	-0.52 rad (-30°)
Vertical tail area	83.7 m ² (901.1 ft ²)

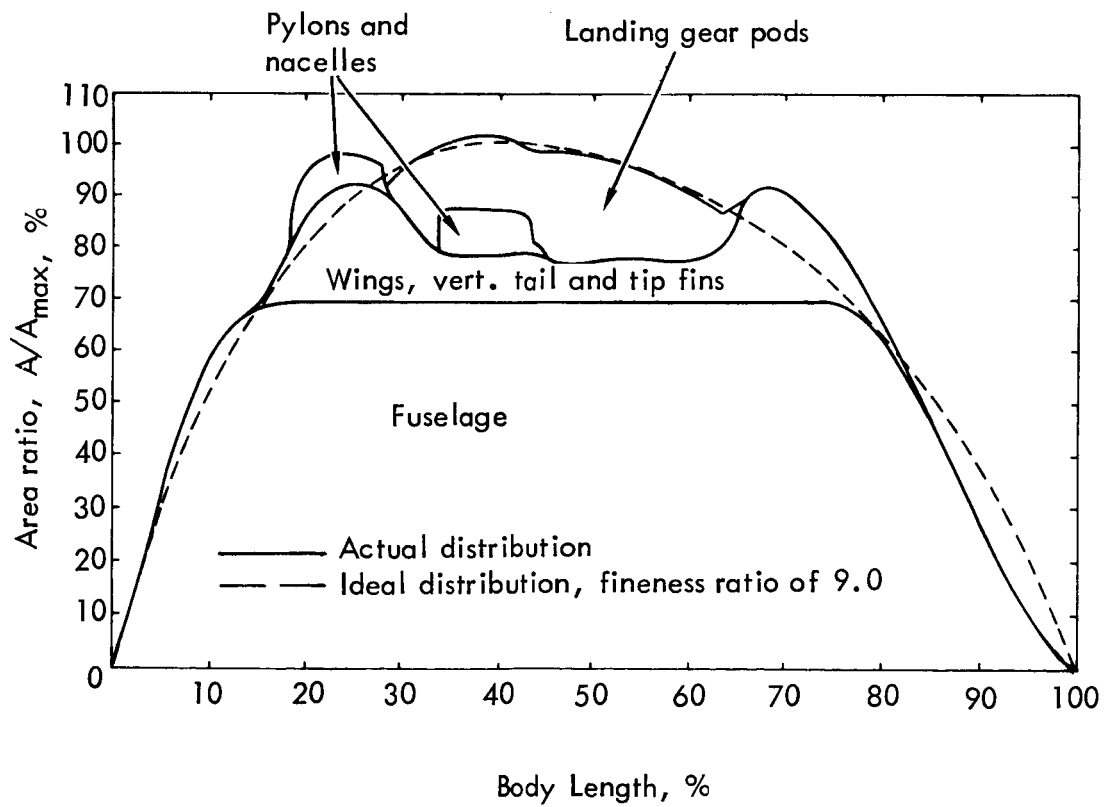


Figure 37. Area distribution for interim configuration.

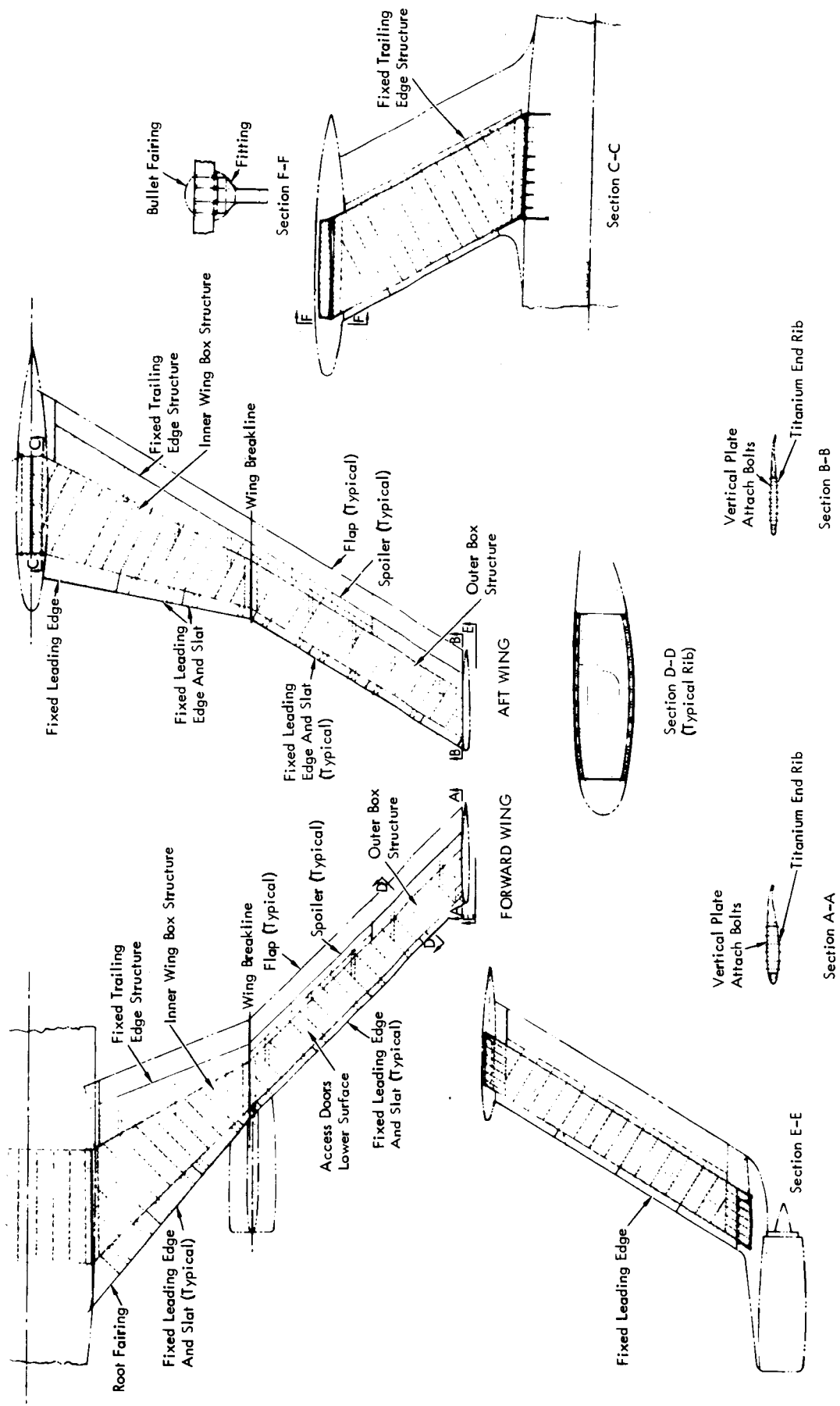


Figure 38. Boxed-plane structural system.

by the projection of the constant-chord outer panels to the centerline of the configuration.

Forward Wing - Designed in a two-panel planform, the forward wing is swept-back at a 0.79 rad (45°) angle at the panel quarter chord and has a thickness/chord ratio of 11.83 percent. The inboard panel has a taper ratio of 0.42 and a span equal to 50 percent of the wing semi-span. The outboard panel is of constant section.

Major structural elements of the inner and outer panels include two-spar, single-cell, primary boxes and leading- and trailing-edge structures. The front and rear spars for the outer panel are located at the 10-percent and 58-percent chord positions. On the tapered inboard panel, the front spar is located at the 10-percent position at the wing break and at the 19.4-percent chord position at the root section; the rear spar is at the 58-percent chord position at the wing break and at the 70-percent chord position at the wing root. Ribs in the primary-box structures are oriented normal to the front spars while flap support structures are located streamwise. Engine support structures are located at the wing break locations for the inboard engines and at the tips of the outboard panels for the outer engines. The primary box of the forward wing is designed to serve as an integral fuel tank for which access panels are provided on the lower surface.

A constant cross-section wing center-section structure is located in the forward fuselage structure to provide continuity of wing primary structure.

Aft Wing - The aft wing is swept-forward at a 0.54 rad (31°) angle, and has a thickness/chord ratio of 6.61 percent. This wing is similar in design to the forward wing in that it has a two-panel planform with constant-chord outboard panels. Unique characteristics of the inboard panel include a taper ratio of 0.53 and a reduction in the sweep forward to 0.29 rad (16.5°) at the planform quarter-chord position.

The primary box structure of the inboard wing is arranged to match the primary structure of the vertical stabilizer which provides the principal means of support for the aft wing. This requires the wing-root locations of the front and rear beams in the aft wing to be at the 12.7-percent and 66-percent chord positions, respectively. Due to the taper of the inboard panels, the front and rear beams of the aft wing are at 10 percent and 58 percent of the chord at the wing break station, respectively. In the constant-section outboard panels, the beams are maintained at the same chord locations as at the wing break station, which occurs at the mid-point of the wing semi-span.

The primary-box rib structures are oriented normal to the rear spars in both panels, and slat and leading-edge structures are oriented normal to the leading edge. The trailing-edge fixed structures are arranged normal to the rear spars and all flap support structures are located streamwise.

The aft wing attachment to the vertical stabilizers is by means of multi-tongued fittings located on the front and rear spars as illustrated on Figure 38.

Vertical Stabilizer - A constant-section, $0.52 \text{ rad } (30^\circ)$ swept-forward, single-cell, primary-box vertical stabilizer provides the principal means of support for the aft wing. The box structure has front and rear spars located at 5 percent and 65 percent of the chord, respectively. The structure forward of the front spar comprises the fixed leading edge, and the trailing edge is made up of a hinged rudder and fixed trailing-edge structures. Attachment of the vertical stabilizer to the fuselage is by means of primary attachment fittings at front and rear spar frames with secondary attachments at intermediate frames.

The vertical stabilizer area is $85.4 \text{ m}^2 (919 \text{ ft}^2)$ and the thickness/chord ratio is 10 percent.

Vertical Tip Fins - The wings are connected at their tips by vertical fins swept-back $0.52 \text{ rad } (30^\circ)$ to form a closed-box system. The tip-fin structures consist of single-cell primary boxes having front and rear spars located at 10 percent and 62 percent of the chord, respectively. The fins are of constant section and have a thickness/chord ratio of 6 percent and an area of $64.8 \text{ m}^2 (697 \text{ ft}^2)$. The internal rib structures are oriented normal to the front and rear spars, and the structural box is designed to serve as an integral fuel tank. Transitional structures are provided at the upper and lower ends of each wing to facilitate mating the vertical fins with the wings.

The structure forward of the front spar consists of a fixed leading-edge structure. On the trailing edge there is a full-span hinged control to generate side force, and there is also a fixed fairing between the control surface leading edge and the rear spar of the wing.

Materials and Construction - All primary structures are fabricated using graphite epoxy. A typical assembly consists of molded graphite-epoxy skins, stringers, and ribs bonded to form an integrated structure. Titanium is used for shims and embedments where required to provide attachment structures. Diffusion-bonded titanium fittings are used where dictated by loading conditions in areas such as landing gear support structures and attachment of the wing and fuselage, the wing and stabilizer, and the fuselage and stabilizer. Secondary structures, such as leading and trailing edges, are assembled from graphite epoxy, "E" and "S" glass, and PRD-49 used in conjunction with honeycomb cores. These structures are molded and bonded to form integrated structures.

3.2.2.3 Fuselage Structures and Internal Layout

The fuselage is sized to provide accommodation for 400 passengers on a single deck. The fuselage is $71.1 \text{ m } (233.3 \text{ ft})$ long and $43.2 \text{ m } (141.7 \text{ ft})$ of it exists as a constant cylindrical section, having a diameter of $6.6 \text{ m } (21.67 \text{ ft})$. Figure 39 presents a layout of the passenger flight deck which is designed to current wide-body jet standards of comfort and has an accommodation split of 20-percent first class and 80-percent tourist class passengers. First-class accommodations are arranged 7 abreast on $0.97 \text{ m } (3.17 \text{ ft})$ seat pitch and tourist accommodations are 9 abreast at $0.86 \text{ m } (2.83 \text{ ft})$ seat pitch. Comfort stations, galleys, and stowage space are provided in both compartments, and 4 type "A" doors are located on each side of the fuselage.

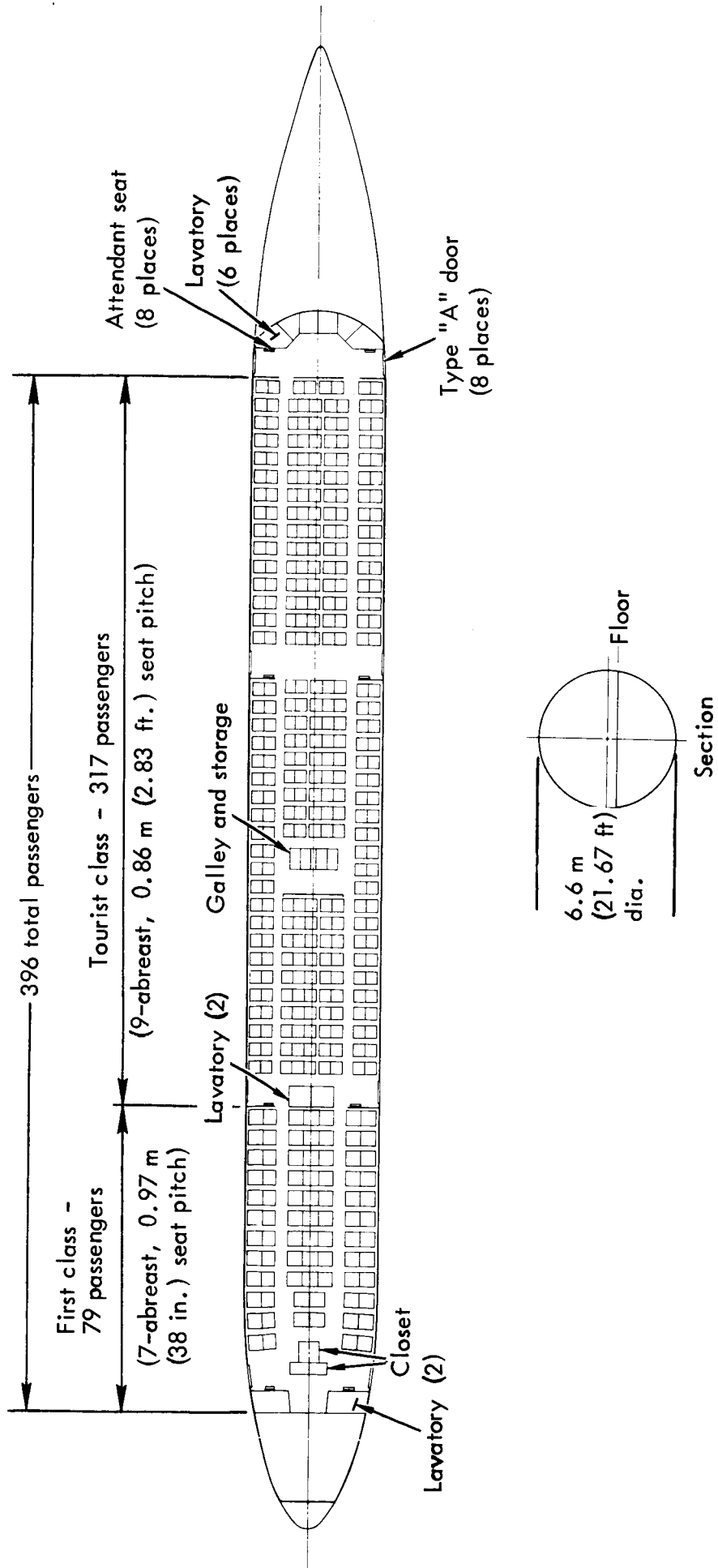


Figure 39. Fuselage interior arrangement.

The fuselage structure shown on Figure 40 is divided into nose, center, and aft fuselage components. The constant-section center fuselage, the largest of the three components, is further divided into major segments to facilitate production. The structure includes structural shells, longerons, passenger and baggage compartments, floors and beams, main frames, bulkheads, landing gear structures, and vertical-tail support structures.

The nose fuselage includes the flight deck and nose landing-gear stowage space and structure and also accommodates the forward portion of the passenger deck.

The forward wing is attached beneath the passenger deck at the forward end of the center fuselage. Mounting structure and stowage volume for the main landing gears are located at approximately the middle of the center fuselage. Pods are required to envelope the main landing-gear structures and to provide space for systems and APU's.

The aft fuselage accommodates the rear portion of the passenger deck and provides the mounting and attachment structure for the vertical stabilizer for the aft pressure bulkhead. The mounting structure for the vertical stabilizer impacts upon the passenger seating arrangement due to the large depth of the vertical stabilizer spar frames.

A typical shell structure consists of a bonded assembly of graphite-epoxy composite skins, shear clips, and ring frames. Portions of the structure in the region of window cut-outs utilize titanium which is also used for the manufacture of the major frame structures.

3.2.2.4 Flap Mechanisms

Nested Fowler-type double-slotted flaps are installed on the trailing edges of both wings. The flaps are divided into six spanwise segments for each wing, with three segments to each semi-span. Initial motion of each segment is translational and provides an increase in wing area by extending the wing chord a maximum of 19 percent. This motion is followed by a rotation to provide up to a maximum deflection of 0.70 rad (40°) on the high-lift flaps. Each inboard and tip segment has an articulated trailing edge providing ± 0.35 rad (20°) of rotation for longitudinal and lateral control at any translated position of the flap assembly.

The arrangement of the devices shown on Figure 41 requires the wing rear-beam location to be at 58 percent of the local chord on the outboard panel of the wing and varies the location from 58 percent at the break to 70 percent at the root of the wing inboard panel. The illustrations of Figure 41 relate to the inboard flap/elevator segments and are typical for the remaining segments.

The main support rollers for each flap segment are fixed within the wing-box structure adjacent to the wing rear beam. The box rail structures are driven by means of an actuator connected to the main flap carriage and are arranged to roll on the fixed position rollers to produce translational motion of the box rails. The main flap segment rollers are mounted on each flap carriage and each flap is driven through a

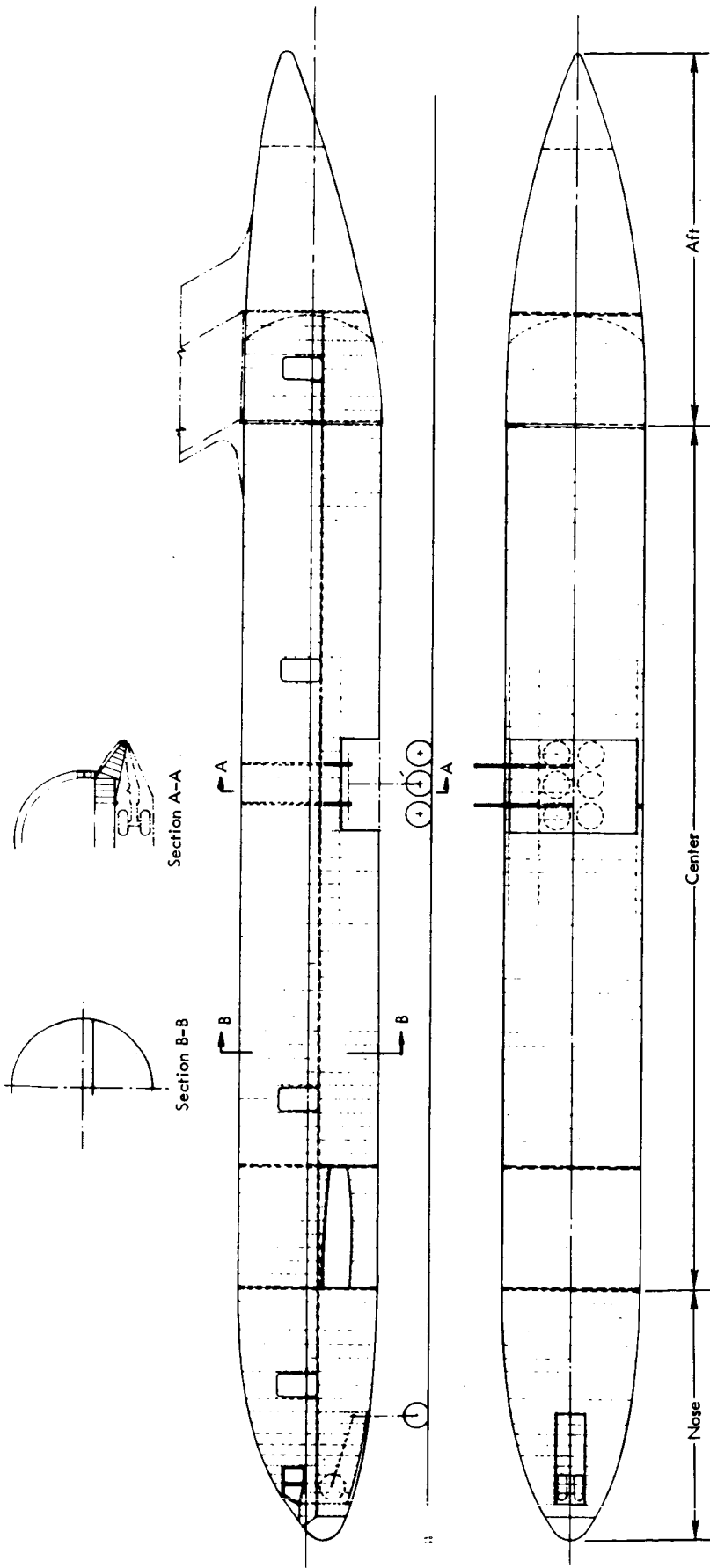
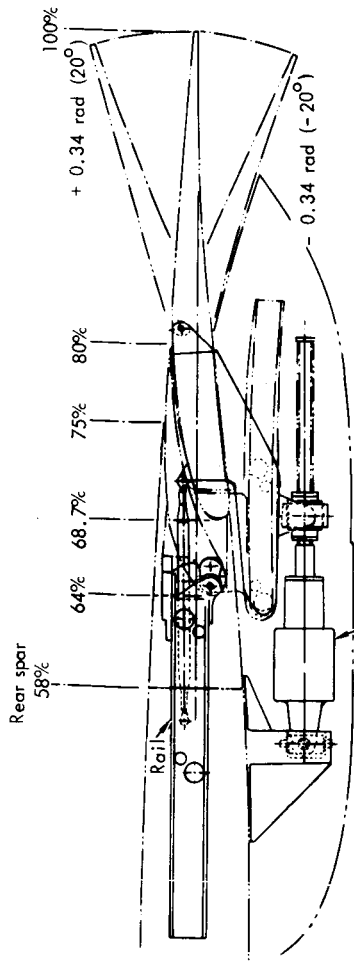
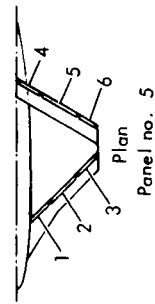


Figure 40. Fuselage structural layout.



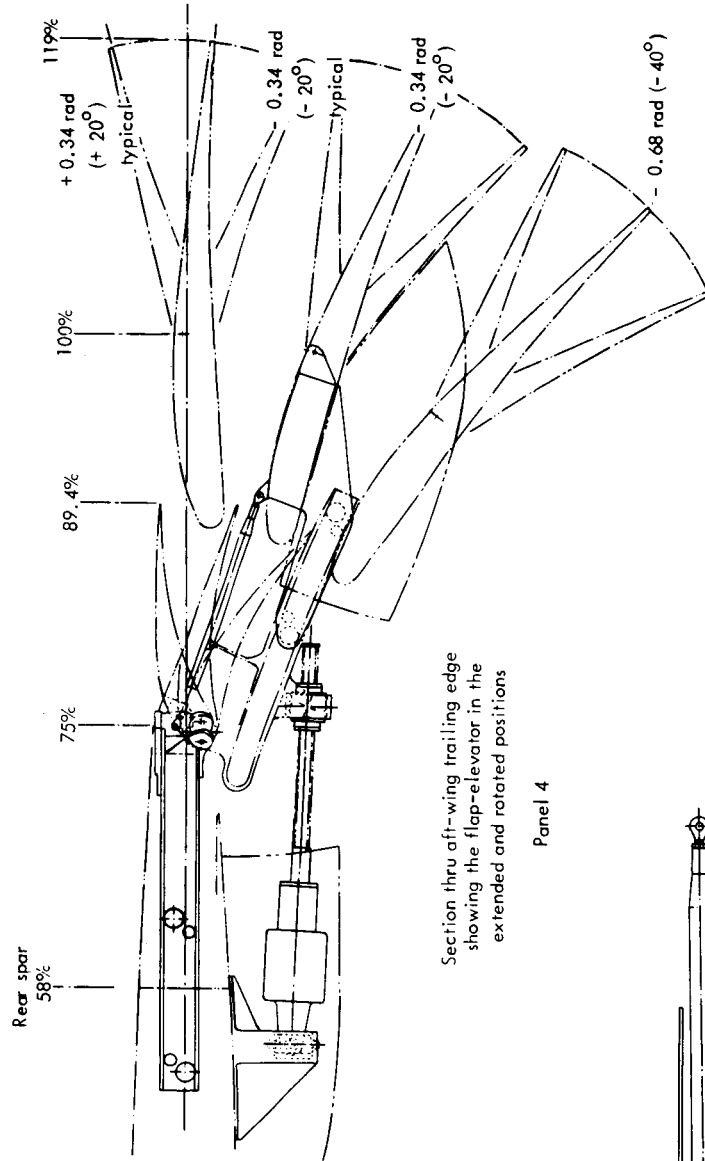
Section thru aft-wing trailing edge showing the flap-elevator in the up position

Panel 4



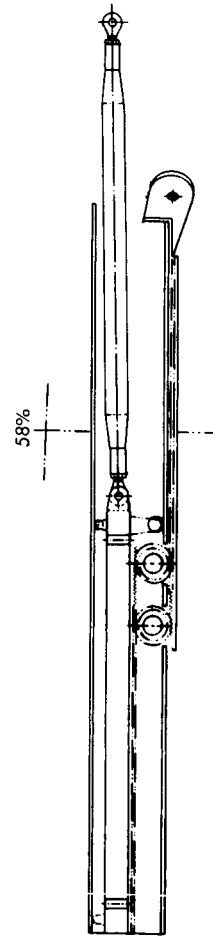
Panel no. 5

Panel	Low speed case		Take-off		Landing		Trim
	Extension	Rotation	Extension	Rotation	Extension	Rotation	
1	1%	0 rad deg	1%	0.43 rad 25°	1%	0.43 rad 25°	-0.34 rad 20°
2	1%	0 rad deg	1%	0.34 rad 20°	1%	0.48 rad 40°	
3	1%	0 rad deg	1%	0.43 rad 25°	1%	0.43 rad 25°	
4	1%	0 rad deg	1%	0.34 rad 20°	1%	0.34 rad 20°	-0.34 rad 20°
5	1%	0 rad deg	1%	0.34 rad 20°	1%	0.48 rad 40°	
6	1%	0 rad deg	1%	0.34 rad 20°	1%	0.34 rad 20°	



Section thru aft-wing trailing edge showing the flap-elevator in the extended and rotated positions

Panel 4



Section thru rail

Figure 41. Trailing edge device and surface panel position.

fixed link by means of a pair of parallel racks, one of which is mounted in a fixed location on the wing structure. Motion of the actuator is transferred to the box rail and thence through the racks and associated pinions to cause translational motion of the flap in such a manner that one inch of actuator and rail motion causes two inches of motion at the flap. At full extension the box rail becomes locked and sequencing devices enable the actuator to reverse direction to provide rotational motion of the flap.

In the case of the inboard and tip flap segments, the articulated trailing edges are operated by means of an integrated duplex actuator package which is mounted on the lower surface of the main flap segments.

3.2.2.5 Landing Gear

The landing gear system consists of a two-wheeled, single-strut nose gear and two single-strut six-wheeled main gears - all utilizing a common wheel and tire size.

Main Gears - Each main gear, as shown in Figure 42, consists of a single-action strut and a six-wheeled truck. The mass distribution of the biplane arrangement requires the incorporation of long-stroke struts into the gears to ensure that low reaction factors at the gears are generated and that landing gear loads do not create the principal design conditions for the fuselage. The main gears have a free-fall capability and are located to provide a tail-down clearance angle of 0.21 rad (12°) and to be within tip-over angle tolerance. Retraction of the gears is laterally inboard through a four-bar linkage. Gear locking is accomplished by an over-center linkage and through internal locks in the actuators.

Nose Gear - A double-acting strut is used for the nose gear shown in Figure 43 in order to reduce the gear reactions during dynamic braking and pitching motions. The gear retracts forward and has free-fall capability. Retraction is accomplished through a four-bar linkage driven by an actuator containing internal locking devices. Nose gear steering is accomplished with a rack and pinion mechanism.

3.3 STRUCTURAL ANALYSIS

The configuration shown earlier in Figure 6 was selected for the initial analysis of the transonic biplane structure. Continuous structure was used at the intersections of the wing tips and tip fins, of the forward-wing root and fuselage, and of the aft-wing root and vertical fin. The objective of the continuous structure at these intersections was to develop fixed end moments which in effect would distribute the wing bending moment between the root and tip of the wing-box structure. This arrangement should result in significantly lower wing-box weights than an equivalent cantilevered monoplane wing box.

Weights of the biplane wing structure could not be estimated with conventional weight-estimating techniques because of the redundant load paths and the unknown stiffness requirements for flutter prevention. The study plan was to develop parametric

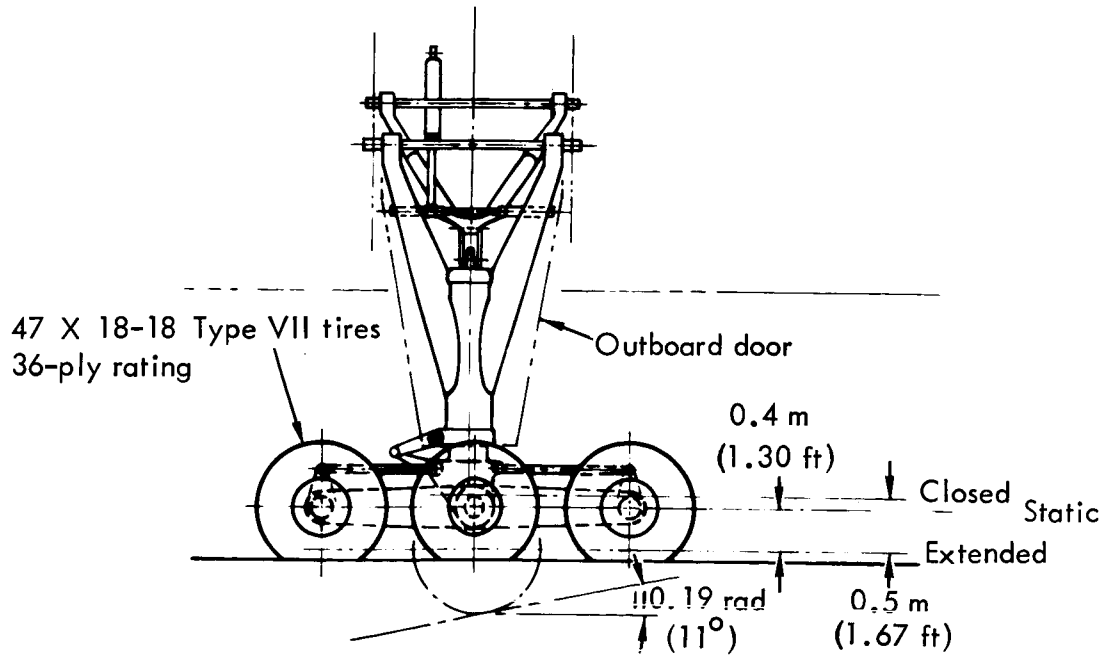
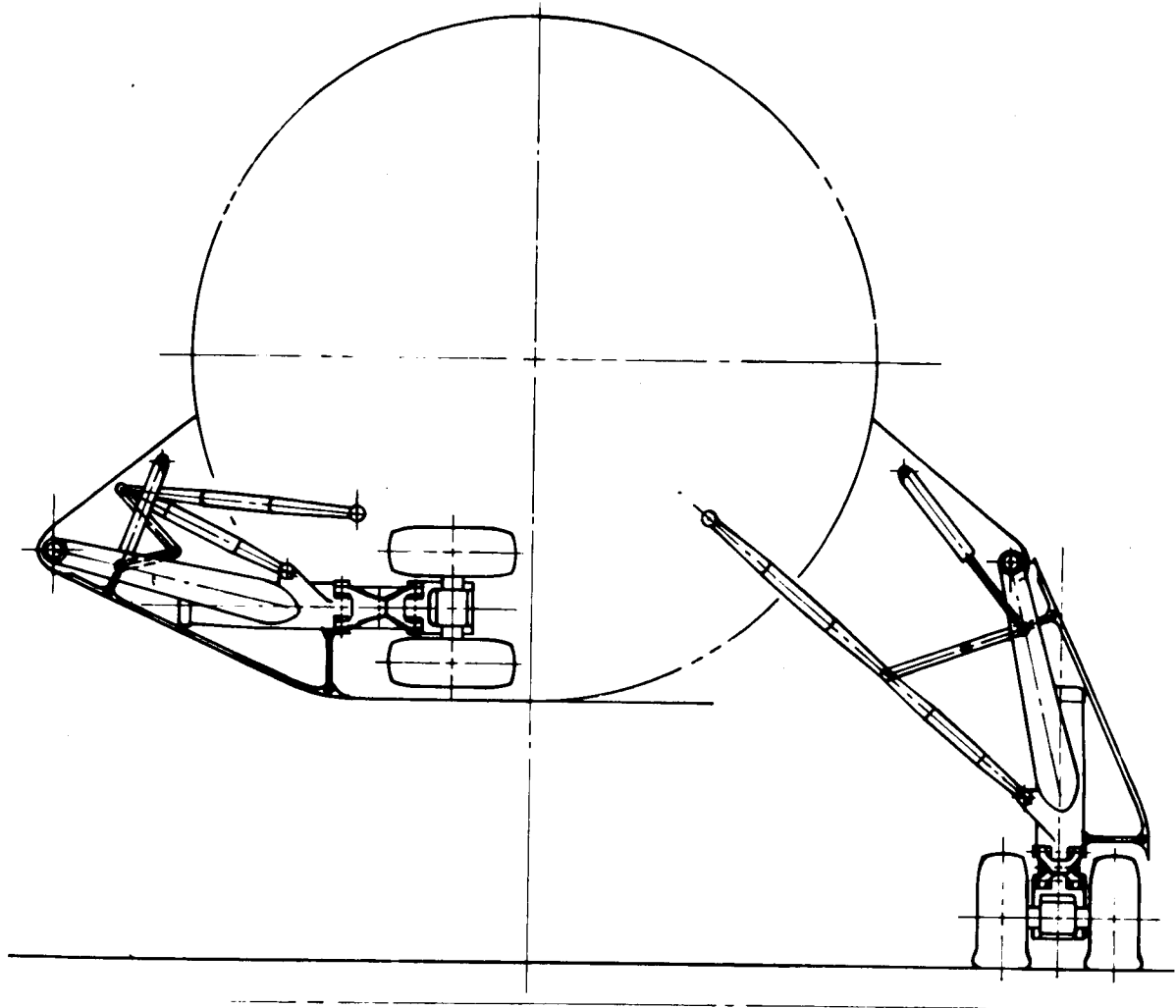


Figure 42. Main landing gear.

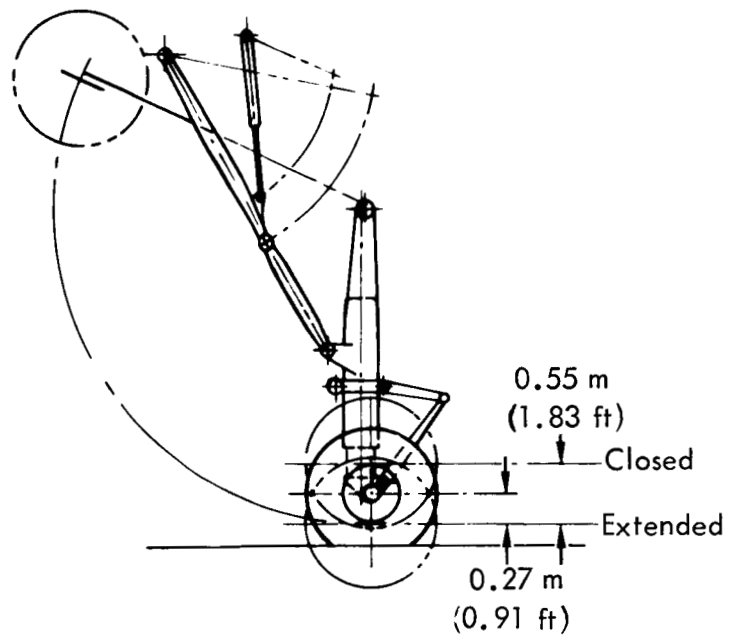
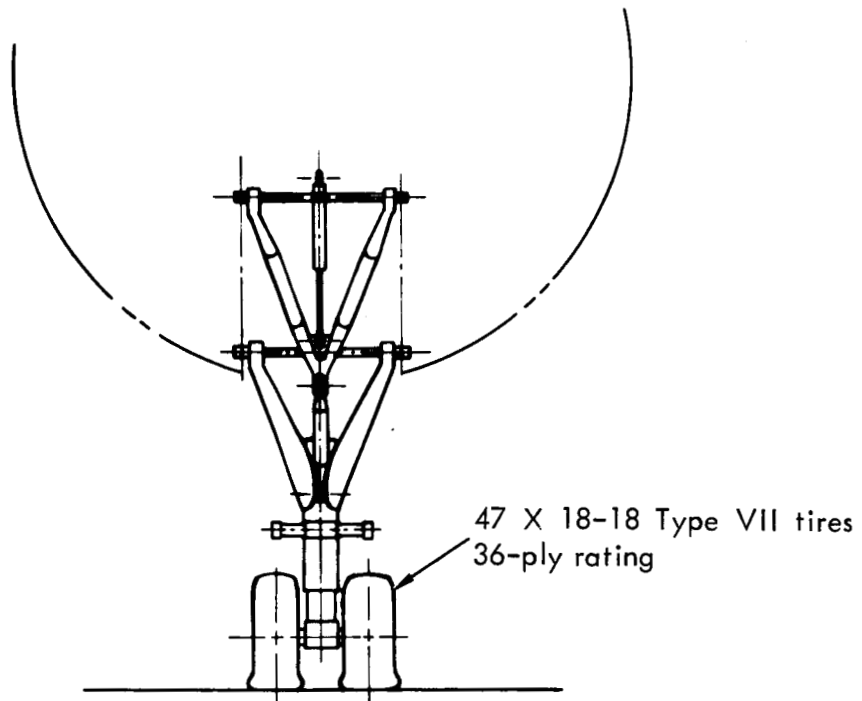


Figure 43. Nose landing gear.

weight equations by sizing a baseline configuration for static loads; and once this was completed, check the baseline for flutter. Points for developing parametric weights were obtained from variations of wing taper and wing bat area. A simplified finite-element model was set up to compute the load distributions in the redundant biplane structure. Structural sizes, moments of inertia, weights, applied air loads, inertial loads, and stiffnesses (EI and GJ) were estimated for each increment of the wing, fuselage, vertical fin, tip fin, and engine pylon structure between the node points in the finite element model. Iterations were made to adjust the structural sizes and stresses to the internal load distributions. Structural sizing and analyses of five configurations were completed during Phase I of this study and these are shown as designs 1 through 5 on Figures 44 and 45. The results of the static analysis did show the biplane wing box to be lighter than a cantilevered monoplane as was earlier projected.

A single flutter analysis of the baseline was planned to show that the stiffer biplane wing with rigidly held tips would have adequate margins for flutter. This, however, was not the case; and the flutter analysis indicated relatively low flutter speeds. As a result, numerous in-depth structural analyses and configuration changes were made in an attempt to resolve the low flutter speeds. These analyses are discussed in more detail in Section 3.3.4.

The design loads criteria, structural modeling approaches, parametric weight program, and flutter analysis are discussed in the following sections.

3.3.1 Design Loads Criteria

Reference 15 was used to define the structural design requirements for the transonic biplane. Briefly, the design criteria were as follows:

Design Speeds (see Figure 46)

$$V_C/M_C: 193 \text{ m/sec (375 kts) CAS/M} = 0.95$$

$$V_D/M_D: 225 \text{ m/sec (437 kts) CAS/M} = 1.01$$

Limit Load Factors:

Maneuver: 2.5 to -1.0 g's

Landing: -1.5 g's

Taxi: -1.5 g's

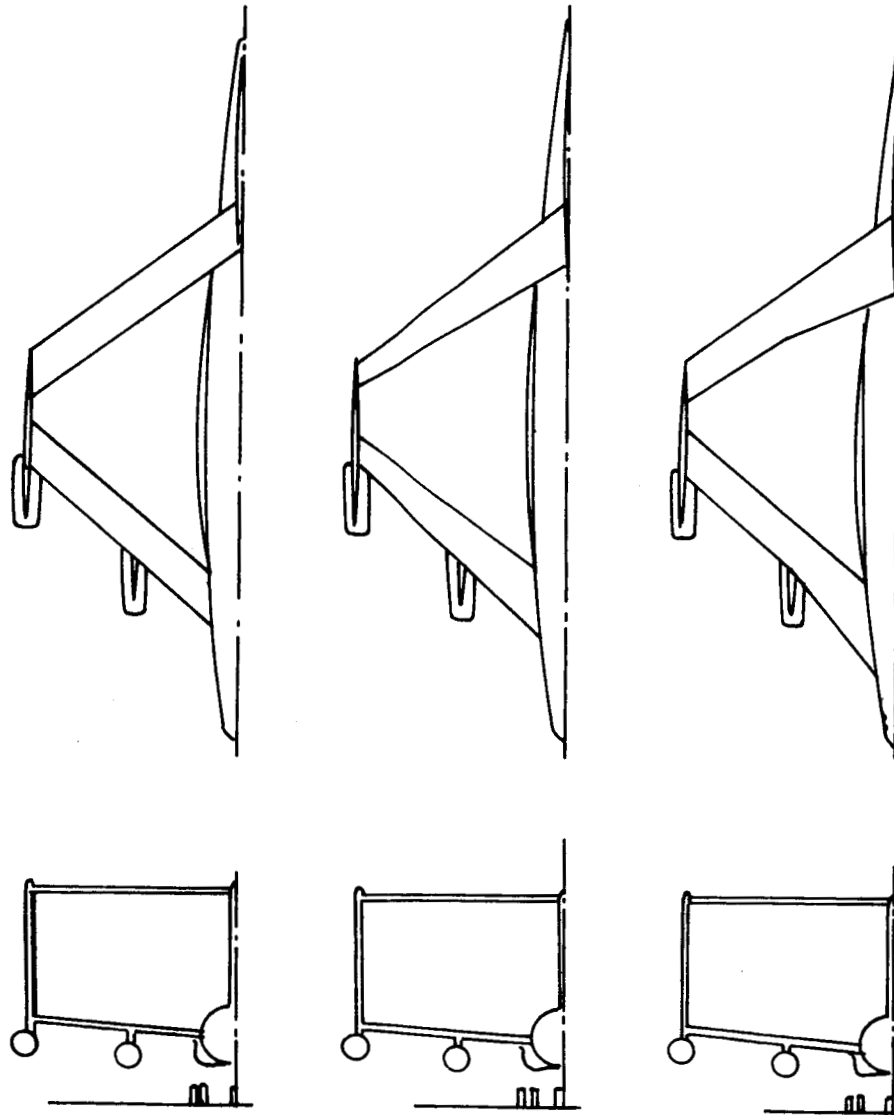
Braking: 0.8 braking coefficient

Design Weights (derived from ATT for initial configuration)

Maximum takeoff: 302 284 kg (666 422 lb)

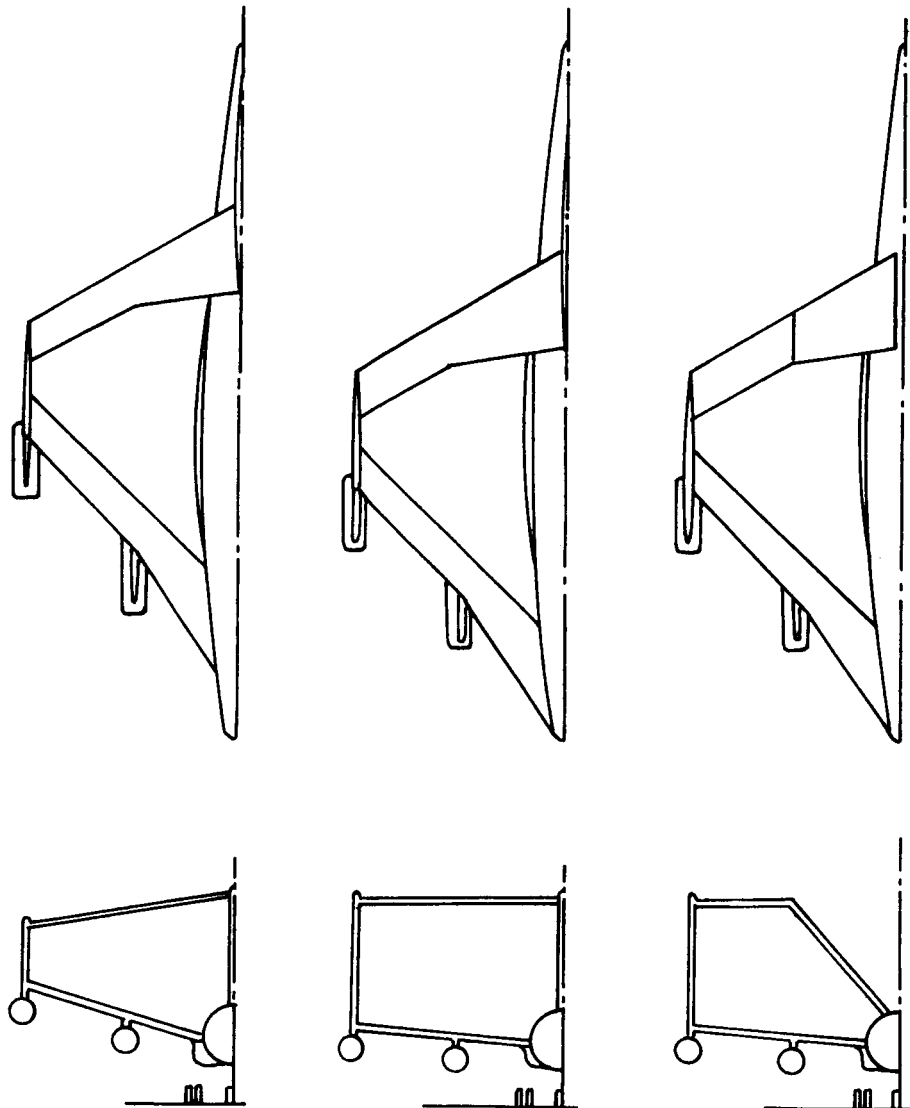
Maximum zero fuel: 166 014 kg (365 998 lb)

Landing: 209 560 kg (462 000 lb)



1. Initial configuration 2. Taper ratio = 0.4
 Taper ratio = 1.0 3. Batted wings

Figure 44. Configurations used for structural analysis.



- 4. Flutter improved configuration
- 5. Aerodynamic improved configuration
- *6. Alternate configuration

* Accomplished in Phase II.

Figure 45. Additional configurations used for structural analysis.

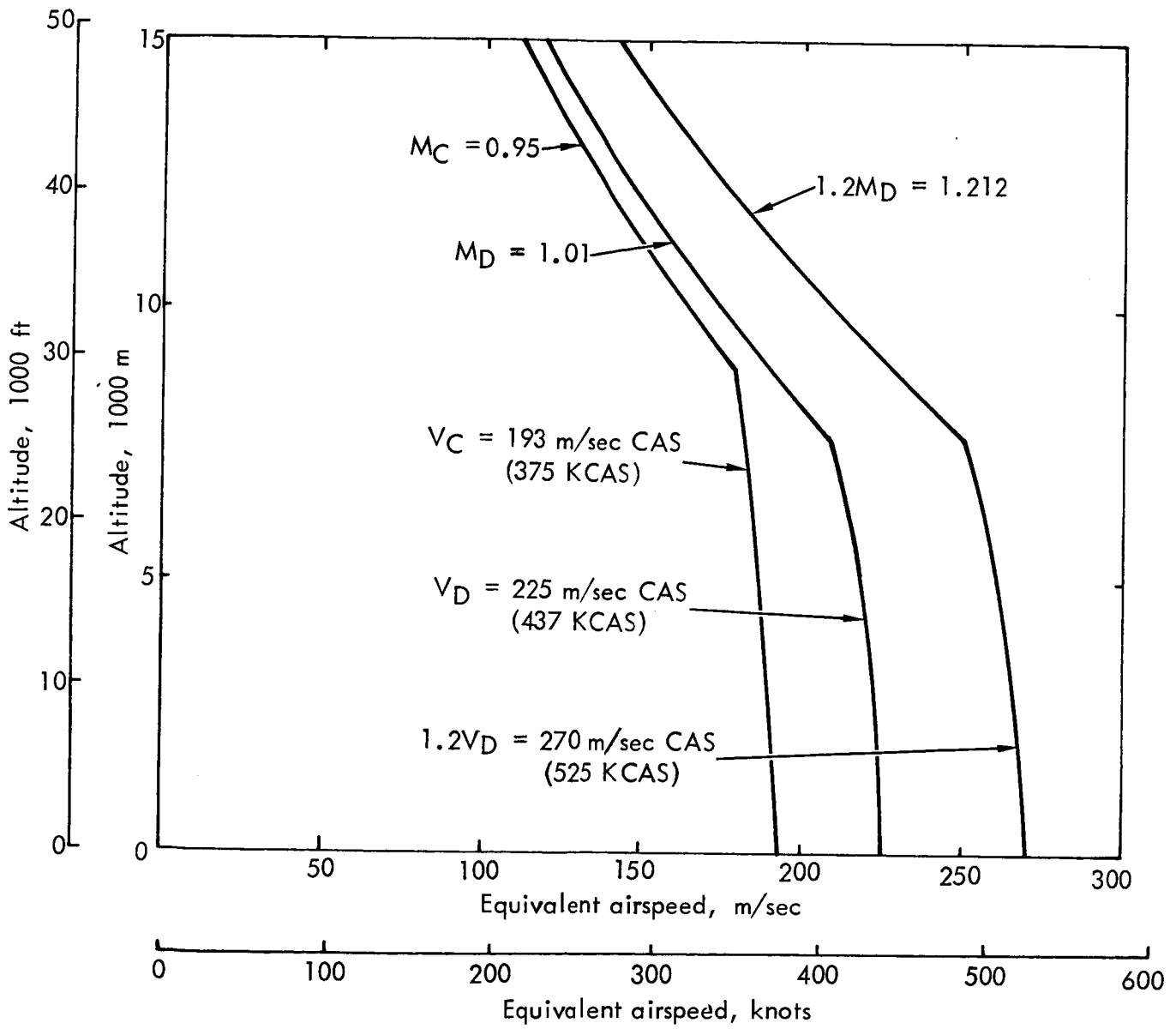


Figure 46. Structural design airspeeds.

Center-of-Gravity Range: 12 to 27 percent MAC

Cabin Pressure: $67\ 570\ \text{N/m}^2$ ($9.8\ \text{lb/in}^2$)

Advanced filamentary composites were assumed to be applied to approximately 60 percent of the airframe structure. Ultimate stresses were held to levels which provided adequate fracture and fatigue resistance for a long life commercial transport.

3.3.2 STRUCTURAL MODELING CONCEPTS AND RESULTS

Structural models of the various configurations previously shown in Figures 44 and 45 were developed using the finite element Flutter and Matrix Algebra System (FAMAS) program. The models were constructed using beam elements. These elements are vector elements (nodes n to $n+1$) and carry shear and bending in two perpendicular planes normal to the element axis, plus axial load parallel to the axis, and torsion about the axis. The required inputs are the shear and tensile moduli of elasticity, cross-sectional areas, and moments of inertia. A typical model is shown in Figure 47.

The wing planforms were laid out and the front and rear spars were located at 15 percent and 65 percent of the wing chord except on the battled wing configurations. The wing elastic axis was selected halfway between the front and rear spars, and properties were calculated based on cuts normal to the elastic axis. The vertical stabilizer properties were calculated in a like manner. A typical wing planform and cross section are shown in Figure 48. The axes for the elements representing the fuselage were taken at the fuselage center line.

Loads on the model were derived using the lift-distribution data for a 2.5-g maneuver condition and balancing this lift with distributed vertical inertia loads on the wings, fuselage, engine pylons, tip fins, and vertical stabilizer. This is achieved using the best estimate of the airplane mass distribution and is adjusted to provide a pitching-moment balance as well as a vertical balance. Minor unbalances in the pitch and vertical moment and load were reacted at a node on the fuselage approximately halfway between the forward and aft wing roots. Lateral loads were applied to the tip fins. These loads were symmetrically opposed; therefore, they were inherently balanced. A typical spanwise lift distribution for a 2.5-g maneuver condition and tip-fin loading is shown in Figure 49. The final input loads at the model nodes were multiplied by 1.5 to reflect ultimate loads.

Section properties of the fuselage and engine pylon members were based on statistical estimates of structural member sizes. Section properties of the wings, tip pylons, and vertical stabilizer were based on cover sizing and reflect cover stresses due to primary bending of $3.45 \times 10^8\ \text{N/m}^2$ (50 ksi) tension or compression. These cover stress levels were obtained by iterating the FAMAS analysis and resizing the cover skins until the desired stresses were achieved. It was assumed that graphite-epoxy could be laminated to provide strength properties identical to those of aluminum; therefore, properties of aluminum were used on the model. The definition of \bar{t} is the equivalent cover thickness considering both skin and stringer materials combined. It was assumed that the value of t , the thickness, of the skin and spar web was $2/3$ the

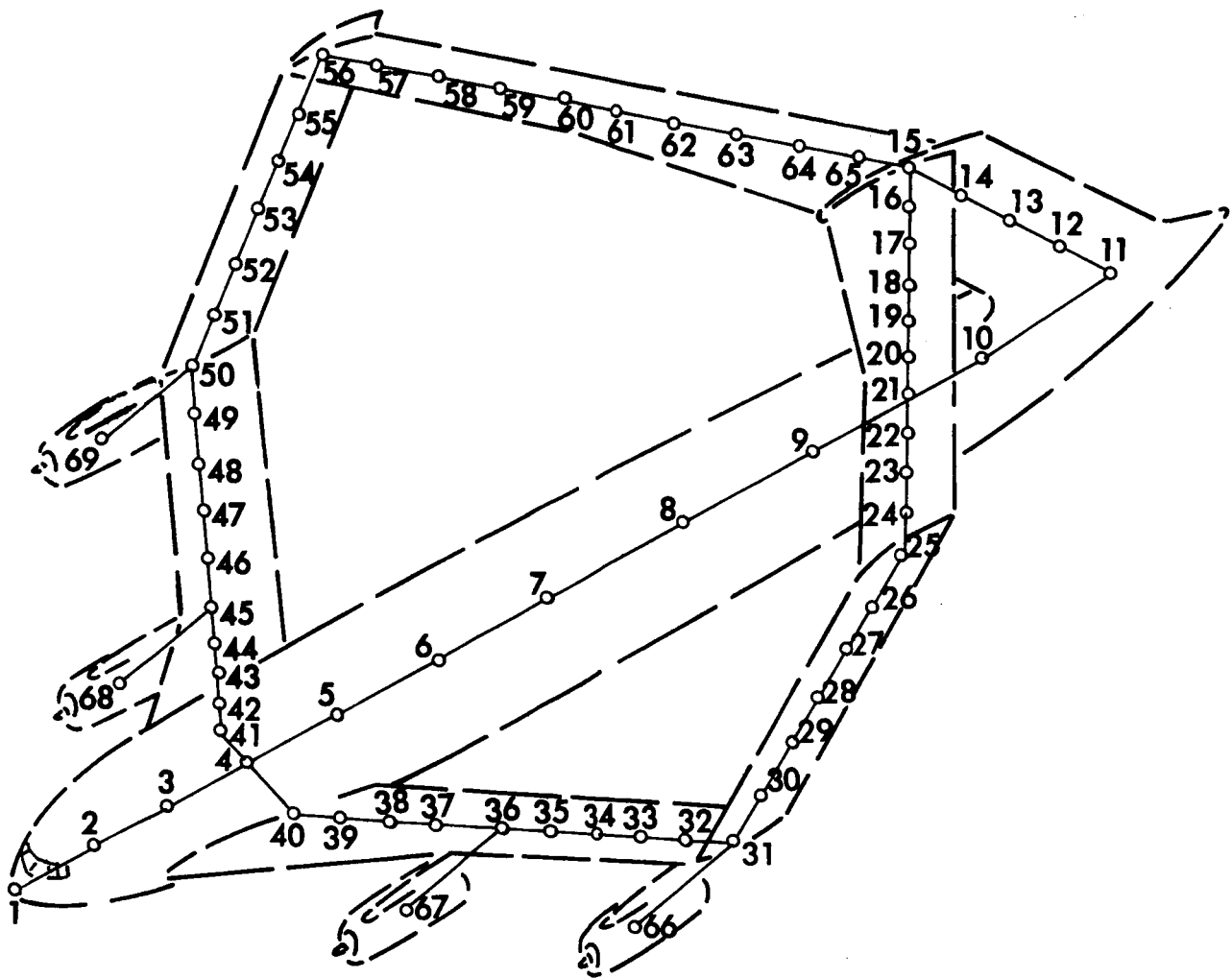
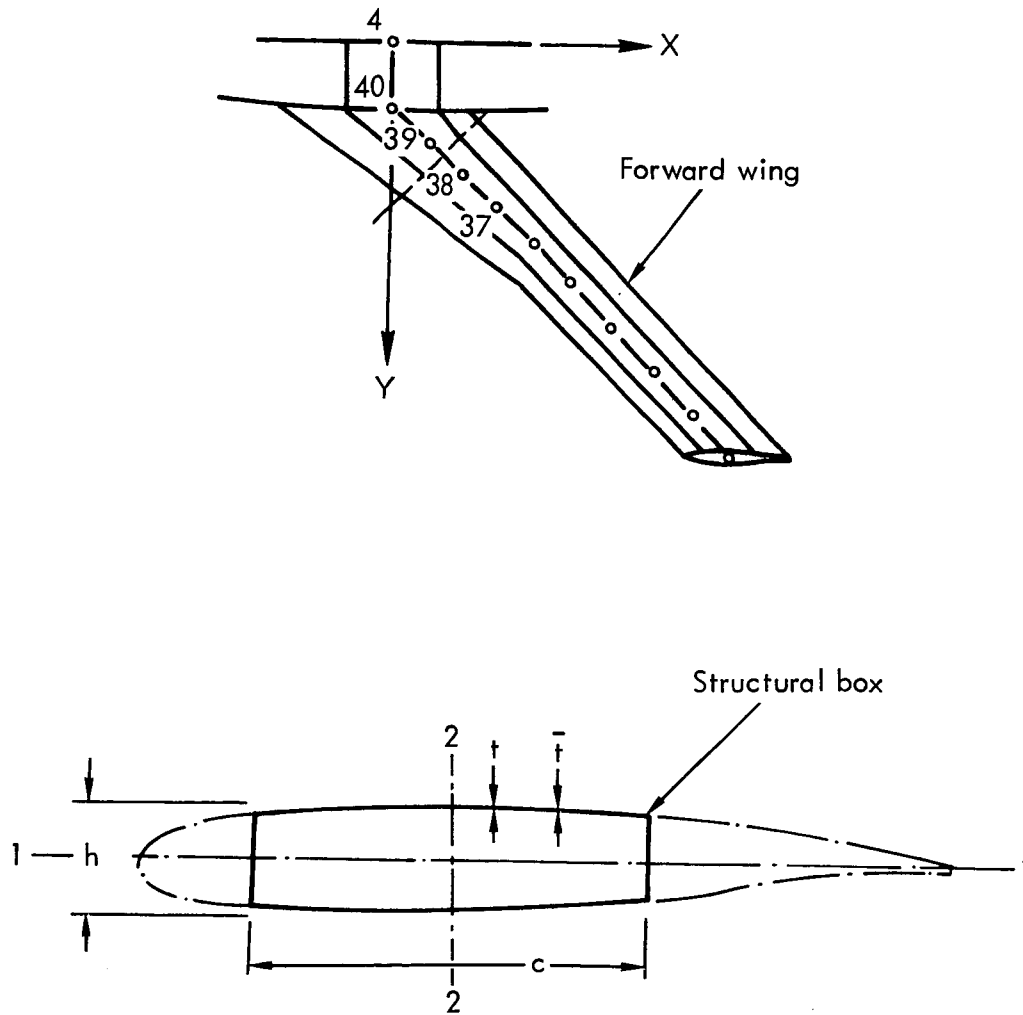


Figure 47. Typical finite-element FAMAS model.



$$t = 0.67 \bar{t}$$

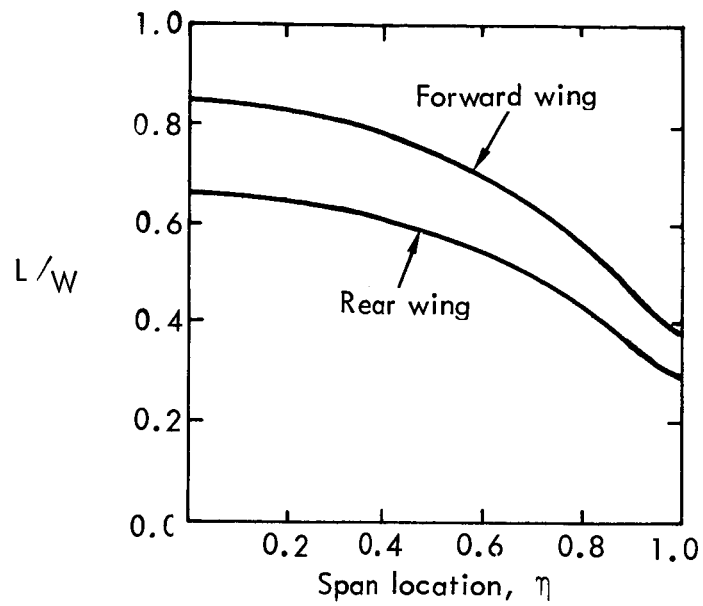
$$A = (2)(c)(\bar{t}) + (2)(h)(t)$$

$$I_1 = ch^2 \bar{t} / 2$$

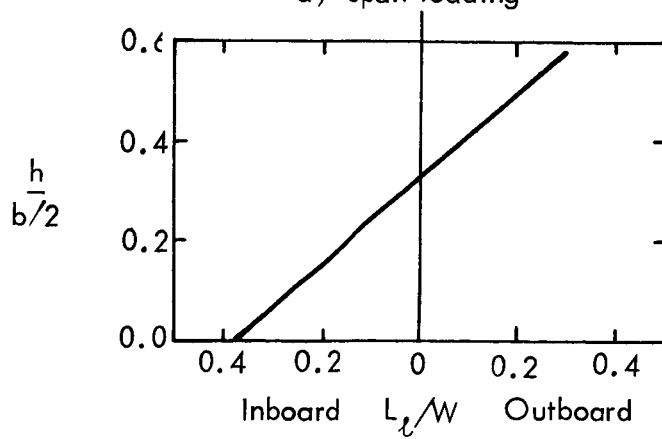
$$I_2 = c^3 \bar{t} / 6 + c^2 ht / 2$$

$$J = (ch)^2 2t / (c + h)$$

Figure 48. Typical wing planform and structural box cross section.



a) Span loading



b) Tip-fin loading

Figure 49. Typical wing and tip-fin lift distribution.

value of \bar{t} . The forward and aft wings each contain a bending inflection point where the bending moment goes to zero. The sections adjacent to these inflection points were given a minimum \bar{t} of 0.00254 m (0.1 in.).

The output from the FAMAS program includes internal loads in terms of shears, moments, axial loads, and torsion on each element. In addition, nodal deflection and rotation are also output. Typical bending moment, deflection, and twist of the forward and aft wings plus a plot of \bar{t} resulting from sizing based on an approximate maximum bending stress of $3.45 \times 10^8 \text{ N/m}^2$ (50 ksi) are shown in Figures 50, 51, 52, and 53.

In a practical wing box designed for production, the variation in skin thickness would be more uniform, and possibly, approach a constant thickness for the outer 75 percent of the wing span. This could offer an advantage for lower production costs.

3.3.3 PARAMETRIC WEIGHT PROGRAM

The computer program developed during the ATT study (Reference 4) for configuration sizing and performance was modified for use during this study. Weight estimation logic was incorporated into the program to reflect the effects of a biplane configuration using the ATT monoplane as a basepoint. The logic was arranged to provide branching such that biplane as well as monoplane configurations could be estimated using the same program with a configuration input code. Added structural stiffness above that required for strength and producibility constraints was ignored under the assumption that flutter suppression would be accomplished through active control devices. (This assumption did not prove to be valid as described in the Phase II section of this report.) The composite weight factors for the various weight groups, as derived from the ATT studies, are identified in Table VI. The biplane weight effects incorporated in the computerized weight-estimation logic are described in the following paragraphs.

3.3.3.1 Wing and Tip-Fin Weight

It was recognized that the structural redundancy of the biplane forward and aft wings would cause them to exhibit different weight sensitivity to the airplane design parameters than would be the case for a monoplane wing. Lockheed's FAMAS program, as discussed in section 3.3.2, was used to analyze the number 1, 2, and 3 configurations in Figure 44. The structural member sizes obtained from the FAMAS program were then used to derive wing and tip-fin box weights with the secondary structure being derived from contemporary aircraft unit-weight data. These resulting analytically-based weights were then compared to the parametric wing weights using the monoplane weight-estimation logic with lift distribution factors approximating the load on each wing. The initial tip-fin relationships used an arbitrary 143.6 N/m^2 (3 psf) unit weight for the aluminum weight basis. The resulting comparison of these weight values is shown in Table VII. In this table, the weights based upon the FAMAS analyses are shown in data set A, the results from using the initial parametric relations are shown in data set B, and the weights derived from the modified parametric relations are shown in data set C. The factors used to modify the initial parametric relations are shown by the "K" values shown by each item in data set C. Comparison of the resulting data set C

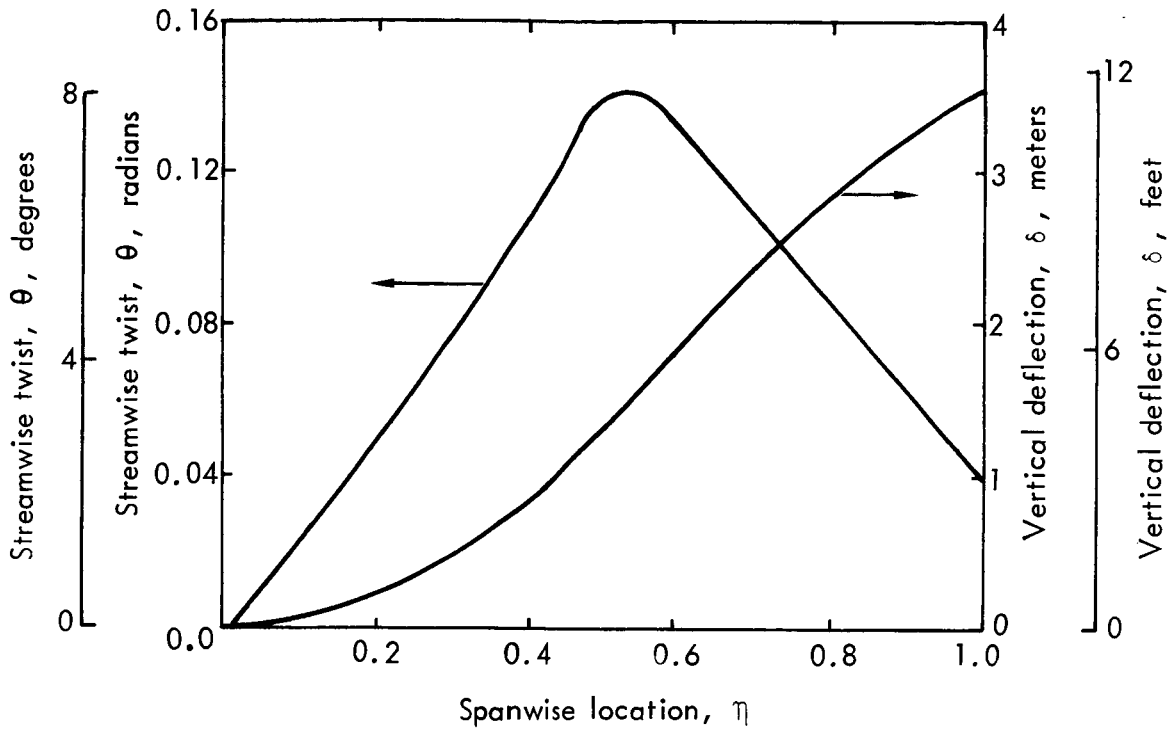


Figure 50. Vertical deflection and streamwise twist for forward wing of Configuration 1

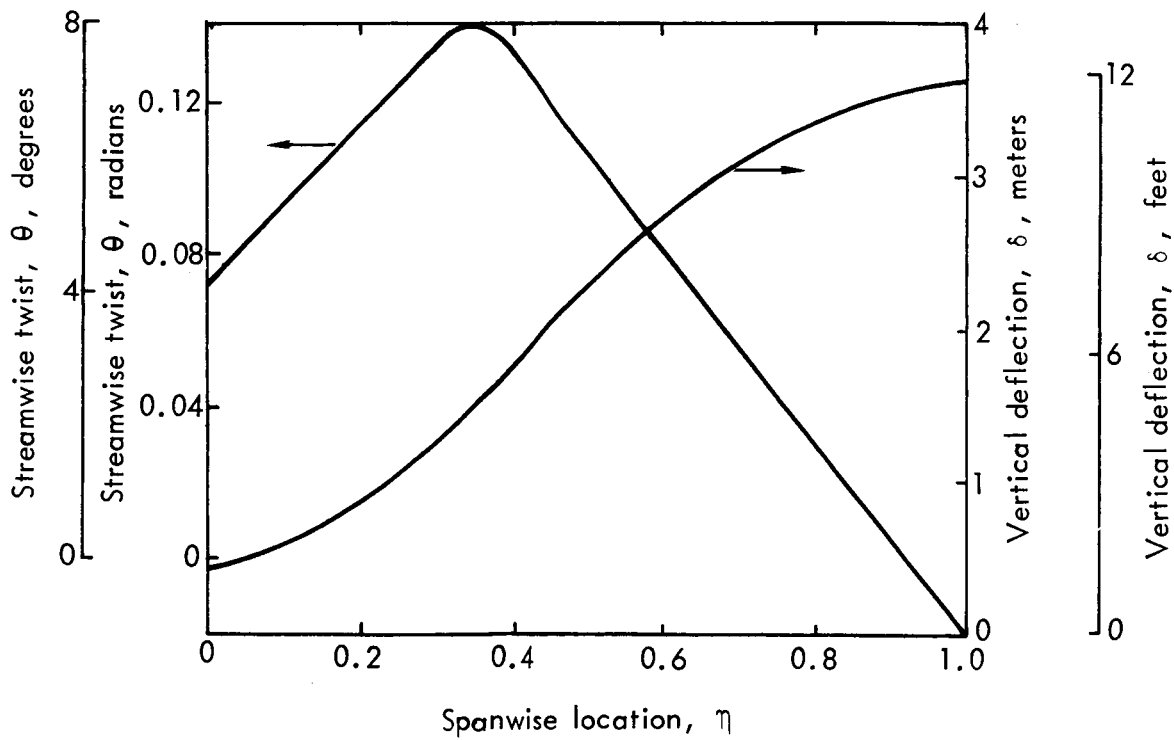


Figure 51. Vertical deflection and streamwise twist for aft wing of Configuration 1

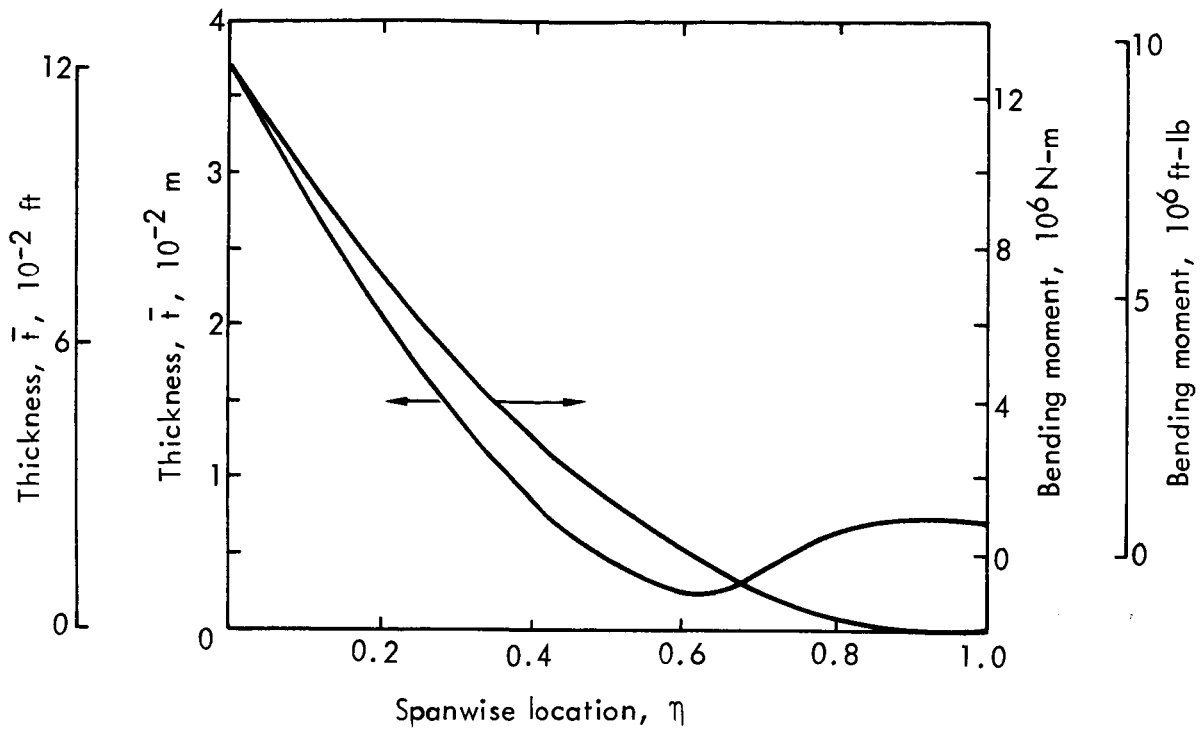


Figure 52. Bending moment and equivalent cover thickness for forward wing of Configuration 1.

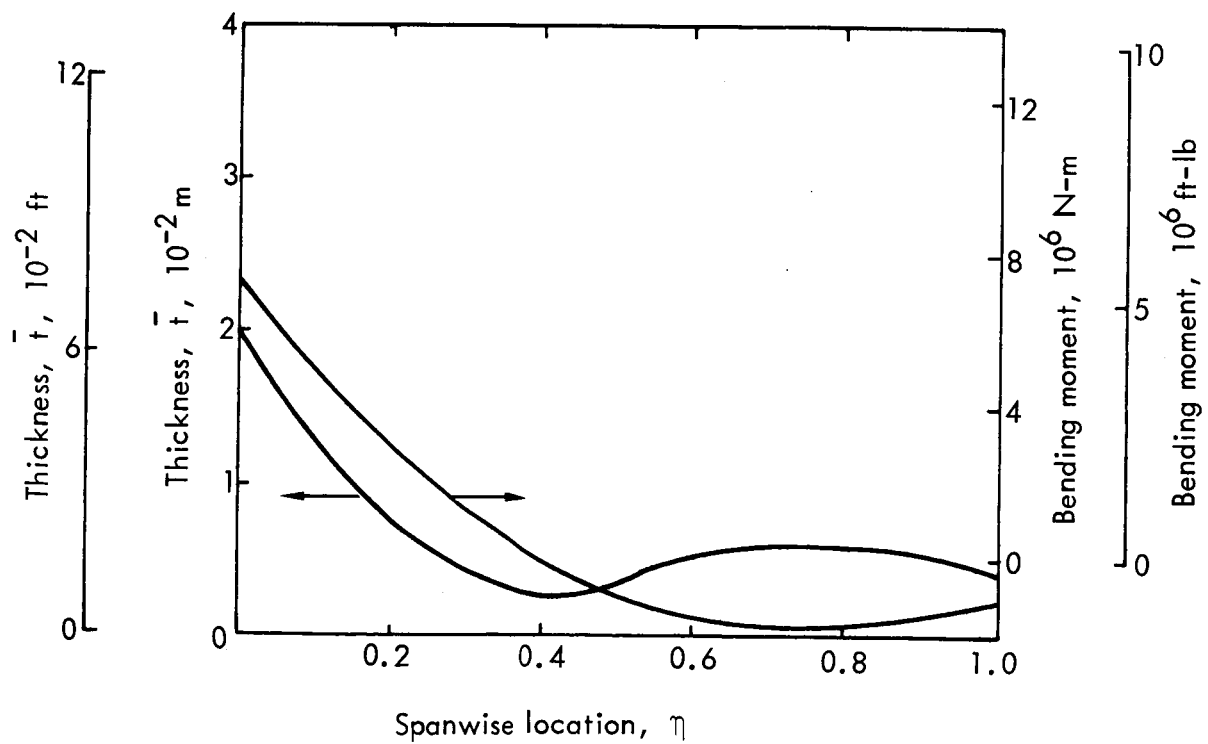


Figure 53. Bending moment and equivalent cover thickness for aft wing of Configuration 1.

TABLE VI. COMPOSITE WEIGHT FACTORS

Weight group	Composite factor
Wings	0.63
Tip fins	0.73
Vertical tail	0.73
Fuselage	0.664
Nacelle	0.787
Landing gear	0.848

Note: The above factors are applied to conventional aluminum structures to account for advanced materials application. (Reference 4.)

quantities with those of data set A indicate good correlation with the FAMAS derived data. The K-factor relations were incorporated into the parametric weight program for analysis of biplane configurations to identify strength-critical structure with no direct stiffness penalty for flutter prevention.

3.3.3.2 Vertical Tail Weight

The vertical tail of the biplane supports the aft wing and transfers loads to the aft fuselage. It was obvious that the vertical tail weight would be governed by fore and aft bending stiffness as well as torsional stiffness. To determine the stiffness effects, the FAMAS program was used to analyze the number 3 and 5 configurations of Figures 44 and 45. These configurations were used since the batted wing configuration was determined to be more structurally efficient than the un-batted wing. Table VIII presents the weights derived from the FAMAS analysis for the vertical tail. Analysis of the parameters affecting vertical tail weight was conducted to derive parametric weight relationships which were subsequently incorporated into the weight estimation routine. These relationships provide close correlation with the FAMAS analysis results giving 5094 kg (11 230 lb) for configuration 5, a difference of 2.8 percent.

TABLE VII. PARAMETRIC WEIGHTS FOR WING AND TIP-FIN CORRELATION

Fixed configuration parameters:

- Forward-wing sweep, 0.70 rad (40 deg)
- Basic wing area, 442.6 m² (4764 ft²)
- Tip-fin height, H_{TF}, 12.71 m (41.70 ft)
- Aft-wing sweep, -0.87 rad (-50 deg)
- Basic wing aspect ratio, 4.12

	Configuration		
	1	2	3
Variable configuration parameters:			
Basic wing taper ratio, TR ₂	1.0	0.4	1.0
Forward wing bat area, m ² (ft ²)	0	0	48.0 (516.67)
Aft wing bat area, m ² (ft ²)	0	0	24.9 (268.02)
Tip fin chord, C _{TF} , m (ft)	5.19 (17.03)	2.96 (9.71)	5.19 (17.03)
A. Weights derived from "FAMAS" analysis, kg (lb)			
Forward wing (K _{comp} = 0.63)	23 858 (52 598)	23 691 (52 230)	20 148 (44 419)
Aft wing (K _{comp} = 0.63)	11 843 (26 109)	12 628 (27 840)	10 056 (22 170)
Tip struts (K _{comp} = 0.73)	8 115 (17 891)	6 677 (14 720)	6 192 (13 651)
	3 900 (8 598)	4 386 (9 670)	3 900 (8 598)
B. Weights derived from initial parametric, kg (lb)			
Forward wing (K _{comp} = 0.63)	36 122 (79 635)	31 326 (69 062)	31 455 (69 346)
Aft wing (K _{comp} = 0.63)	16 614 (36 628)	14 821 (32 675)	14 529 (32 031)
Tip struts (K _{comp} = 0.73)	18 098 (39 899)	15 699 (34 610)	15 516 (34 207)
	1 410 (3 108)	806 (1 777)	1 410 (3 108)
C. Weights derived from modified parametric, kg (lb)			
Forward wing (K _{comp} = 0.63) (K = (1 + TR) ^{-0.48})	23 721 (52 296)	23 844 (52 567)	21 097 (46 511)
Aft wing (K _{comp} = 0.63) (K = 0.437)	11 912 (26 261)	12 611 (27 802)	10 417 (22 966)
Tip struts (K _{comp} = 0.73) (K = 12 x H _{TF} ⁻² C _{TF} ^{1.2})	7 909 (17 437)	6 860 (15 124)	6 780 (14 947)
	3 900 (8 598)	4 373 (9 641)	3 900 (8 598)

TABLE VIII. VERTICAL TAIL WEIGHTS DERIVED FROM FAMAS ANALYSIS

Item	Configuration	
	3	5
Tail area, m ² (ft ²)		
Tail sweep, rad (deg)	-0.52 (-30)	-0.75 (-43)
Thickness-to-chord ratio	0.06	0.10
Aspect ratio	1.09	1.10
Taper ratio	1.0	0.775
Average material thickness:		
o Bending material, cm (in)	0.76 (0.30)	0.93 (0.36)
o Shear material, cm (in)	5.55 (2.19)	3.77 (1.48)
Derived weight data:		
Bending material, kg (lb)	2 971 (6 550)	3 243 (7 150)
Shear material, kg (lb)	1 647 (3 631)	1 792 (3 951)
Ribs, kg (lb)	925 (2 039)	1 007 (2 220)
Secondary structure, kg (lb)	844 (1 861)	744 (1 640)
Total weight (aluminum), kg (lb)	6 387 (14 081)	6 786 (14 961)
Composite factor	0.73	0.73
Vertical weight, kg (lb)	4 663 (10 280)	4 954 (10 922)

3.3.3.3 Fuselage Weight

The biplane configuration weight effects for the fuselage consist of additional fuselage frames for wing attachment (monoplane wing and main landing gear frames are essentially common frames). The fuselage main frames of a monoplane were estimated for the ATT at 2.6 percent of the design landing weight. The biplane weight-estimation logic increases this percentage by 50 percent to 3.9 percent of the landing weight. Additional fuselage weight in the biplane configuration is accounted for by higher wetted area for a given fuselage maximum cross-section and maximum length. The fuselage weight-estimating relationship incorporated into the computer logic, therefore, accounts for increased fuselage main frames and increased fuselage wetted area along with the normal aircraft sizing parameters such as gross weight, load factor, dive speed, landing gear location, length-to-diameter ratio, and belly cargo. For typical biplane and monoplane configurations with constant design parameters, the following increments are presented to illustrate the main frame and wetted area increases from the monoplane weight:

- o Main frames: 8.5 percent increase in total fuselage weight
- o Wetted area: 2.8 percent increase in total fuselage weight

3.3.3.4 Surface-Controls Weight

The biplane surface-controls weight in the parametric weight analysis uses the control surface areas of the forward and aft wings plus an overall 25-percent increase in weight to account for longer runs for hydraulic lines and cables for the control systems. The surface controls weight-estimation relationship is a function of load factor, gross weight, and control surface areas.

3.3.3.5 Other Components Weights

The other component weight relationships are the same for the monoplane (ATT-developed data) and the biplane. The following indicates the logic functions used for each of the other components:

- (a) Landing gear - function of landing weight
- (b) Nacelle and pylon - function of noise level requirements, nacelle wetted area, engine weight and thrust, number of engines, pylon length and sweep, and engine location.
- (c) Propulsion - function of engine weight, number of engines, fuel capacity, and engine location.
- (d) Auxiliary power system - function of gross weight
- (e) Instruments - constant quantity derived for the ATT
- (f) Hydraulics - function of gross weight
- (g) Electrical - function of gross weight
- (h) Avionics - constant quantity derived for the ATT
- (i) Furnishings - function of number of passengers and belly cargo
- (j) Air conditioning and anti-icing - function of cabin design pressure differential, fuselage length and diameter, and gross weight
- (k) Operating equipment - function of number of passengers and belly cargo

3.3.3.6 Weight Summary

The selected interim configuration (configuration type 5) for Phase I was determined using the foregoing parametric weight program as a subroutine within the configuration sizing and performance program. As previously indicated, the wing weight relationships did not provide sufficient stiffness to preclude flutter. For comparison, however, the resulting weight breakdowns from the computer routines are presented in Table IX for the biplane and monoplane (ATT) configurations for the design mission.

TABLE IX. PHASE I WEIGHT SUMMARY COMPARISON

Item	Interim biplane		Monoplane	
	kg	lb	kg	lb
Forward wing	5 924	13 060	21 901	48 284
Aft wing	6 155	13 570	-	-
Tip fins	4 097	9 033	-	-
Horizontal tail	-	-	1 862	4 105
Vertical tail	6 386	14 079	1 457	3 212
Fuselage	26 748	58 970	24 551	54 125
Landing gear	11 898	26 231	11 927	26 295
Nacelle/pylons	9 358	20 631	9 468	20 874
Propulsion system	17 811	39 266	18 065	39 827
Auxiliary power system	638	1 406	639	1 409
Surface controls	4 620	10 186	3 963	8 737
Instruments	602	1 327	602	1 327
Hydraulics & pneumatics	1 672	3 686	1 676	3 695
Electrical	2 545	5 611	2 547	5 616
Avionics	918	2 024	918	2 024
Furnishings	12 393	27 321	12 393	27 321
Air conditioning and press. system	3 067	6 762	3 250	7 165
Weight empty	114 832	253 163	115 219	254 016
Operating equipment	12 804	28 229	12 864	28 361
Passenger payload	38 465	84 800	38 465	84 800
Cargo payload	0	0	0	0
Zero fuel weight	166 101	366 192	166 548	367 177
Mission fuel	135 490	298 704	135 737	299 248
Ramp gross weight	301 591	664 896	302 285	666 425

Note: Above weight values reflect the use of filamentary composites using the weight factors identified in Table VI.

The parametric weight data for the interim biplane configuration are intended to reflect strength-designed structure as far as the wings and tip fins are concerned, and assume that aeroelastic problems are handled by active control devices. It is emphasized that the parametric weight relations were derived using three base-point configurations and their corresponding redundant FAMAS analyses, which is a limited data correlation family for this redundant structural configuration. The interim configuration wing parametric weights appear to be low when compared to other strength-designed configurations derived by FAMAS. Since flutter problems with this configuration were predominant, further excursion into the exact correlation of parametric weights and redundant FAMAS analysis weights was not of major concern. That is, higher wing masses would have yielded lower flutter speeds, and since the flutter speed was already much too low, a change in configuration was deemed to be the most likely avenue of investigation. This changed configuration is illustrated by configuration No. 6 in Figure 45 and is presented in the Phase II section of this report.

3.3.4 FLUTTER ANALYSIS

The primary objectives of the flutter investigation were to:

- o Determine whether serious flutter problems exist which render the transonic biplane transport concept impracticable.
- o Determine approximate stiffness or other significant flutter prevention weight increments for incorporation into a transonic biplane parametric weight equation.

In order to achieve these objectives, flutter analyses were conducted for four different biplane configurations. The methods of analysis are described below.

3.3.4.1 Math Model for Flutter Analysis

The redundant load paths associated with the box-wing system necessitated the use of a finite-element redundant-analysis program to calculate the flexibility influence coefficients used in the flutter analysis. Therefore, a common mathematical model was used for both the strength and influence coefficient calculations. A typical redundant-analysis model was shown previously in Figure 47. These models represented the complete configuration and typically contained over 400 degrees of freedom, which is considerably more than could be practically dealt with in a dynamic analysis. In order to reduce the degrees of freedom to a manageable number, the model was restrained at a node near the aircraft center of gravity and influence coefficients were calculated for symmetric and antisymmetric cases. Only those degrees of freedom required to represent the important inertial and aerodynamic forces on one side of the plane of symmetry were retained for the dynamic analyses.

A typical dynamic analysis math model is depicted in Figure 54. Although the right side of the configuration is shown for clarity, only the left side was actually represented. Each lifting-surface panel was represented inertially by a lumped mass

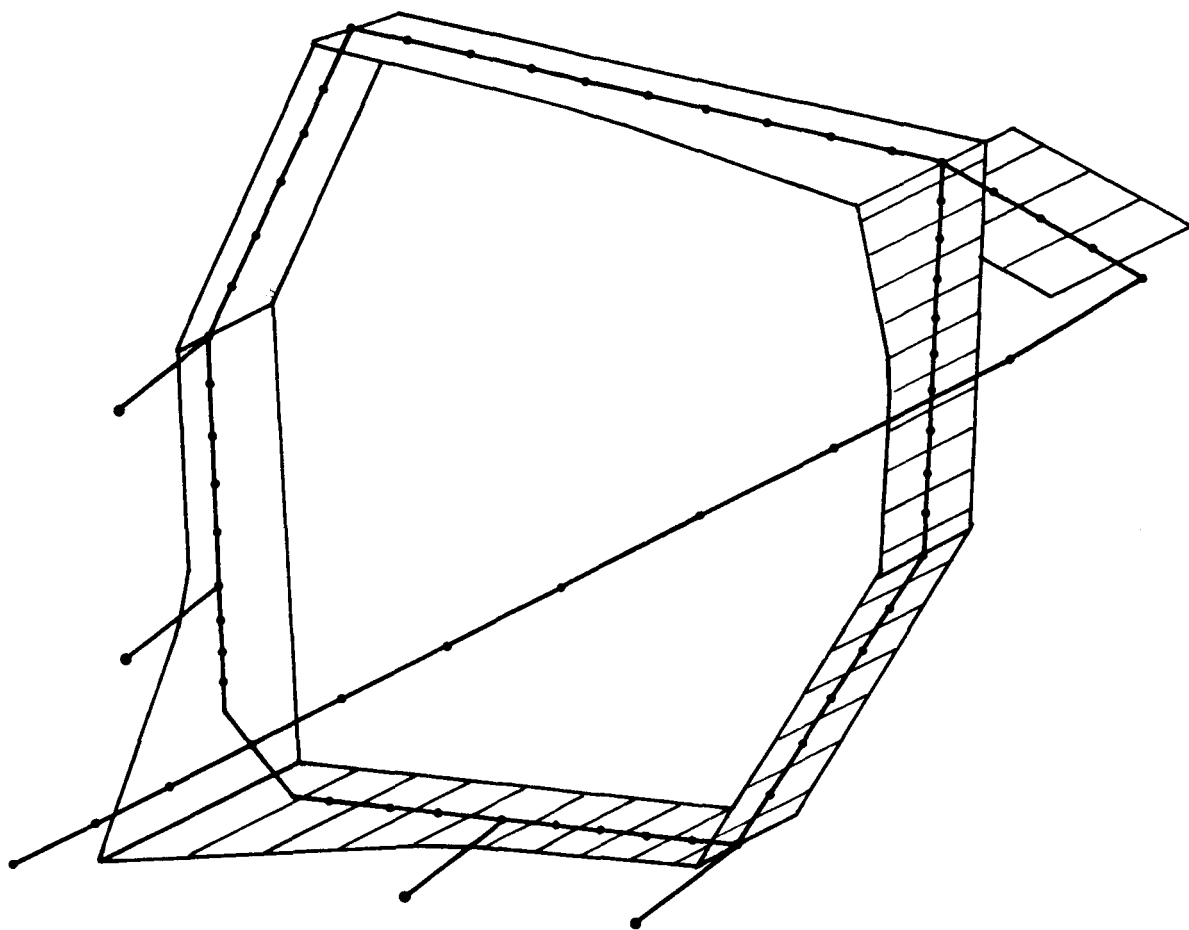


Figure 54. Typical math model used for vibration and flutter analysis.

and a pitching moment of inertia. Each fuselage panel was represented inertially by a lumped mass and a roll moment of inertia. Each engine-nacelle was represented by a lumped mass and roll, pitch, and yaw moments of inertia. The symmetric analysis model included a total of 128 degrees of freedom and the antisymmetric included 138. The first 20 vibration modes were calculated for the restrained models and these were coupled with the appropriate three rigid-body modes to represent the symmetric and antisymmetric flutter motions. The unsteady aerodynamic forces associated with the flutter motions were usually represented by Theodorsen strip-theory coefficients modified to yield the same spanwise lift and moment distributions as were calculated by steady non-planar lifting-surface (vortex lattice) theory for Mach 0.95. Some analyses of the interim configuration were also conducted with aerodynamic coefficients calculated by unsteady non-planar lifting-surface (doublet lattice) methods. The forward wing, tip fin, aft wing, and vertical stabilizer system were represented by a total of 96 doublet lattice panels. Thus, the unsteady induced flow effects between all of these lifting surfaces were included. Aerodynamic forces on the nacelle-pylons and fuselage were neglected.

3.3.4.2 Results for Initial Study Configuration (Configuration 1)

Vibration and flutter analyses of the strength-designed, initial study configuration were conducted for the maximum payload, empty fuel condition. Because of tip strut coupling and the opposing sweep effects of the two wings, a relatively high flutter speed for the biplane configuration was anticipated. This did not prove to be true, however. Both symmetric and antisymmetric instabilities occurred at speeds well below the required flutter speed of 270 m/sec (525 KCAS).

The critical antisymmetric instability occurred at a speed of 144 m/sec (279 KEAS) and a frequency of 0.83 Hz. Although the flutter modes were not calculated for this configuration, the low flutter frequency indicated that one or more of the fundamental antisymmetric vibration modes was probably a major contributor to the flutter motion. This indication was supported by the fact that the flutter speed was found to be approximately proportional to the frequency of the second (0.724 Hz) antisymmetric vibration mode (see Table X). This mode is characterized by forward-

TABLE X. ANTISYMMETRIC VIBRATION MODES USED IN FLUTTER ANALYSES.

Mode Number	Natural frequencies (Hz) for configuration number			Predominant motion configuration 5
	1	4	5	
1	0.345	0.419	0.423	Wings vertical bending
2	0.724	0.917	0.823	Lower wing fore and aft, upper wing yaw-roll
3	0.997	1.413	1.179	Upper wing yaw (fin torsion)
4	1.286	1.741	1.538	Lower wing (midspan) torsion
5	1.495	1.781	1.717	
6	2.003	1.898	1.834	
7	2.123	2.428	2.195	
8	2.364	3.041	2.906	
9	2.592	3.211	3.013	
10	3.004	3.596	3.566	
11	3.079	4.280	3.728	
12	4.500	5.005	4.240	
13	4.681	5.527	5.194	
14	5.347	6.280	6.143	
15	5.571	7.524	6.405	
16	5.977	8.059	8.032	
17	7.193	8.862	8.526	
18	8.088	9.299	8.867	
19	8.387	11.088	9.799	
20	9.507	11.353	11.305	

wing fore-and-aft bending which is out-of-phase with aft-wing yawing and rolling motion. These results indicated that a general stiffness increase of approximately 250 percent was required on the forward wing and vertical stabilizer and perhaps on the aft wing and tip fins in order to raise the flutter speed to an acceptable level.

The critical symmetric instability occurred at a speed of 163 m/sec (316 KEAS) and a frequency of 0.48 Hz. The low flutter frequency indicated that the instability was very fundamental in nature and that one or more of the fundamental symmetric vibration modes (Table XI) was a likely contributor to the flutter motion. Subsequent investigations indicated that this instability involved large amounts of fuselage pitching and plunging and aft-wing vertical-bending motion. These results again indicated that a very large general stiffness increase (approximately 176%) would be required for adequate flutter stability.

In view of the foregoing results, it became clear that prohibitively large weight increases would result from attempts to achieve satisfactory flutter speeds through general stiffening of the primary structure. Therefore, an attempt was made to

TABLE XI. SYMMETRIC VIBRATION MODES USED IN FLUTTER ANALYSES.

Mode Number	Natural frequencies (Hz) for configuration number			Predominant motion configuration 5
	1	4	5	
1	0.481	0.557	0.575	Wings vertical bending
2	1.013	1.394	1.135	Upper wing vertical, lower wing fore and aft bending
3	1.245	1.678	1.547	Lower wing (midspan) torsion
4	1.507	1.871	1.949	Upper wing fore and aft, vertical bending
5	1.816	2.348	2.055	Inbd engine pylon lateral bending
6	2.063	2.507	2.409	Upper wing and fin fore and aft, aft fuselage vertical bending
7	2.299	2.929	2.916	
8	2.437	3.113	2.967	
9	2.996	3.824	3.798	
10	3.127	4.646	4.311	
11	3.605	5.105	4.588	
12	4.735	5.430	5.267	
13	5.373	6.505	5.888	
14	5.467	6.986	6.593	
15	6.526	8.771	6.857	
16	7.004	9.924	9.488	
17	7.637	11.430	10.680	
18	8.838	11.890	12.030	
19	9.879	13.350	12.810	
20	10.850	14.610	13.080	

achieve the required flutter speed increase by reconfiguring the vehicle. Since the antisymmetric flutter instability involved large amounts of fore-and-aft motion of the aft-wing tips relative to the forward-wing tips, it appeared that a 50-percent reduction in the tip-fin length would produce a substantial increase in the effective stiffness and thereby increase the critical speed of this mode.

Reduced tip fins, along with wing bats and revised wing sweeps, were incorporated into Configuration 4. These changes were all estimated to be beneficial from a flutter standpoint. The antisymmetric and symmetric flutter speeds for this configuration were 179 m/sec (348 KEAS) at 1.53 Hz and 190 m/sec (370 KEAS) at 0.76 Hz, respectively. Thus, the critical flutter speed increased by 25 percent, but it remained far short of the required 270 m/sec (525 KCAS). Also, aerodynamic studies of this configuration indicated that the reduced wing-tip separation caused a severe drag penalty. As a result, the configuration was dropped from further consideration.

3.3.4.3 Results for Configuration 5

Because no practical passive solution to the flutter problem had been found, an active flutter suppression system was assumed to provide the required flutter speed increase, and the configuration was sized on the basis of aerodynamic performance and strength considerations. This led to Configuration 5 in Figure 45 which was similar to Configuration 4 except that the tip fin was restored to the original 0.3 semispan length.

Flutter analyses were conducted for Configuration 5 using modified strip-theory aerodynamic coefficients as before. The flutter speeds and frequencies for the antisymmetric and symmetric cases were 148 m/sec (287 KEAS) at 1.15 Hz and 155 m/sec (302 KEAS) at 0.62 Hz, respectively. Thus, the flutter speeds had returned to approximately the same levels as were predicted for the initial study configuration, in spite of significantly greater inboard wing stiffnesses produced by the wing bats.

Because it was suspected that the strip-theory analysis results might be overly conservative, flutter analyses of this configuration were also performed with unsteady lifting-surface-theory aerodynamic coefficients. The results of these analyses are shown in Figures 55 through 58. The critical antisymmetric mode is shown in Figure 55 to progress from a 1.28 Hz vibration mode at zero airspeed to an unstable 1.14 Hz flutter mode at 133 m/sec (259 KEAS). The structural damping coefficient required for neutral stability continues to increase rapidly at airspeeds above the flutter speed, which indicates a decisive, rather than marginal, instability. In order to better understand the nature of this instability, the complex flutter motions at the speed of instability were calculated. These are shown in Figure 56 as relative magnitudes and phase angles at several points on a stick diagram of the vehicle. The predominant motion is seen to be yawing, rolling, and lateral translation of the aft wing associated with lateral bending and torsion of the vertical stabilizer. This was similar to antisymmetric T-tail flutter motion and suggested that a stiffer connection between the massive aft wing and the fuselage would be very beneficial in increasing the antisymmetric flutter speed.

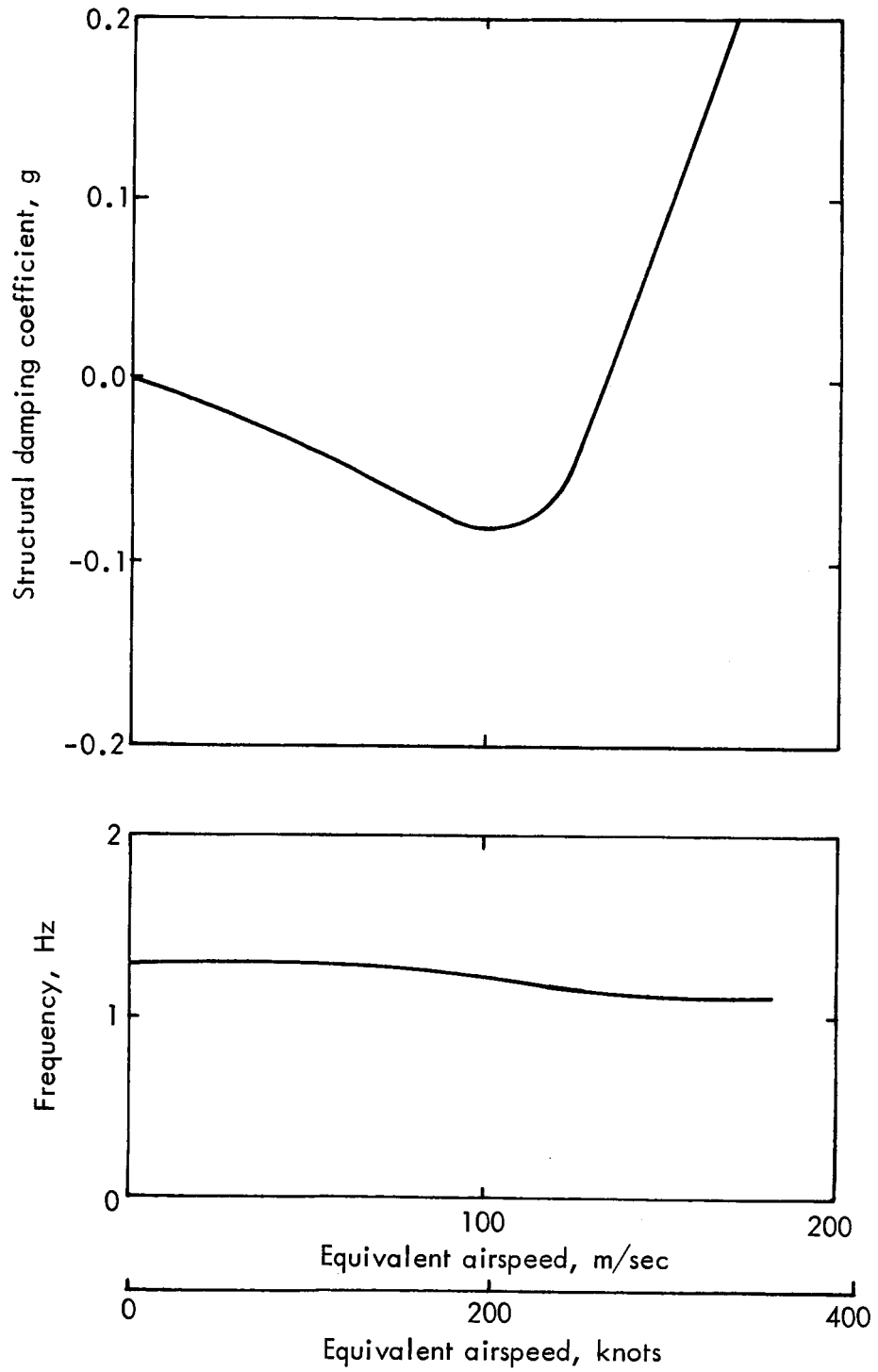


Figure 55. Antisymmetric flutter analysis results for configuration 5, doublet lattice aerodynamics.

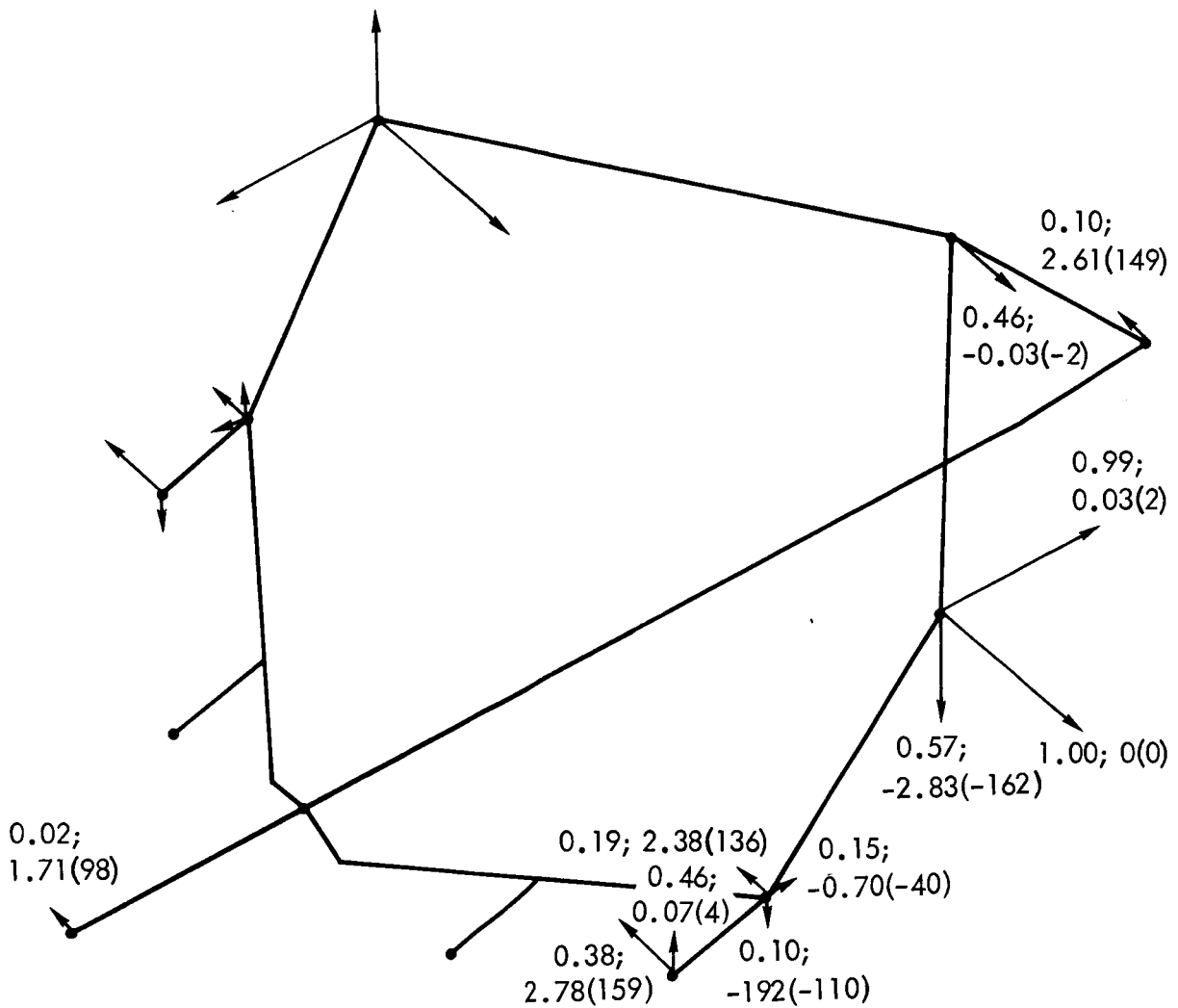


Figure 56. Critical antisymmetric flutter mode for configuration 5, doublet lattice aerodynamics. Values with vectors are relative flutter amplitude and phase angle in radians (degrees).

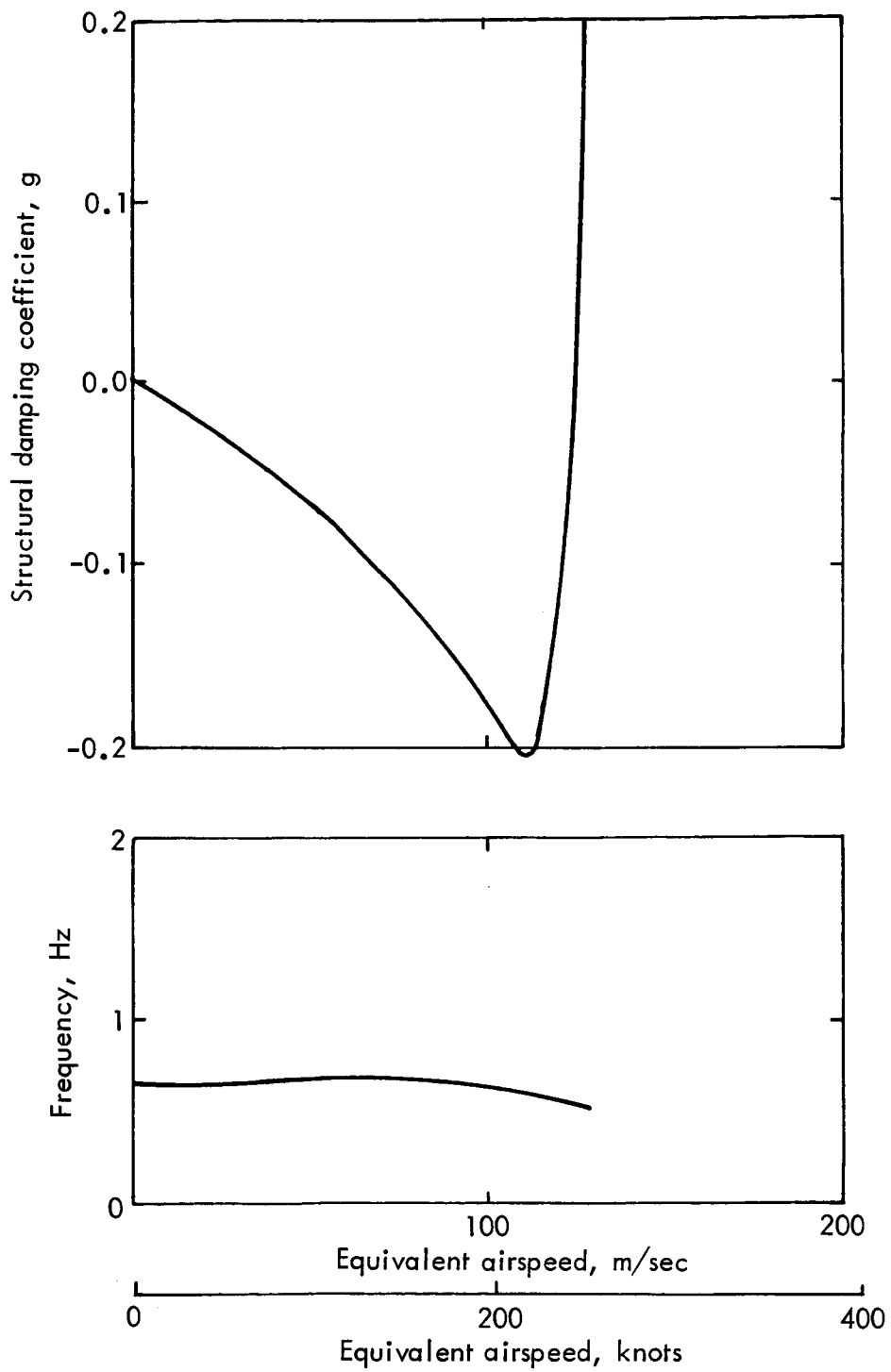


Figure 57. Symmetric flutter analysis results for configuration 5, doublet lattice aerodynamics.

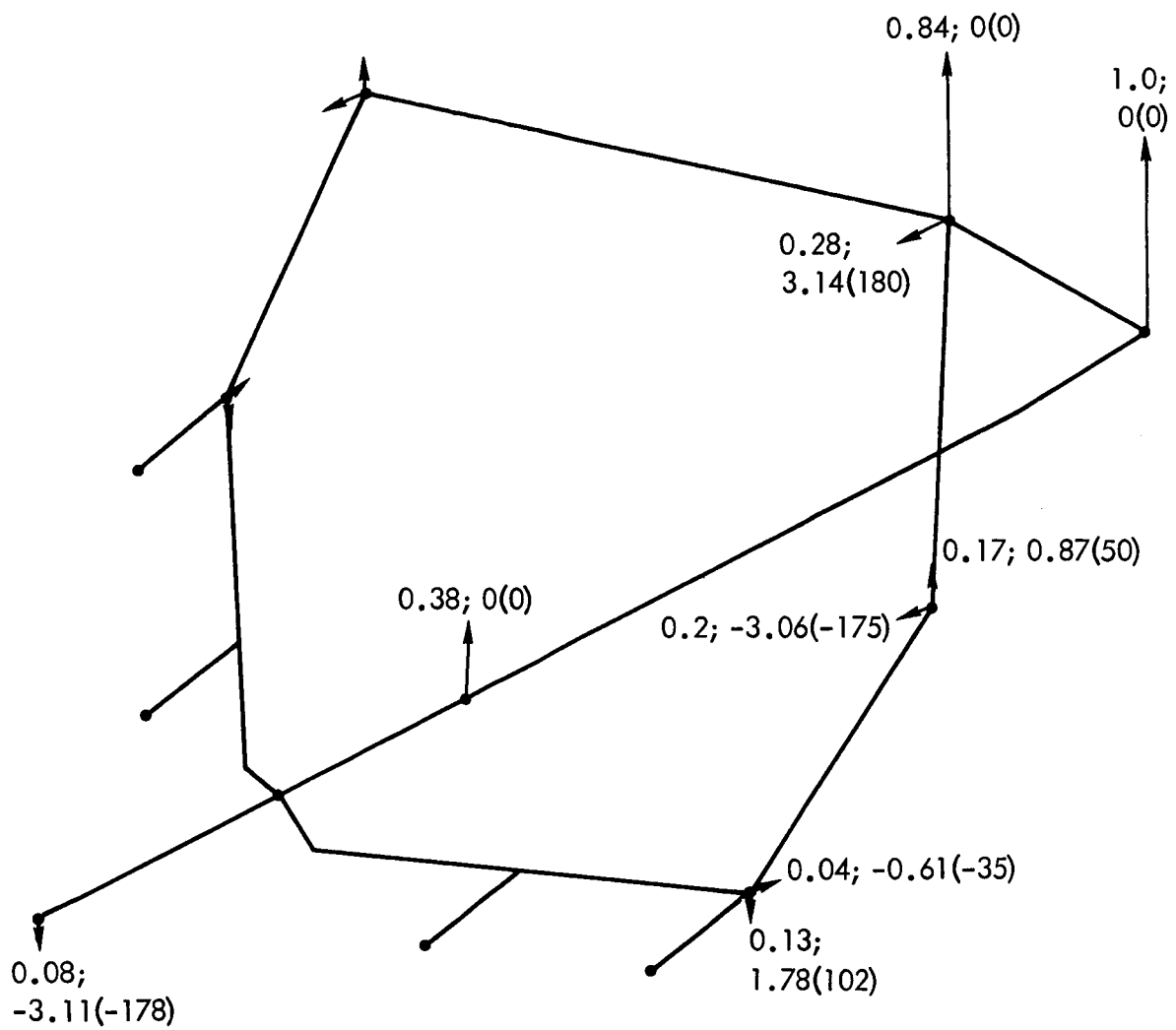


Figure 58. Critical symmetric flutter mode for configuration 5, doublet lattice aerodynamics. Values with vectors are relative flutter amplitude and phase angle in radians (degrees).

The stiffness of this connection on the Phase I configurations was limited by the vertical stabilizer, which was relatively flexible in lateral bending and torsion. This was an important consideration in the configuration selections during Phase II.

Figure 57 shows the frequency and damping variations with airspeed for the critical symmetric flutter mode. The curves show the critical 0.52 Hz mode to be decidedly unstable at speeds above 124 m/sec (241 KEAS) with an attendant downward trend in frequency. Figure 58 shows the critical symmetric flutter mode at the speed of instability. This mode consists mainly of fuselage pitching about a point near its nose, with out-of-phase bending of the wings (particularly the aft wing) and vertical stabilizer such that relatively little motion occurs at the wing tips. This unusual mode of instability resembles a highly modified, flexible, short-period mode and is apparently peculiar to the biplane configuration. Because of its very low frequency, it could probably be effectively stabilized by an active control system.

The stiffness and weight data used in the flutter analyses of Configuration 5 actually reflected a level of strength in excess of that required by the design load condition. Because of the unsatisfactorily low flutter speeds, however, no further refinement of the structural design was made for this configuration. Instead, Phase II of the study was redirected towards finding a passive solution to the flutter problems by more substantial reconfiguration of the vehicle.

4.0 CONFIGURATION STUDIES

4.1 SIZING AND PERFORMANCE PROGRAM

It must be recognized at an early stage in configuration development that an optimum aerodynamic configuration does not necessarily give a minimum weight aircraft since allowances must be made for the interaction of other disciplines such as structures and propulsion. For this reason, a parametric computer program was used to determine sensitivity of the various design constraints on a configuration design for a 10 186 km (5500 n.m.) mission at a cruise Mach number of 0.95. Based on results of the analyses discussed in section 3, a configuration of the type identified as number 5 in figure 45 was assumed, and the following characteristics were used to define all cases considered in this analysis.

- o Forward-wing sweep = 0.79 rad (45°)
- o Aft-wing sweep = -0.54 rad (-30°)
- o Wing separation distance to span ratio, $h/b = 0.3$
- o ATT composite utilization
- o STF-429 engine technology
- o Supercritical aerodynamics
- o Fuselage sized to 400 passengers
- o Cruise altitude = 11 278 m (37 000 ft)

The configuration variables evaluated were aspect ratio, cruise lift coefficient (or wing loading) and small variations in wing sweep.

4.2 PARAMETRIC STUDY RESULTS

Early studies on the effect of varying fore and aft-wing sweep by small amounts indicated penalties in ramp weight. Therefore, the emphasis was concentrated on optimizing the basic sweep case for aspect ratio and cruise lift coefficient.

In order to make a rapid assessment of the takeoff performance of the various candidate configurations, use was made of the empirical relationship between FAA takeoff distance over 10.67 m (35 ft) and the parameters W/S , W/T , $C_{L_{1.2V_S}}$ and σ . Figure 59 presents takeoff field lengths for a $306^{\circ}K$ ($90^{\circ}F$) day at a 304.8 m (1000 ft) airport altitude. Studies of the maximum lift capability in

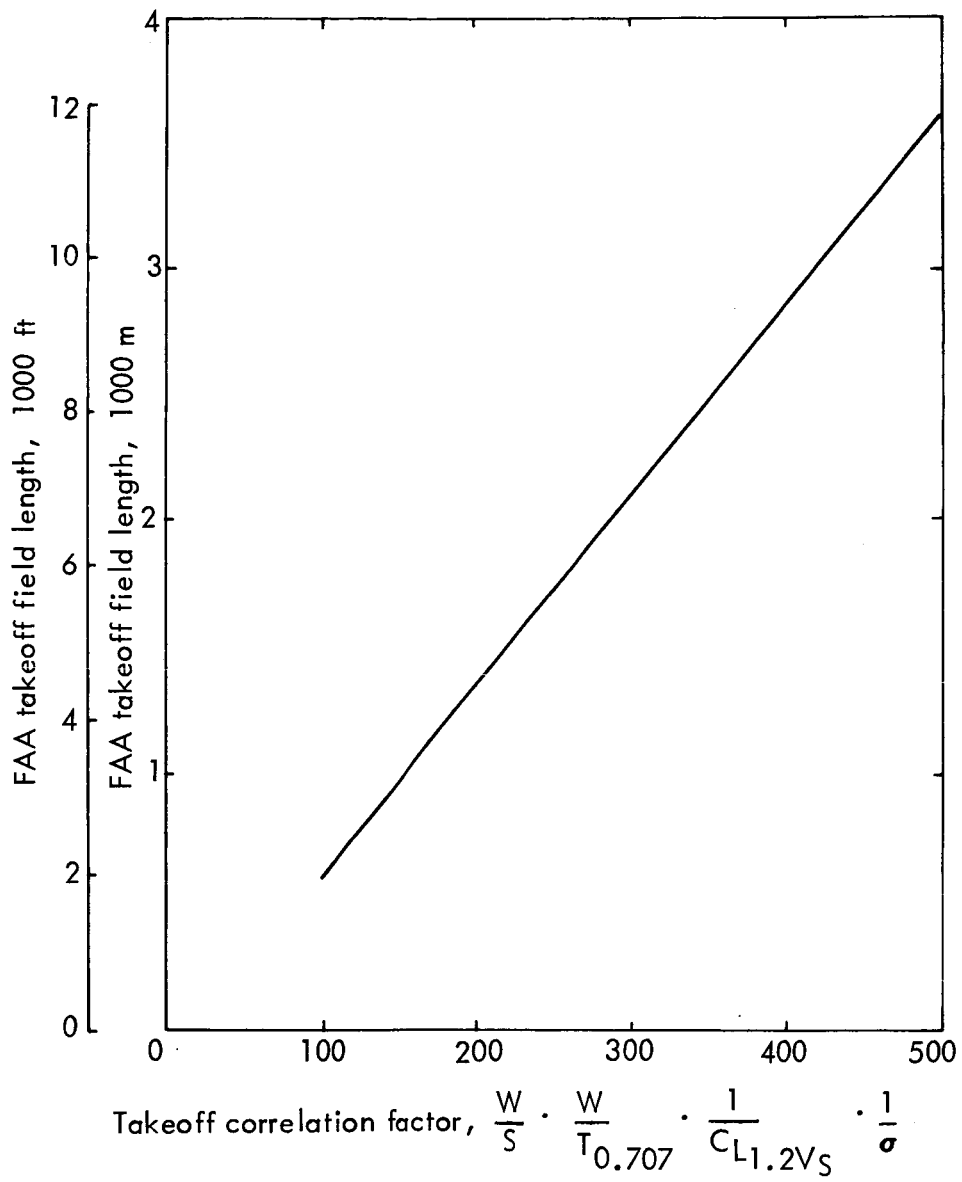


Figure 59. Takeoff field length correlation.

Section 3.1.2 indicated that the biplane configuration was capable of achieving maximum lift coefficient levels comparable to those on the ATT monoplane configuration. Consequently, it was assumed that cruise wing loadings could be chosen within a range comparable to those of the ATT, and that no reduction in wing loading would be required to meet airfield performance objectives.

Figure 60 presents calculated variations in ramp weight with aspect ratio and initial cruise lift coefficient. Superimposed on this plot is a locus of configurations, as determined from Figure 61, which satisfy a takeoff-field requirement of 3048 m (10 000 ft). This provides a cut-off for desired wing loadings of configurations satisfying all mission requirements.

Similarly, Figure 62 gives mission fuel requirements with the 3048 m (10 000 ft) takeoff requirement shown. These data indicate that a configuration having an aspect ratio of 4.4 and a cruise lift coefficient of 0.464 appears to be near optimum. This was defined as the interim selected configuration (See Figure 36).

Since the preliminary optimization process described does not represent levels of weight and aerodynamic efficiency which have been substantiated during an actual design phase, some basic sensitivity studies were also made to determine effects on ramp weight of variations of vertical tail weight, zero-lift drag coefficient, and wing span efficiency factor. Figure 63 presents incremental ramp weight data derived from the sizing program for independent variations in these parameters. These data indicate that changes in vertical tail weight per unit of surface area produce a ramp weight change of 9525 kg (21 000 lb) on a configuration sized to meet the 10 186 km (5500 n.m.) mission. Small increments in zero-lift drag also have considerable effect on ramp weight. An increment of 10 counts ($\Delta C_{D0} = 0.0010$) produces a 15 876 kg (35 000 lb) gross weight penalty. Sensitivity to small changes in span efficiency factor is also significant, as Figure 63 shows. A decrement of 0.1 in span efficiency or a 6-count increase in induced drag produce a 6-count increase in induced drag produces a 4536 kg (10 000 lb) penalty in ramp weight.

Characteristics of the interim configuration selected from the parametric results just discussed are summarized below:

Takeoff weight	301 592 kg (664 897 lb)
Passenger payload	38 465 kg (84 800 lb)
Range	10 186 km (5500 n. mi.)
Takeoff distance	3048 m (10 000 ft)

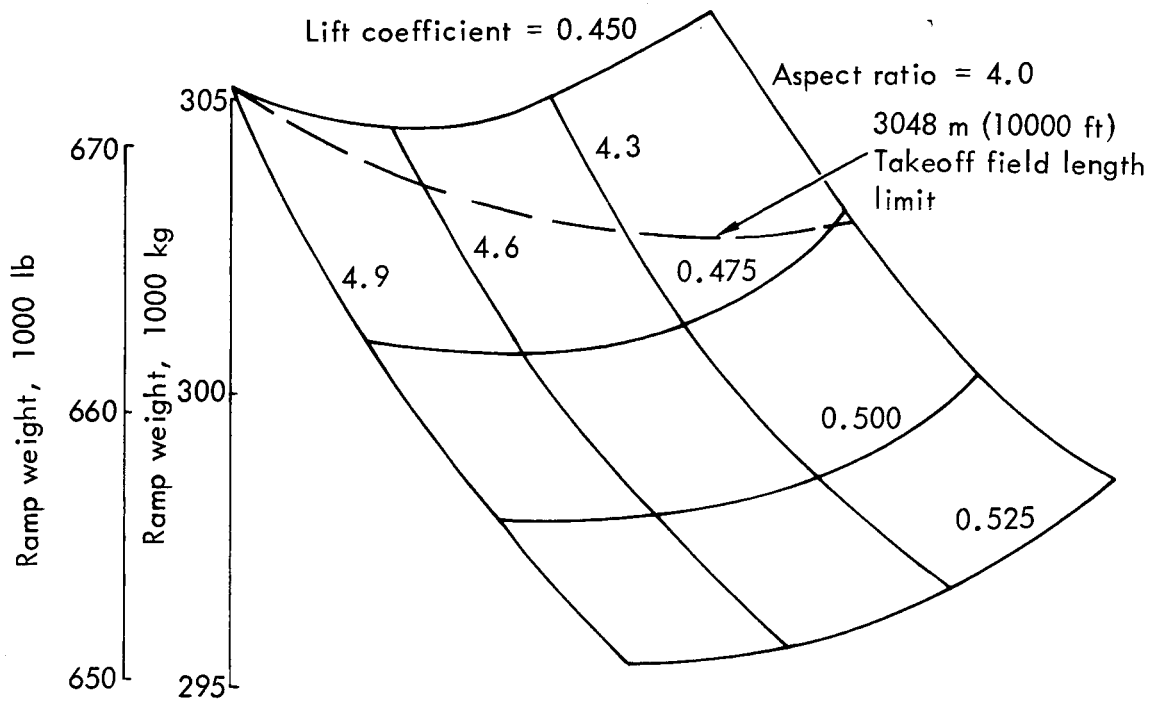


Figure 60. Variation of ramp weight with aspect ratio and initial cruise lift coefficient.

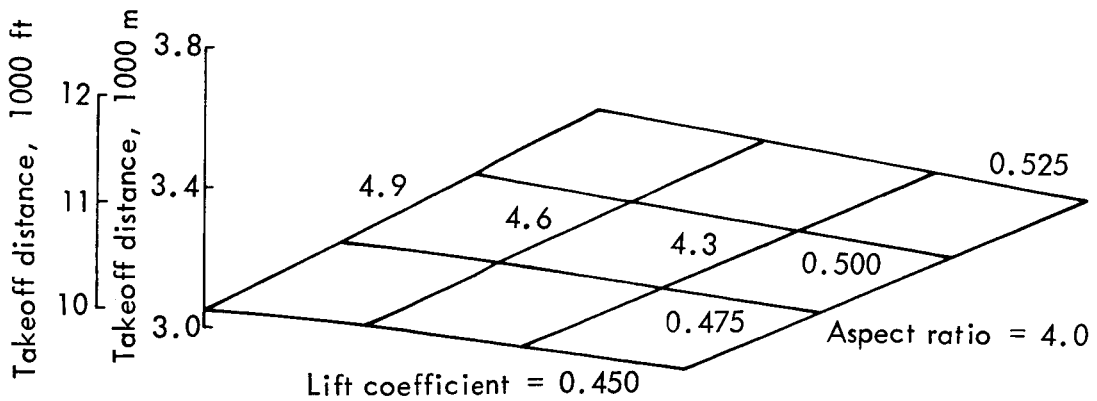


Figure 61. Takeoff field length.

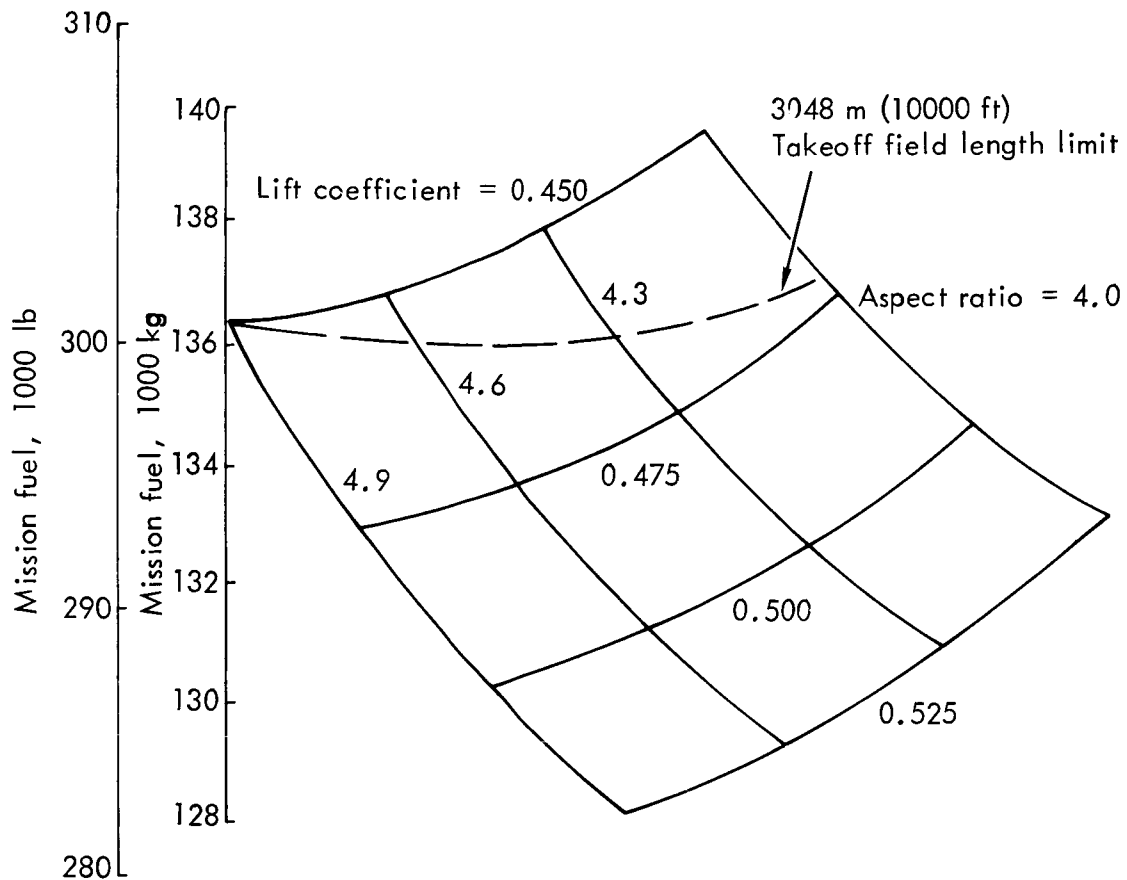


Figure 62. Mission fuel requirements.

These data show that the weight and fuel required for a biplane, which will satisfy the specified payload-range performance, are approximately equal to those of the monoplane configuration that was developed during a detailed design and optimization effort on the NASA/Lockheed ATT study (Reference 4). It could be anticipated that further development effort would provide worthwhile improvements by optimizing aerodynamic and structural characteristics of the biplane. Since the frequencies of vibrations involved in the flutter instabilities discussed in Section 3.3.4 are very low, an alleviation system could probably be developed to satisfy normal flutter-speed margins. A more conclusive case for further development of this concept could be made, however, if marginal performance benefits were not combined with a requirement for a new and rather complex active control system. Phase II of this study was, therefore, devoted to a search for configuration changes which might alleviate flutter instabilities by passive means.

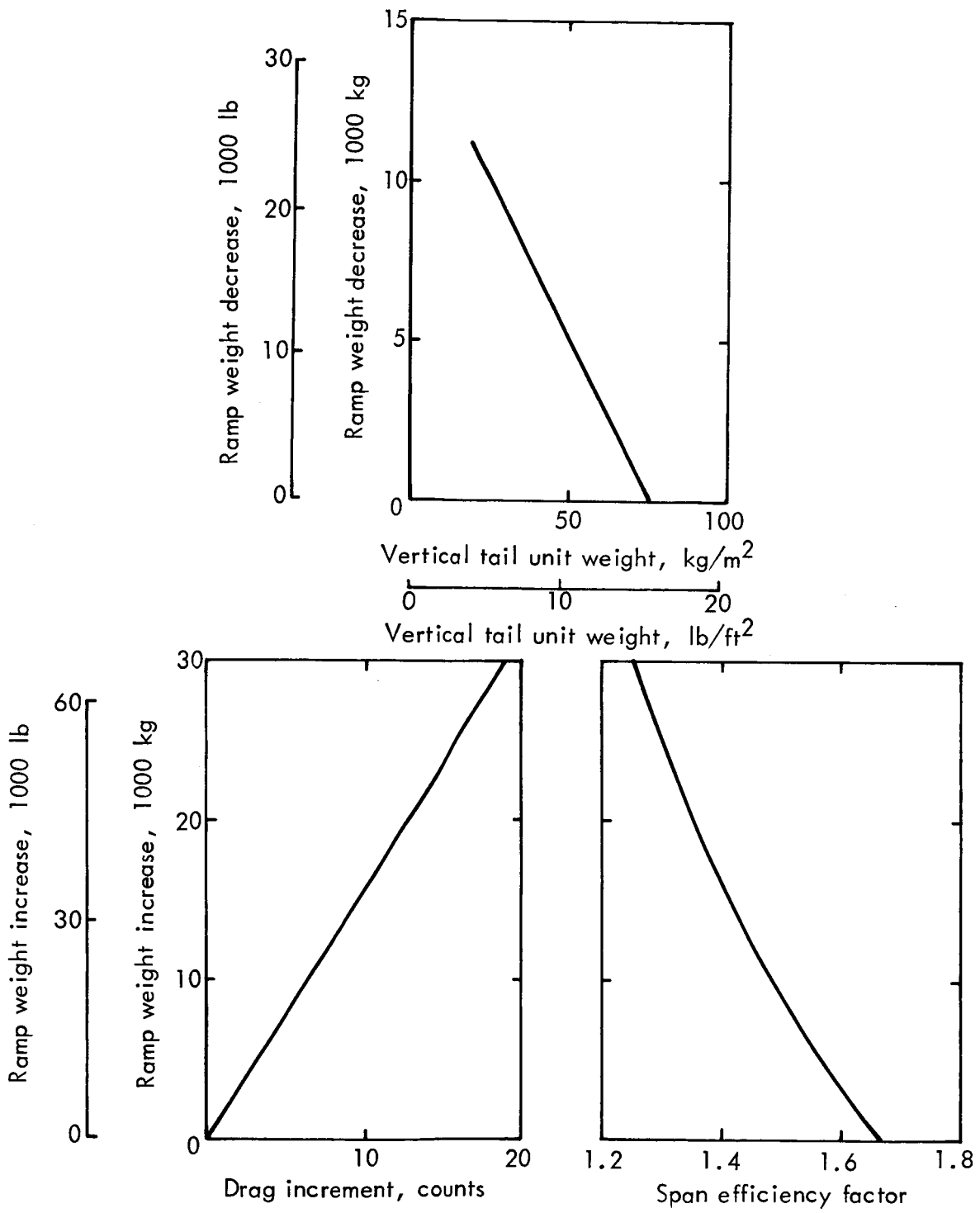


Figure 63. Sensitivity study results.

PHASE II. REVISED STUDY PROGRAM

1.0 REDEFINED STUDY PLAN

Results of studies conducted to this point can be summarized by two basic statements:

- o Initial transonic biplane configurations are roughly equivalent to refined monoplane configurations in terms of ramp weights required to achieve a given level of performance.
- o Flutter instabilities occur at speeds well below those required for transport aircraft cruising at a Mach number of 0.95.

The equivalence of monoplane and biplane weights and performance, in spite of significantly improved aerodynamic span efficiency factors for the biplane, is the result of substantial increases in vertical tail and fuselage structural weights. It could be expected that more intensive development work on this configuration concept could reduce these weight penalties and therefore show some benefits for the transonic biplane. In order to exploit such potential benefits, however, it is first necessary to eliminate the flutter susceptibility or to supply a satisfactory suppression system. As might be expected for a configuration having the many aeroelastic degrees of freedom possible in the biplane arrangement, the flutter motions are extremely complex, and no single feature of the arrangement was isolated as the source of these instabilities. It can be argued that the rather low frequencies (less than 2 Hz) shown by the flutter results would make the biplane configuration especially amenable to flutter alleviation through use of active control systems. While this is probably a valid argument, and a satisfactory biplane configuration could probably be evolved based on active control technology concepts, the development of such a flutter suppression system is outside the scope of the present investigation.

After a review of the study results at this point, and of the various options available for establishing the feasibility of the transonic biplane concept, it became apparent that studies directed toward a better understanding of the flutter instability phenomena, and of potential passive flutter elimination would be most profitable.

2.0 ALTERNATE CONFIGURATION

Several avenues of potential improvement in flutter characteristics were examined in establishing configurations for Phase II of this study. Because of the complex, redundant structural configuration and the meager amount of information available regarding the underlying phenomena, no direct attack on the flutter instability was possible. Relocation of large discrete masses (engines) offered one possibility. Elimination of flexibilities introduced by transmitting aft-wing loads into the fuselage through the vertical tail also appeared to be a likely candidate. Each potential flutter improvement scheme was also investigated to assure no significant deterioration in induced drag. Studies conducted in an attempt to develop a satisfactory alternate configuration are discussed in this section.

2.1 FLUTTER CONSIDERATIONS

Relocation of the engines from the forward wing to some point on the fuselage was a possible solution to the flutter problem which had not been investigated during Phase I. Therefore, a brief engine relocation study was conducted on Configuration 5 using modified strip-theory aerodynamic coefficients. Alternately, the outboard, inboard, and both inboard and outboard engines were relocated to an aft fuselage location just forward of the vertical stabilizer. The results are summarized below.

<u>Engines Relocated to Aft Fuselage</u>	<u>Antisymmetric</u>		<u>Symmetric</u>		
	<u>Speed, m/s (KEAS)</u>	<u>Freq, Hz</u>	<u>Speed, m/s (KEAS)</u>	<u>Freq, Hz</u>	
None (Configuration 5)	148	(287)	155	(302)	0.62
Outboard	155	(301)	167	(324)	0.62
Inboard	137	(266)	162	(314)	0.58
Outboard & Inboard	136	(264)	172	(334)	0.57

These results indicate that a small (5%) increase in the critical flutter speed could be obtained by relocating the outboard engines to the aft fuselage. The other relocations reduced the critical flutter speed. Consequently, no engine relocations were included because of the small flutter speed benefit and the increased difficulty of obtaining a smooth area distribution for minimum wave drag.

The results of the Phase I studies indicated that a stiffer connection between the aft wing and the fuselage would likely produce a significant increase in the antisymmetric flutter speed. Therefore, the Phase II studies were directed toward configurations in which the aft wing was connected directly to the aft fuselage, rather than through a vertical stabilizer. This was also expected to yield a beneficial effect on the symmetric flutter speed through elimination of the vertical stabilizer fore-and-aft bending flexibility. Thus, a series of such configurations was developed and analyzed for induced cruise drag, as is discussed in the next section.

2.2 AERODYNAMIC CONFIGURATION

2.2.1 INDUCED DRAG ANALYSIS - ALTERNATE CONFIGURATION SELECTION

As a result of the flutter analysis described in Section 3.3.4 of Phase I and the subsequent review of potential alternative configurations outlined in Section 2.1 of Phase II, it was decided to continue investigation of configurations which might provide improved flutter characteristics while maintaining the favorable induced drag features of this concept.

Figure 64 presents a comparison of span efficiency factor for a series of closed-biplane arrangements. Configuration A serves as the datum and is representative of the rectangular box arrangement for the interim configuration studied in Phase I. One approach to possible improvement in the flutter characteristics was through deletion of the load-carrying vertical tail and its severe weight penalty by relocating the aft wing on the fuselage, as indicated in Section 2.1. For configurations B and C, the inner portion of the aft wing is fixed to the fuselage and the outer portion remains horizontal in order to maintain a high value of span efficiency. Configurations D through G show the aft wing as a straight panel with varying degrees of dihedral. It is evident that maintaining some of the rectangular box features at the wing tip is desirable in order to minimize the intensity of the tip trailing vortex and the induced drag. Incremental ramp-weight penalties resulting from higher induced drag derived from previous sensitivity data are also shown in Figure 64. The results show that configuration B offers the best compromise to achieving the desired cruise performance with only a small ramp weight penalty. In addition, with configuration B the inboard panels of the aft wing can be used as vertical stabilizers, as in a vee tail. Hence, configuration B was selected as the alternate configuration for further study.

2.2.2 ANALYSIS OF ALTERNATE CONFIGURATION

The principal differences between the interim configuration, established at the end of the Phase I studies, and the alternate configuration are shown in Figure 65. The aft wing was moved rearwards on the fuselage to offset some of the reduction in the effective lift-curve slope and resulting forward shift in neutral point.

2.2.2.1 Cruise

Results from lifting surface theory computation are presented in Figure 66 for the alternate configuration at a cruise speed Mach number of 0.95 and are compared with those of the interim configuration. Some of the apparent reductions in the stability contribution of the aft wing are due to a higher downwash effect on the inner panel. The ratio of the lift-curve slopes for the two wings is reduced from about 1.20 for the interim configuration to 0.71 for the alternate configuration. Therefore, the condition for equal lift coefficients at cruise would have to be met by a decalage angle increase, but off-design lift conditions would be less than satisfactory due to higher induced drag from the wing-lift differential. The variation of lift-curve slope across the span for the alternate configuration is presented in Figure 67. For the calculated and

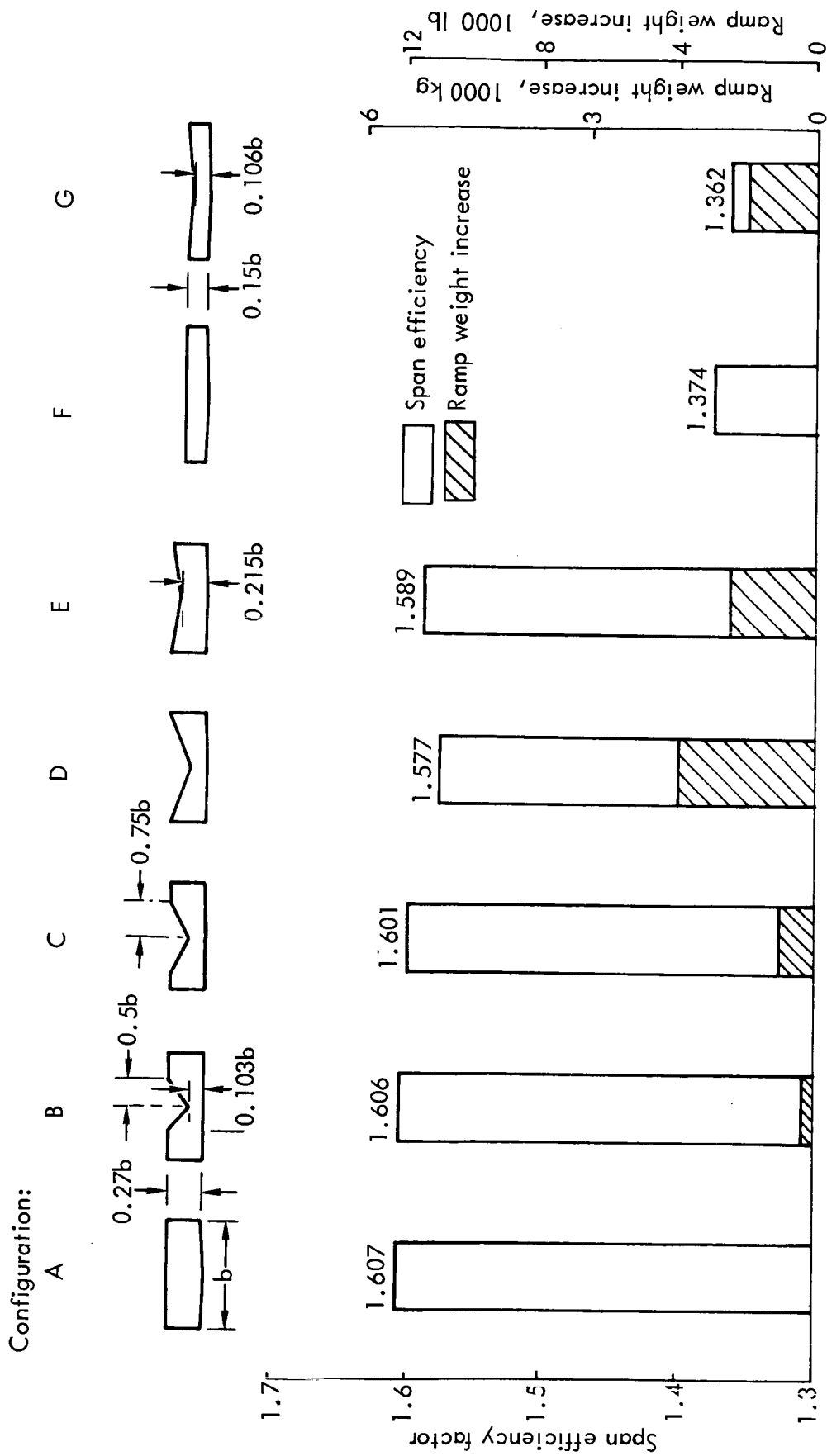


Figure 64. Comparison of alternate configurations.

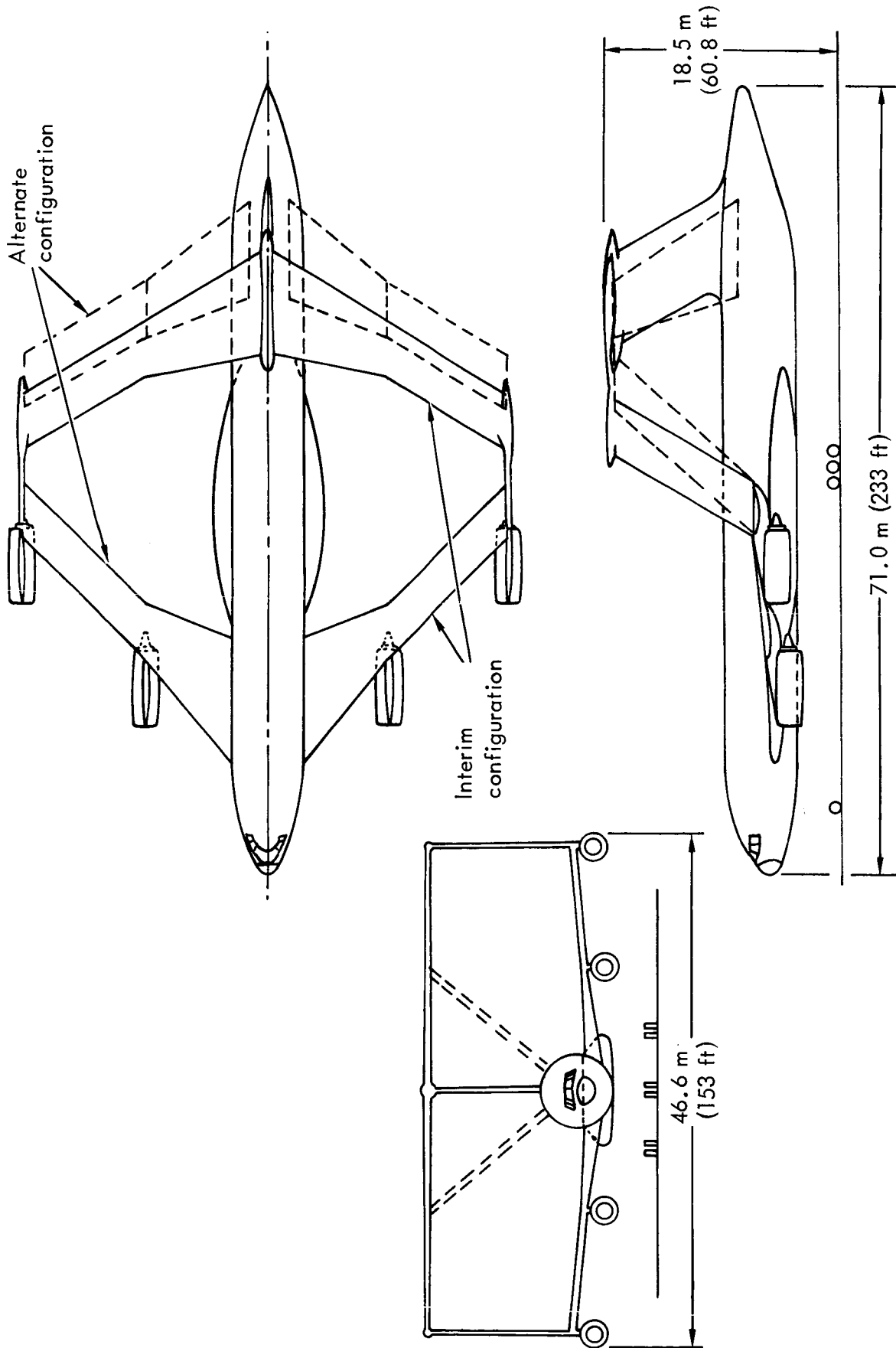
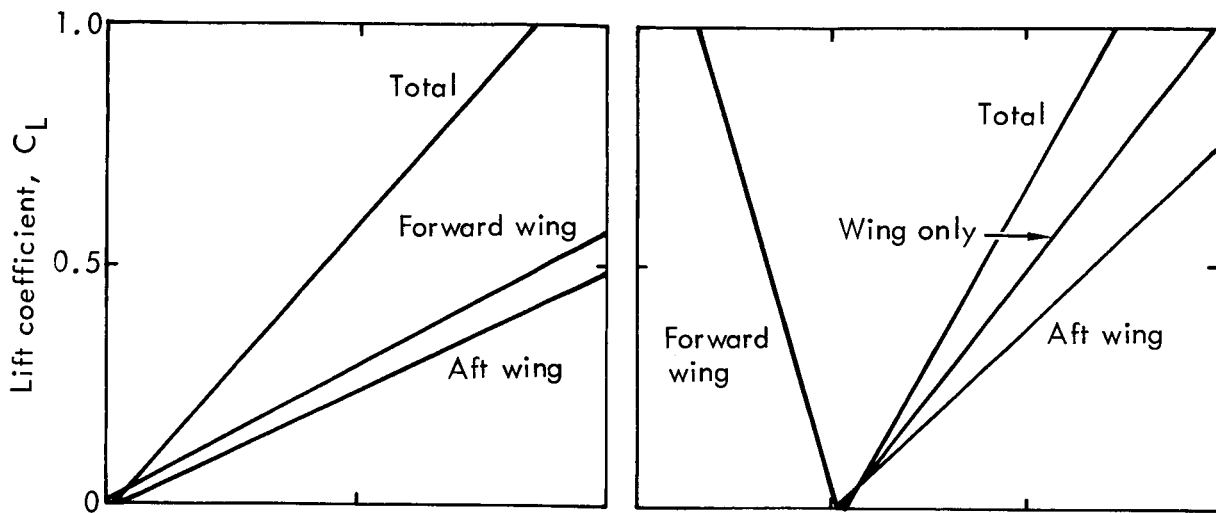
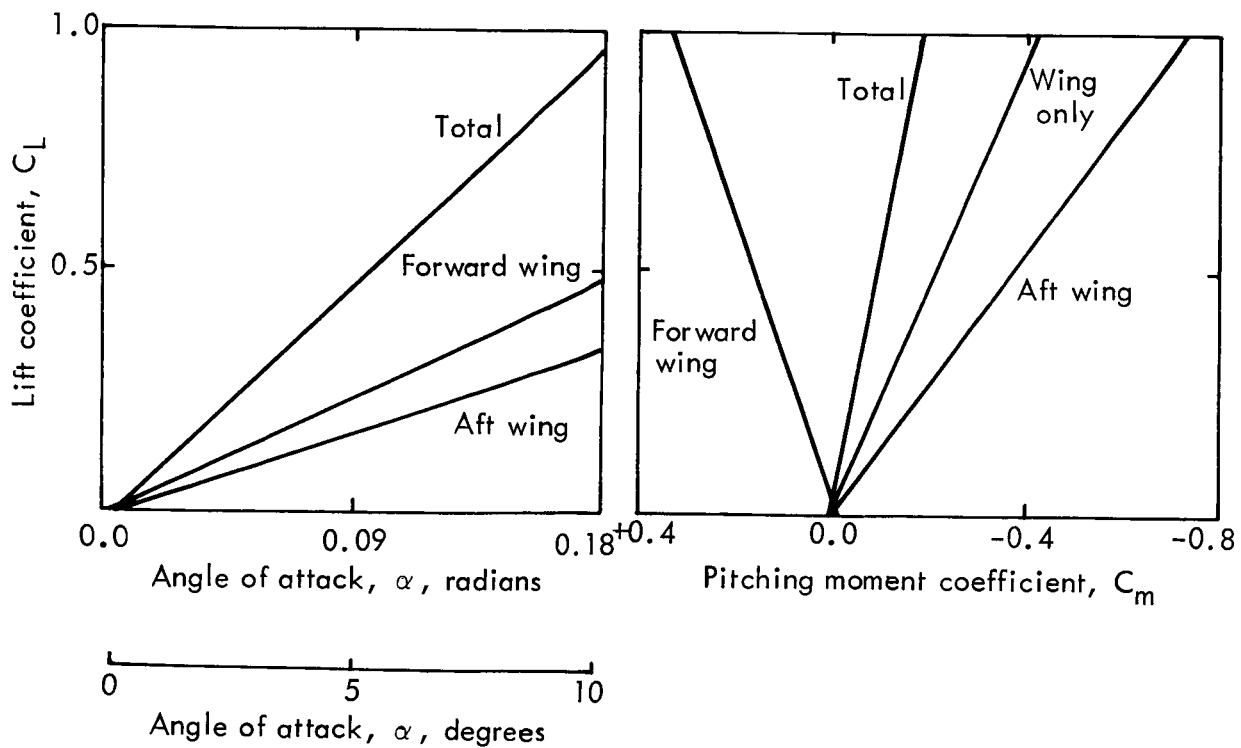


Figure 65. Comparison of interim and alternate configurations.



a) Interim configuration.



b) Alternate configuration.

Figure 66. Lift and pitching moments for alternate and interim configurations at $M = 0.95$.

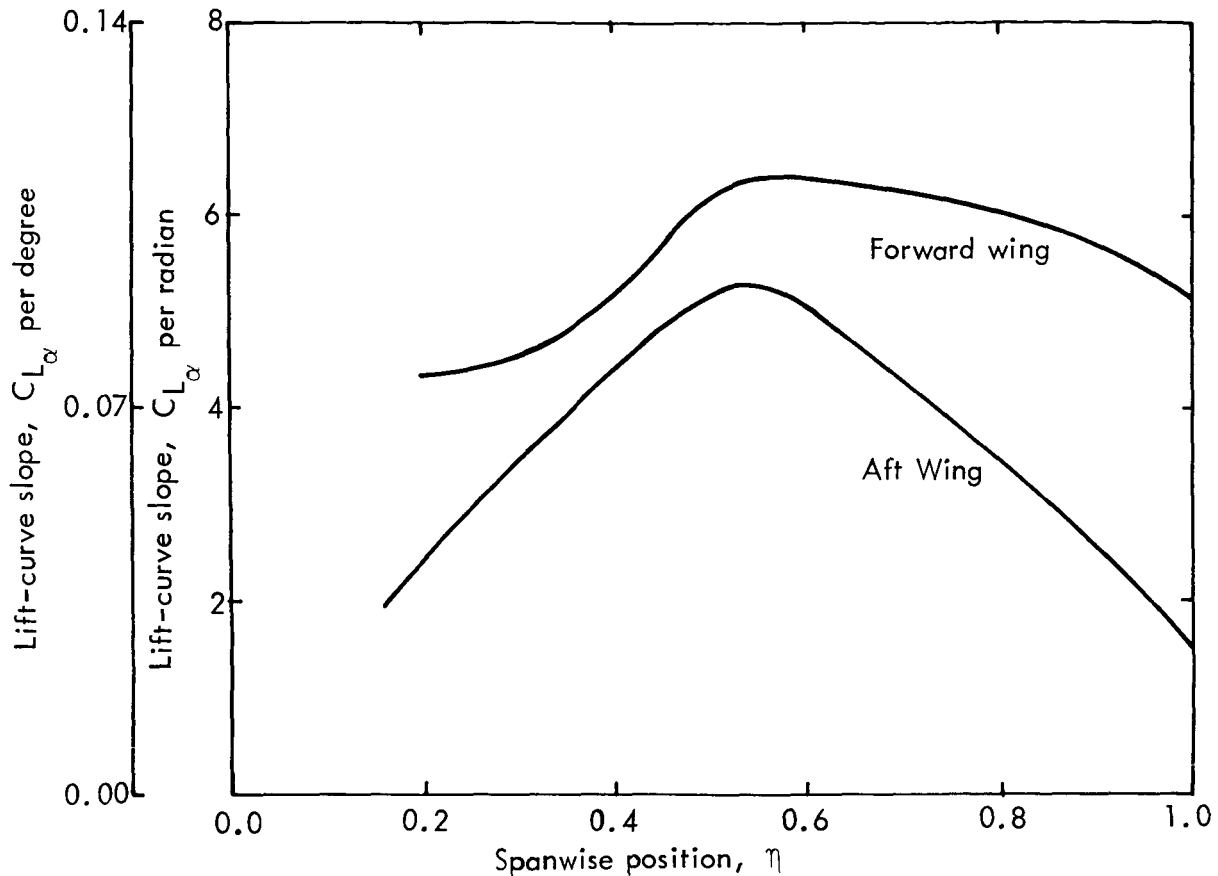


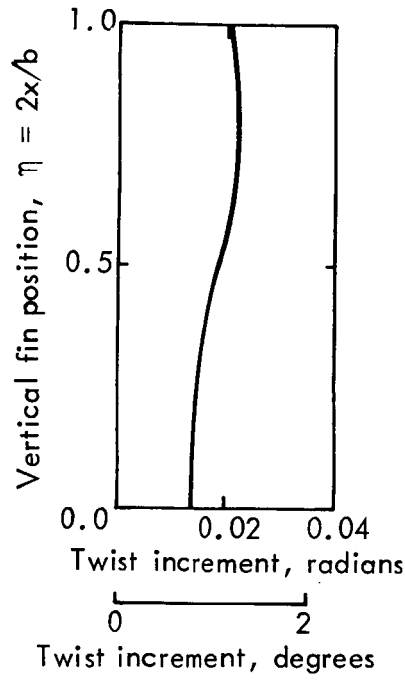
Figure 67. Lift-curve-slope distribution for alternate configuration.

optimum spanload distributions to meet the cruise drag requirement, the amount of wing and end-fin twist distributions shown in Figure 68 are required.

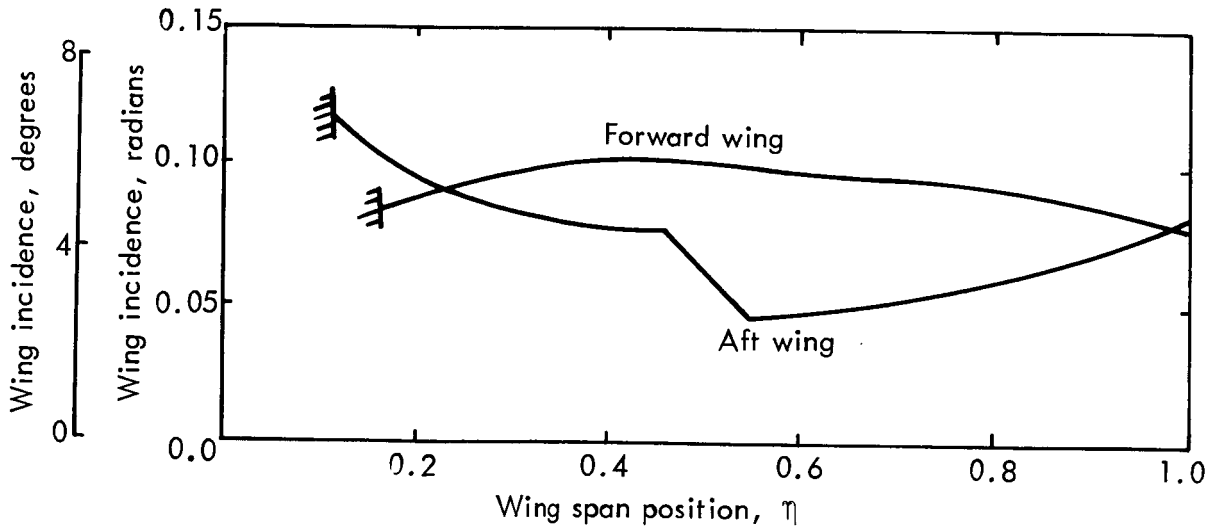
2.2.2.2 High Lift

The basic data sources used in Phase I of the program were utilized in estimating high-lift performance of the alternate configuration. Figure 69 presents some typical lift and pitching moment results with various fore- and aft-wing flap settings. It was found that the optimum flap settings for take-off, trimming with 3-percent static margin, were 0.61 rad (35°)/0.35 rad (20°)/0.44 rad (25°) on the forward wing and 0 rad (deg)/0.17 rad (10°)/0.17 rad (10°) on the aft wing. Corresponding settings for landing were 0.79 rad (45°)/0.70 rad (40°)/0.44 rad (25°) and 0.35 rad (20°)/0.35 rad (20°)/0.35 rad (20°). Full-scale maximum lift coefficient levels are comparable to those of the interim configuration if the forward wing slat is increased to a full span configuration.

The induced drag during climb-out and approach conditions was evaluated through the lifting surface and span efficiency programs described in Phase I. Figures 70 and



a) End-fin twist distribution, front view.



b) Wing twist distribution

Figure 68. Wing and end-fin twist requirements.

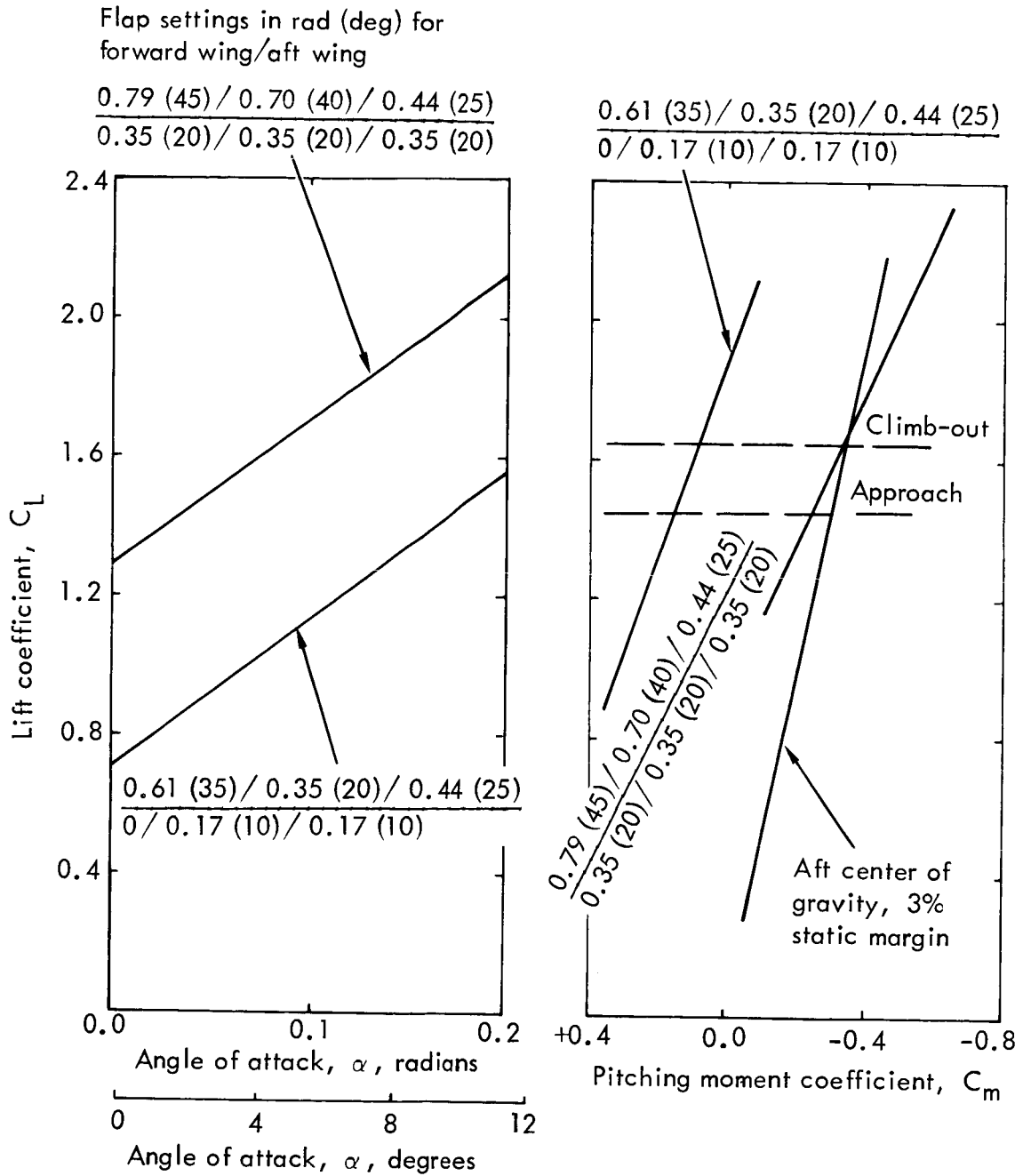


Figure 69. Effect of flaps down on lift and pitch characteristics of alternate configuration.

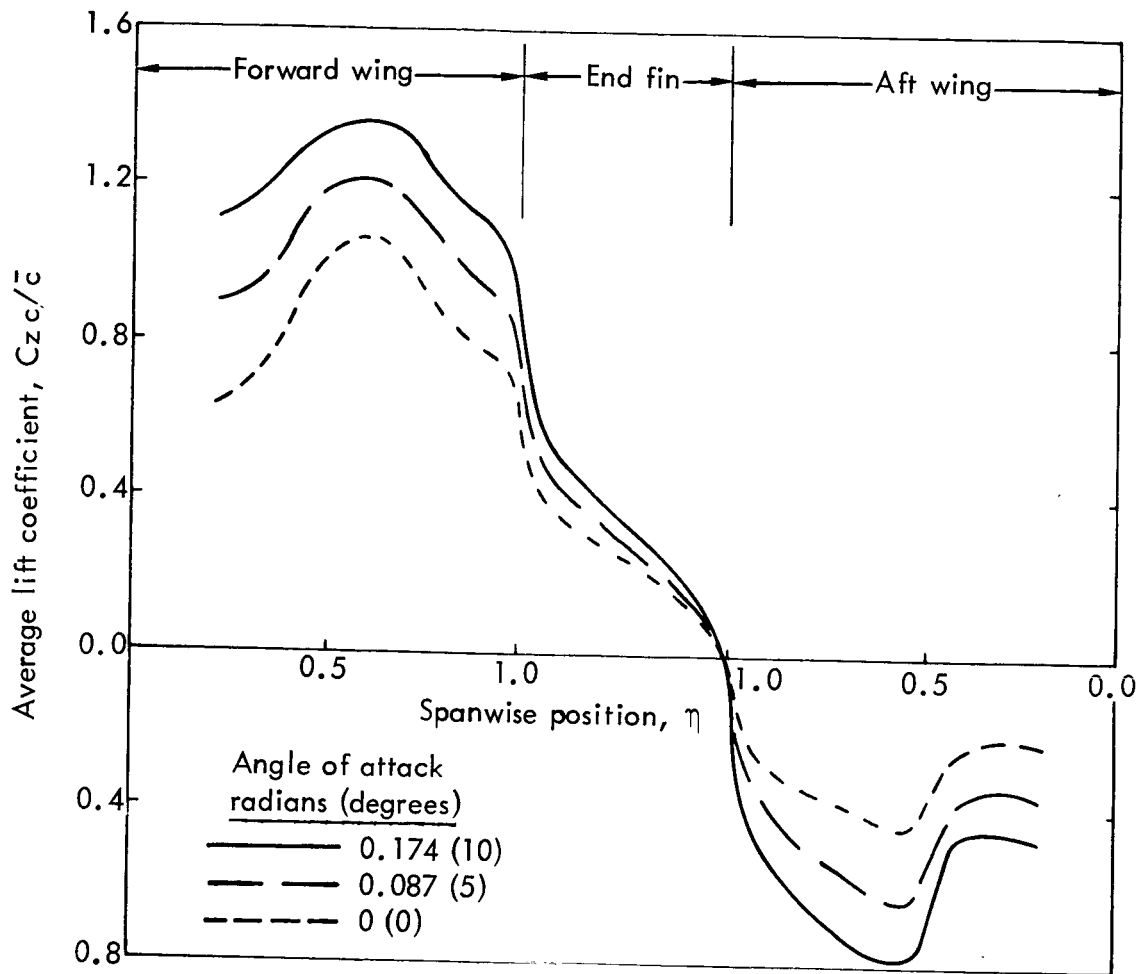


Figure 70. Span load distribution for alternate configuration.
 Forward wing flaps setting of 0.44 rad (25°)/ 0.70 rad (40°)/ 0.44 rad (25°)
 and aft wing flaps setting of 0.35 rad (20°)/ 0.35 rad (20°)/ 0.35 rad (20°).

71 present the effects on span-load distributions of different forward-wing flap arrangements. Span efficiency factors calculated from these and other loading cases are shown in Figure 72. The apparent benefits of increasing inner-flap segment angles, as evident on these curves, is caused primarily by a more uniform load distribution over the wing.

High-lift basic drag data and methodology were introduced in Section 3.1.2.4 of Phase I. The reference data are for flap-span ratios between 10 percent and 80 percent of the wing semi-span on a 0.73 rad (42°) swept wing. These are modified for part-span effects by using Reference 10 methods and by assuming that each flap segment drag increment can be obtained independently before summation of the total. This approach was validated through correlation of estimates with test data for a varying spanwise flap angle. Incremental values of the zero-lift drag coefficient for the forward wing with flaps were estimated for an average value of fuselage semi-width/wing chord of 0.75. (See Figure 32.)

2.2.2.3 Lateral/Directional Stability

Estimates of the lateral and directional stability derivatives for the alternate configuration were made using lifting-surface computations. This procedure included integration of the individual wing panel loads data for unit sideslip angle. Since the computer program did not have the logic for representing a finite fuselage thickness, the levels of stability are somewhat higher than expected from a complete configuration. Table XII gives a breakdown of the change in side force with change in sideslip angle β , $C_{y\beta}$; the change in yawing moment with change in sideslip angle, $C_{n\beta}$; and the change in rolling moment with change in sideslip angle, $C_{l\beta}$, with a comparison of C-5 total configuration values.

TABLE XII. LATERAL AND DIRECTIONAL STABILITY PARAMETERS

Derivative Per Deg.	Biplane					C-5
	Forward Wing	Tip Fin	Outer Aft Wing	V Panels	Total	
$C_{y\beta}$	0	0.0114	0	0.0075	0.0191	0.020
$C_{n\beta}$	0	0.0028	0	0.0065	0.0093	0.0025
$C_{l\beta}$	0.0005	0.0037	-0.0028	0.0041	0.0055	0.0025

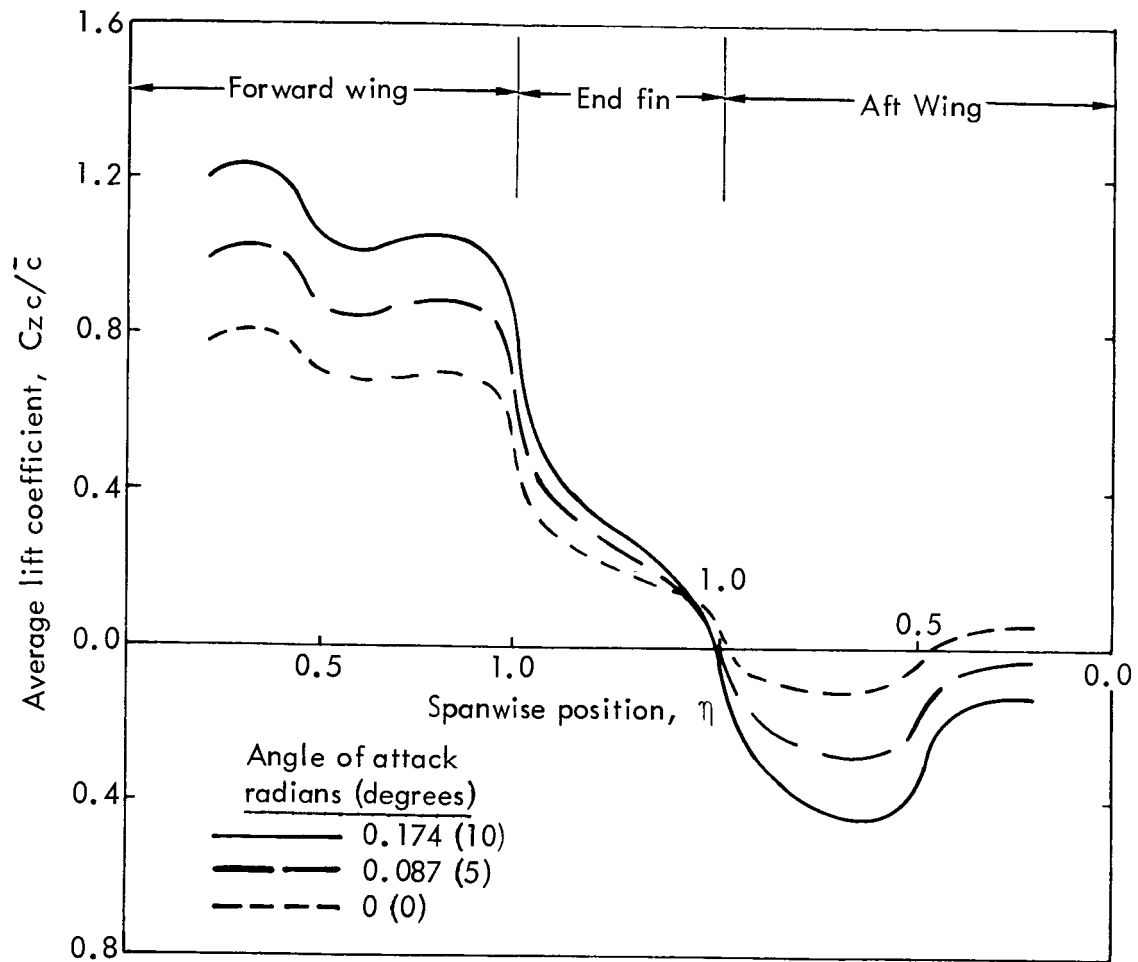


Figure 71. Span load distribution for alternate configuration. Forward wing flaps setting of 0.61 rad (35°)/ 0.35 rad (20°)/ 0.44 rad (25°) and aft wing flaps setting of 0 rad (0°)/ 0.17 rad (10°)/ 0.17 rad (10°).

Flaps setting, radians (degrees)
Forward wing; aft wing

- 0.44 (25) / 0.70 (40) / 0.44 (25); 0.35 (20) / 0.35 (20) / 0.35 (20)
- 0.61 (35) / 0.35 (20) / 0.44 (25); 0.17 (10) / 0.35 (20) / 0.35 (20)
- 0.79 (45) / 0.70 (40) / 0.44 (25); 0.35 (20) / 0.35 (20) / 0.35 (20)
- 0.61 (35) / 0.35 (20) / 0.44 (25); 0 / 0.17 (10) / 0.17 (10)

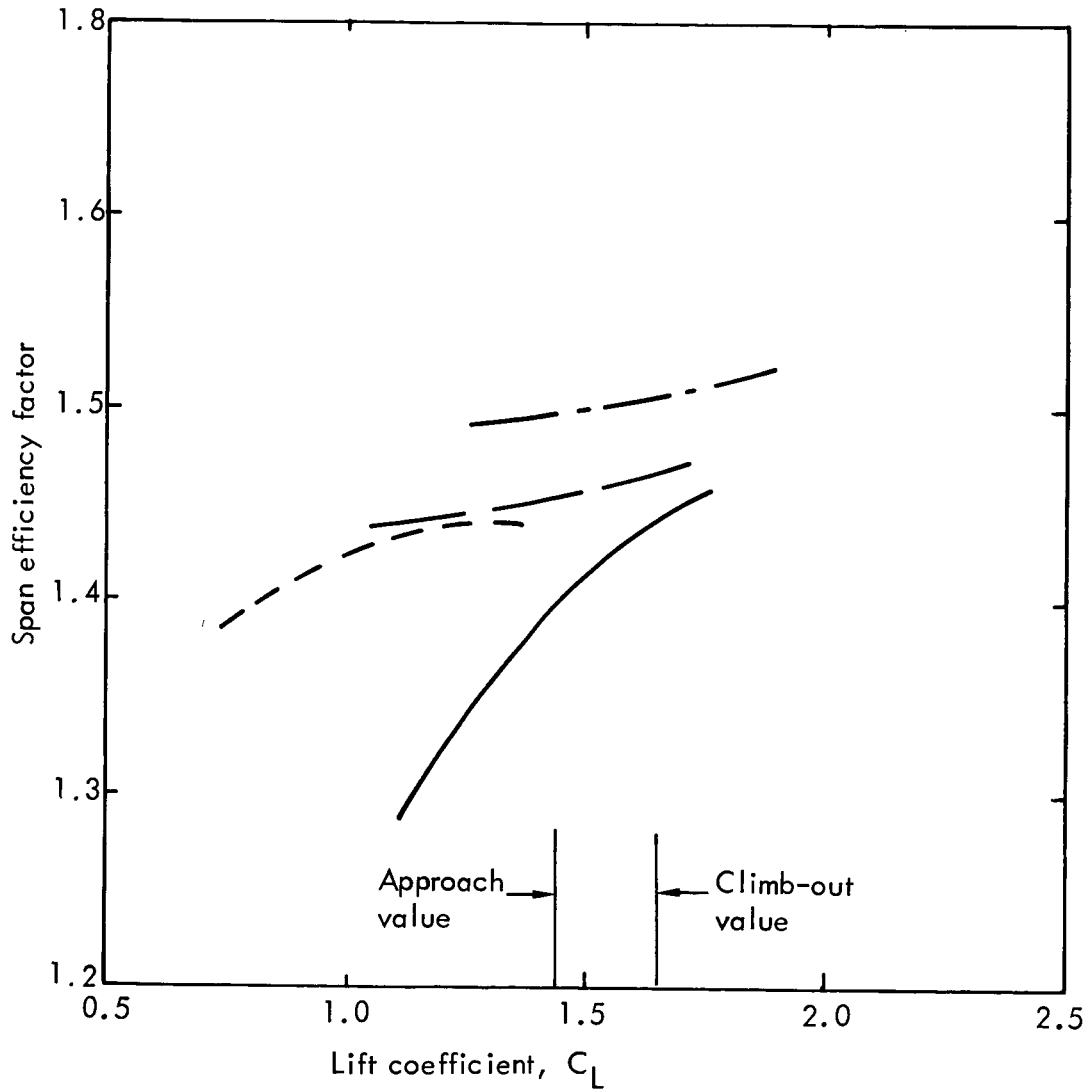


Figure 72. Flaps down span efficiency for alternate configuration.

The results show that the biplane configuration has inherent static-stability levels comparable to, or greater than, a conventional monoplane. Ratios of $C_{l_{\beta}}/C_{n_{\beta}}$ can be shown to be within a satisfactory range to avoid Dutch-roll instability and a tolerable spiral instability level.

3.0 STRUCTURAL ANALYSIS

Analyses were performed to determine the strength-designed structure for the alternate configuration selected in Section 2.2.1 and pictured in Figure 45 as design number 6. Subsequently, revisions were made in the structural design to improve the flutter characteristics while attempting to minimize weight increases for the airplane. The three sections that follow include discussions of the method of structural analysis, the flutter limitations and problem areas, and the weight estimates for the alternate configuration.

3.1 STRENGTH

A structural FAMAS model was developed for the alternate configuration, and structural sizing and analyses were conducted in the same manner as on the previous configurations. After the results of the initial sizing were evaluated from a flutter standpoint, arbitrary increases in the equivalent cover thicknesses were made in order to assess these effects on the flutter speed. This additional box material on the aft wing resulted in a 50-percent increase in average material thickness above that required for strength. The modified material distribution was then re-input into the FAMAS program to derive internal loads and element influence coefficients.

3.2 WEIGHTS

The resulting material distribution, discussed in Section 3.1, for the alternate configuration was used manually to estimate the weight for the forward and aft wings and the tip struts. The remaining aircraft weight items were assumed to be the same as for the interim configuration except for mission fuel. Since the gross weight of the interim configuration was used as the design gross weight in these structural analyses, fuel was decreased to compensate for the zero-fuel weight increase.

Table XIII presents the estimated weight breakdown derived for the alternate configuration along with the distribution factors for allocating the component weights to each major mass item. For each of these major mass items, the weight was distributed and allocated to each node point for use in the flutter analysis. The zero-fuel weight for this alternate configuration is 4289 kg (9456 lb) above the zero-fuel weight reported for the interim configuration. The wing weights for the interim configuration were parametrically derived and were suspiciously low. As indicated previously, design parameter sensitivity in the wing weight relationships, used in the weight parameteric program, was based upon analyses of three closely-related configurations and was limited due to the scope of the Phase I studies.

The forward wing for the alternate configuration is identical to the forward wing of the interim configuration except for a wider wing box. Results of a FAMAS analysis reflected a forward-wing weight that was

TABLE XIII. ALTERNATE CONFIGURATION WEIGHT DISTRIBUTION SUMMARY

Item	Total weight		Weight distribution factors				
	kg	lb	Forward wing	Tip struts	Aft wing	Fuselage	Total
Forward wing	9 511	20 969	0.86			0.14	1.00
Aft wing	13 998	30 860			1.00		1.00
Tip fins	3 343	7 369		1.00			1.00
Vertical tail	0	0					
Fuselage	26 748	58 970				1.00	1.00
Landing gear	11 898	26 231				*0.12/*0.88	1.00
Nacelles/pylons	9 358	20 631	*1.00				1.00
Propulsion system	17 811	39 266	*0.91/0.05		0.04		1.00
Aux. power system	638	1 406				1.00	1.00
Surface controls	4 620	10 186	0.25	0.04	0.33	0.38	1.00
Instruments	602	1 327	0.05	0.01	0.06	0.88	1.00
Hydr. & pneu.	1 672	3 686	*0.02/0.06	0.02	0.08	0.82	1.00
Electrical	2 545	5 611	0.06			0.94	1.00
Avionics	918	2 024				1.00	1.00
Furnishings	12 393	27 321	0.03			0.97	1.00
Air conditioning	3 067	6 762	0.03	0.01	0.03	0.93	1.00
Weight empty	119 122	262 619	*0.21/0.09	0.03	0.14	*0.10/0.43	1.00
Operating equip.	12 804	28 229	0.01		0.01	0.98	1.00
Passenger payload	38 465	84 800				1.00	1.00
Cargo payload	0	0					
Zero fuel weight	170 391	375 648	*0.15/0.06	0.02	0.10	*0.07/0.60	1.00
Fuel	131 201	289 248	0.51		0.49		1.00
Des. gross weight	301 592	664 896	*0.09/0.26	0.012	0.270	*0.04/0.34	1.00

*Concentrated weight items

60.6 percent heavier than that obtained from the parametric results for the interim configuration. This difference was investigated and 38.5 percent was determined to be due to parametric variations which were distributed as follows:

- (1) 15.7 percent due to box geometry.
- (2) 13.0 percent due to an error in the forward-wing lift ratio used for the interim configuration (1-g lift ratio of 0.5 was used instead of 2.5-g lift ratio of 0.56).
- (3) 9.8 percent due to specifying tip-strut fuel for Phase I parametric analysis while the alternate configuration does not use tip-strut fuel. (Tip-strut fuel was determined inadvisable because of the fuel pressure and other undesirable problems.)

The remaining 22.1-percent increment can be partially attributed to internal load redistributions caused by the stiffer aft wing.

Adjusting the forward-wing weight for these parameters would result in a modified interim configuration parametric wing weight of 8205 kg (18 088 lb) which is the 38.5-percent increase just explained. As described in the flutter analysis section which follows, the alternate configuration does not improve the flutter problems. Therefore, the parametric weight program was not changed to reflect this configuration.

3.3 FLUTTER ANALYSIS

Flutter analyses of the alternate configuration were conducted using the same methods described earlier. Modified strip-theory aerodynamic coefficients were used. The stiffness and mass data used represented an approximate strength design on all of the structure except the aft wing, which was stiffened by approximately 50 percent over the strength design in an effort to increase the flutter speeds.

The results of the Phase I and II analyses are summarized in Table XIV. In spite of the reconfiguration and aft-wing stiffening, the flutter speeds for the alternate configuration remained unsatisfactorily low. The critical antisymmetric instability occurred at 130 m/sec (252 KEAS) and 1.06 Hz, and the symmetric occurred at 150 m/sec (292 KEAS) and 0.48 Hz. Although these speeds are somewhat lower than those predicted for the interim configuration, the results are not directly comparable. As previously mentioned, the stiffness and mass data used in the flutter analysis of the interim configuration represented a level of strength in excess of that required by the design loads. If the structural sizing had been further refined, somewhat lower flutter speeds would have resulted. In any case,

TABLE XIV. SUMMARY OF FLUTTER ANALYSIS RESULTS.

Configuration number	Symmetric		Antisymmetric	
	Speed m/sec (KEAS)	Frequency Hz	Speed m/sec (KEAS)	Frequency Hz
1	163 (316)	0.48	144 (279)	0.83
4	190 (370)	0.76	179 (348)	1.53
5	155 (302)	0.62	148 (287)	1.15
5 *	124 (241)	0.52	133 (259)	1.14
6	150 (292)	0.48	130 (252)	1.06

- Computations based on doublet lattice aerodynamics. All other computations based on modified strip theory aerodynamics with wing lift-curve-slope distributions modified to agree with steady lifting surface theory.

all of the configurations analyzed exhibited such low flutter speeds that excessive amounts of structural weight would be required to raise them to the required 270 m/sec (525 KEAS).

3.4 FUNDAMENTAL FLUTTER PHENOMENA

The necessarily limited scope of this study did not permit a thorough, systematic investigation of the fundamental flutter phenomena exhibited by the configurations analyzed. These phenomena, however, appear to be inherent to this configuration type. No static aeroelastic or elastic dynamic-stability analyses were made, but there is some evidence to suggest that the flutter phenomena might actually be dynamic manifestations of static divergence or a highly modified short period instability.

As a further attempt to understand the basic mechanisms involved, calculations were made of the flutter modes and the associated "energy flow" between the airstream and the airframe during flutter. The calculations were made

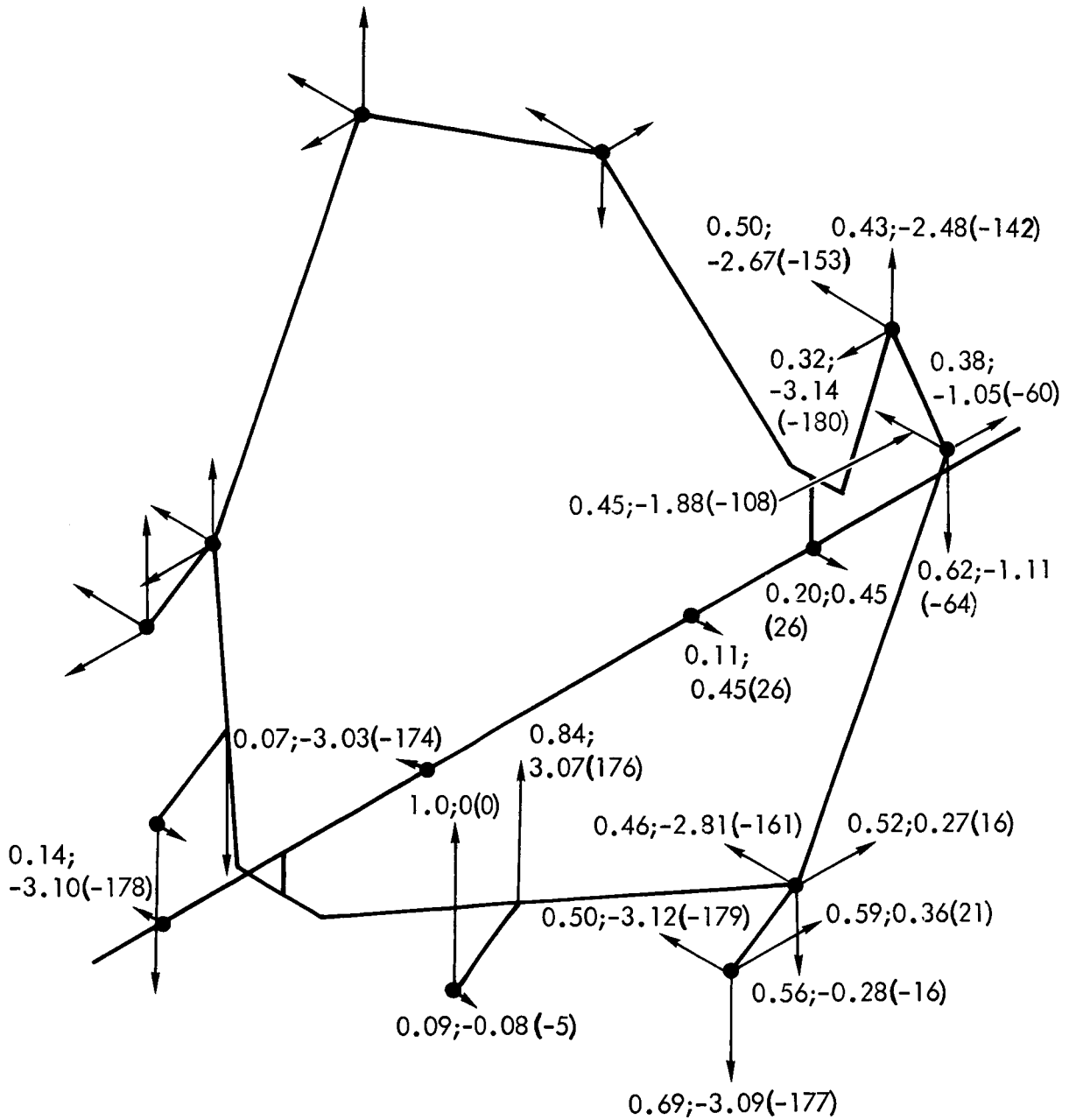


Figure 73. Critical antisymmetric flutter mode for alternate configuration. Values with vectors are relative flutter amplitude and phase angle in radians (degrees).

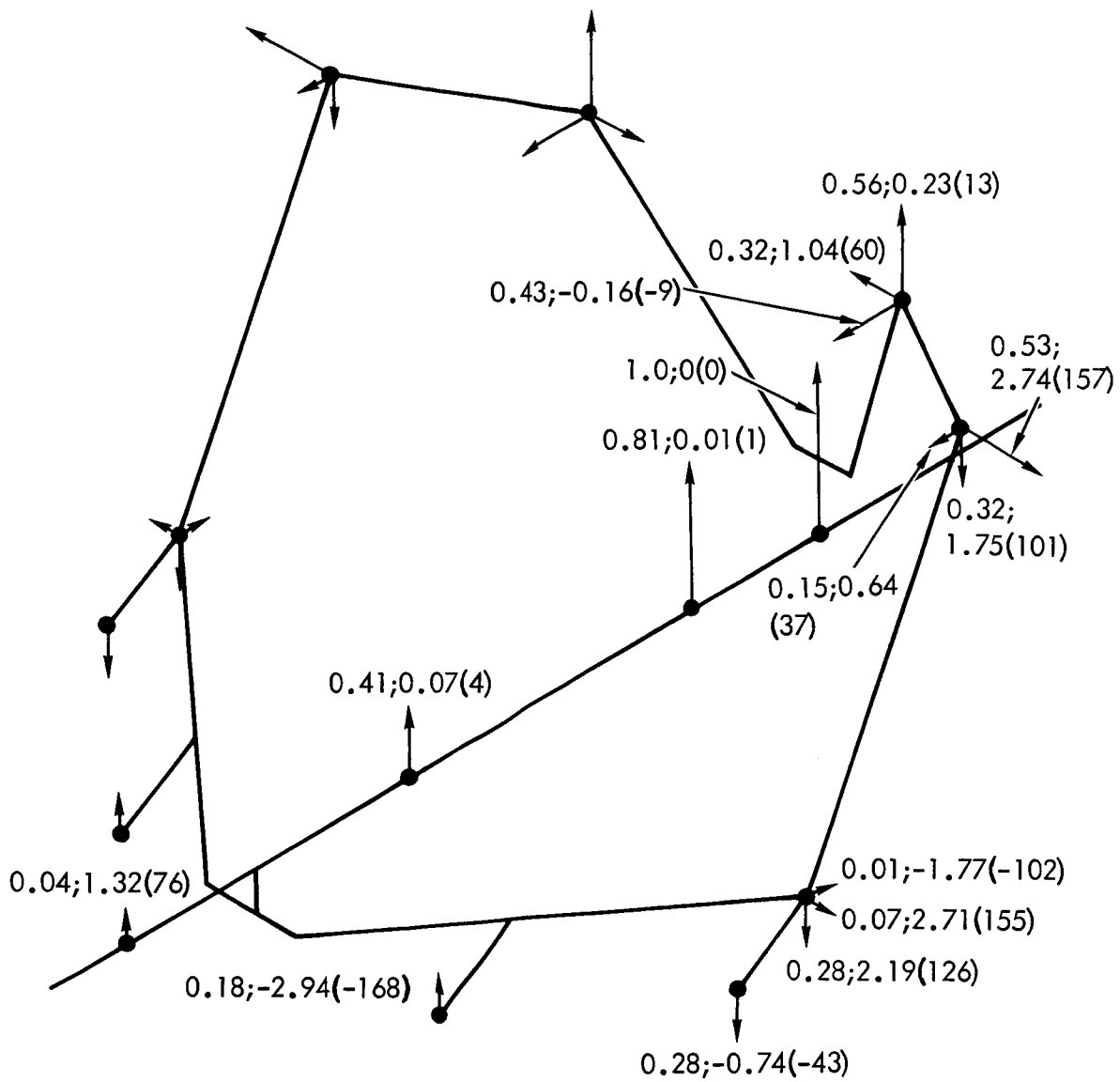
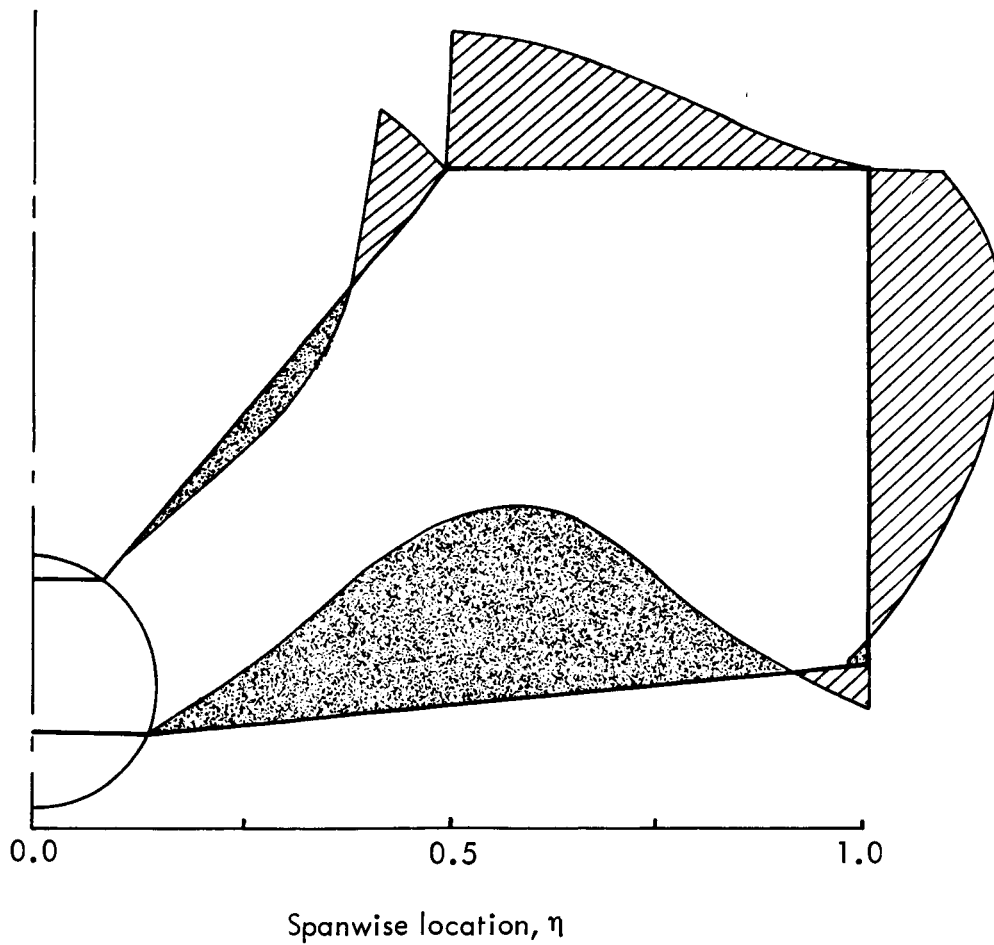
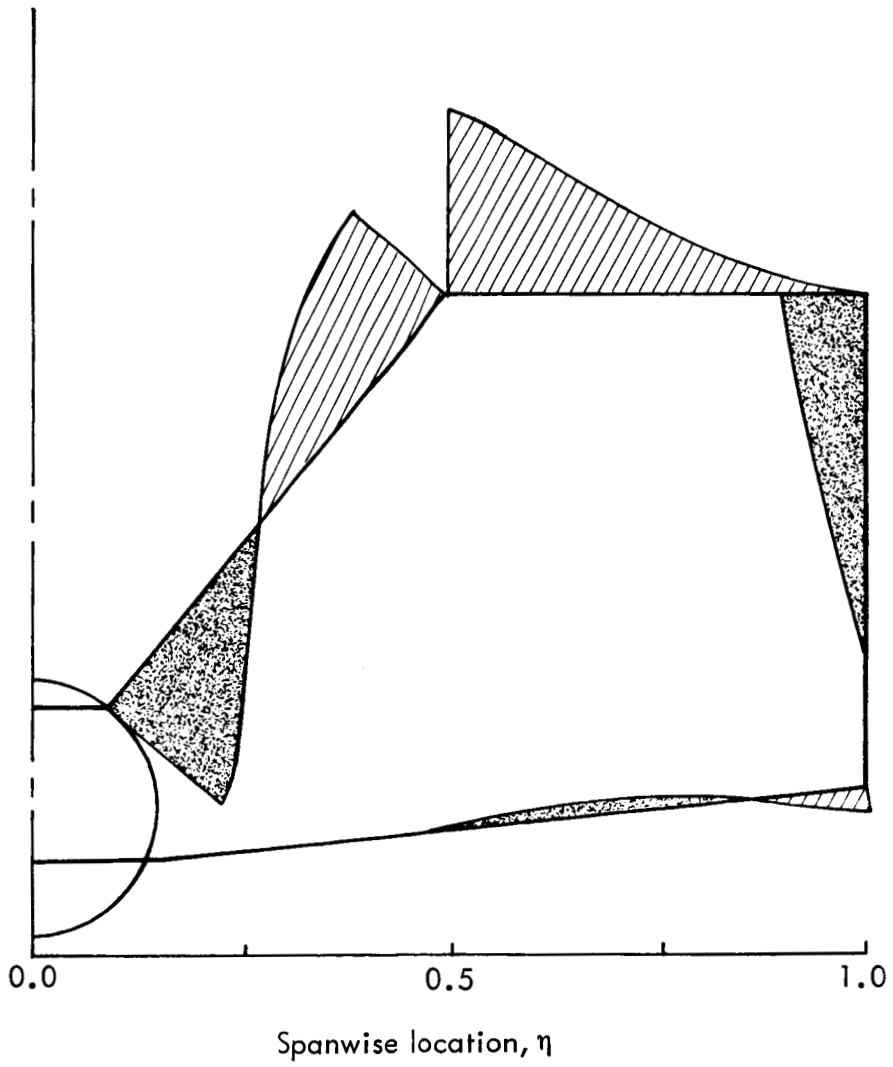


Figure 74. Critical symmetric flutter mode for alternate configuration. Values with vectors are relative amplitude and phase angle in radians (degrees).



Front view

Figure 75. Energy flow during antisymmetric flutter for alternate configuration.



Front view

Figure 76. Energy flow during symmetric flutter for alternate configuration.

for the alternate configuration and were based on modified strip-theory aerodynamic coefficients. Depictions of the complex flutter vectors are shown in Figures 73 and 74. The vectors shown in Figure 73 indicate that antisymmetric flutter consists primarily of antisymmetric vertical and fore-and-aft bending of the forward and aft wings. Thus, the character of the antisymmetric flutter mode for the alternate configuration has changed considerably from that of Configuration 5, even though the flutter speed is about the same. The symmetric flutter mode, shown in Figure 74, is similar to that predicted for Configuration 5; namely, fuselage pitching and plunging together with aft-wing vertical bending.

Diagrams depicting the spanwise distribution of energy absorption and dissipation associated with the antisymmetric and symmetric flutter modes are shown in Figures 75 and 76. The figures show the conditions at the flutter threshold when the absorbed and dissipated energy are in balance and the net energy flow is zero. At higher speeds, the absorbed energy increases and/or the dissipated energy decreases to produce net energy absorption. Figure 75 shows that the principal areas of energy absorption in the antisymmetric mode are the tip fins and the outer 60 percent of the aft wing, whereas the major area of dissipation is the forward wing. Figure 76 shows that the principal area of absorption in the symmetric mode is the outer 75 percent of the aft wing, while the remainder of the aft wing and the tip fin are dissipating energy. The forward wing is not participating in the symmetric mode.

Recent studies by E. Nissim in Reference 16 indicate that the major energy absorption areas on an airframe undergoing flutter are the most efficient areas in which to locate control surfaces for active flutter suppression. By proper activation of these surfaces, the energy absorption areas can be made to dissipate energy and thus suppress the instability. Thus, it is reasonable to assume that active control surfaces located on the outer 75 percent of the aft wing and on the tip fins could provide significant increases in the symmetric and antisymmetric flutter speeds.

4.0 COMPARISON WITH ATT M = 0.95 CONFIGURATION

Descriptions have been presented in previous sections of the transonic biplane configurations having payload, range, and airport performance comparable to those evolved from fairly detailed studies in Reference 4. As indicated previously, the weights of the biplane configuration are similar to those of monoplane configurations designed to accomplish the same mission.

While the biplane arrangement results in substantial reductions in drag due to lift, the parametric airplane design studies in this report show that minimum airplane gross weights occur at aspect ratios lower than those for a monoplane. In fact, cruise lift-to-drag ratios for the optimum biplane configuration in these parametric studies (aspect ratio = 4.4) are essentially equal to those of the monoplane.

At low speeds with flaps deployed for takeoff or landing, the lift-to-drag ratio is also similar to that for the monoplane so that community noise levels can be expected to be comparable to the monoplane.

Area distributions developed for several biplane configurations have shown that satisfactory transonic drag-rise characteristics should be obtained for configurations having cylindrical fuselage mid-sections. Greater flexibility in interior arrangements has been shown by the ATT studies as a result of avoiding fuselage shaping for area-rule tailoring.

From an operational standpoint, some advantage in required ramp space might accrue from the shorter span of the biplane, but any such benefits would be compensated by more difficult access to fuel system and control system components in the upper wing.

5.0 RESEARCH AND TECHNOLOGY RECOMMENDATIONS

Results of the current study have indicated that if computer-predicted flutter instabilities can be overcome, it may be possible to develop a transonic biplane with the same gross weight and fuel economy as a monoplane designed for the same payload/range mission. It must be recognized that both the potential performance benefits and the flutter instabilities are highly dependent upon configuration geometry. Consequently, aerodynamic configurations suitable for slower-speed missions might eliminate both the weight and flutter problems shown by this study. Further effort on applications of the biplane concept, therefore, requires studies of both mission applications and the detailed technology development for weight reduction and flutter elimination.

Because of their importance in determining the feasibility of the transonic biplane concept, the flutter phenomena encountered during this study should be further investigated. A combined analytical and experimental approach consisting of the following tasks is recommended.

- o Experimental verification of flutter analysis results by means of correlated analysis and low-speed wind-tunnel flutter-model tests of a representative configuration.
- o Determination of the flutter-sensitive features of the biplane concept by flutter analyses and/or flutter model tests of a series of radically reconfigured designs.
- o Investigation of the benefits of active flutter suppression by the synthesis and analysis of a conceptual system for a representative configuration.
- o Determination of the effects of compressibility on the supercritical lifting surfaces by transonic wind-tunnel flutter-model tests of a viable configuration derived from the previous tasks.

Results of this study have necessarily been based on small amounts of experimental data supplemented by analytical determinations of aerodynamic and structural characteristics. For cases where studies of transonic biplane applications show substantial benefits in mission effectiveness, the following experimental studies are required to provide a proper basis for further development.

- o Low speed wind tunnel testing is required to confirm high-lift effectiveness estimates and to demonstrate stall inception and progression.
- o Transonic wind tunnel testing should be conducted to confirm overall area distribution acceptability with cylindrical fuselages and to develop aerodynamic shaping of the many surface junctures of the biplane configuration.

- o Static load testing of simplified structural models should be accomplished to verify computer simulations of the redundant structural arrangement.

Studies into potential benefits in other applications would appear warranted. Applications for which induced drag reductions are especially significant should be emphasized in these studies. Some potential applications are:

- o High altitude, long endurance aircraft - High lift coefficients, low wing loadings and relatively high Mach numbers accompanied by high lift-to-drag ratios and low structural weight are all requirements for such aircraft because of the low density environment in which they must operate. The low induced drag of a transonic biplane configuration could produce a pay-off for such missions.
- o Highly maneuverable transonic fighter - Low induced drag is obviously beneficial to minimize speed loss during maneuvers. Studies by the Lockheed-California Co. have concluded, however, that net benefits are minimal for this application.
- o Low supersonic cruise aircraft - The relatively greater longitudinal length of the lift distribution of the transonic biplane results in substantially lower wave drag than other wing arrangements having the same aspect ratio. Optimization of configurations to achieve the benefits of combined wave drag and induced drag reduction should be studied.

REFERENCES

1. Von Karman, T. and Burgers, J. M., "General Aerodynamics Theory-Perfect Fluids" in Vol. II of AERODYNAMIC THEORY, (Edited by Durand, W. F.)
2. Miranda, L. R., "Boxplane Configuration - Conceptual Analysis and Initial Experimental Verification", Lockheed-California Company Report, LR 25180, March 1972.
3. Cahill, J. F. and Stead, D. H., "Preliminary Investigation at Subsonic and Transonic Speeds and the Aerodynamic Characteristics of a Biplane Composed of a Sweptback and a Sweptforward Wing Joined at the Tips," NACA RM L53L24b, 1954.
4. Lange, R. H. , et al, "Study of the Application of Advanced Technologies to Long-Range Transport Aircraft", NASA CR-112088, Lockheed-Georgia Company, 1972.
5. Munk, M. M., "The Minimum Induced Drag of Airfoils", NACA Report No. 121, 1921.
6. Rethorst, S., Saffman, P., and Fujita, T., "Induced Drag Elimination on Subsonic Aircraft", Technical Report AFFDL-TR-66-115, December 1966.
7. Blackwell, J., "A Finite-Step Method for Calculation of Theoretical Load Distributions for Arbitrary Lifting - Surface Arrangements at Subsonic Speeds", NASA TND 5335, July 1969.
8. Palme, H. O., "Summary of Wind Tunnel Data for High-Lift Devices on Swept Wings", SAAB TN 16, April 1953.
9. USAF Stability and Control DATCOM.
10. RAe.S Data Sheets, Flaps 01.01.07.
11. Wimpress, J. K., "Predicting the Low Speed Stall Characteristics of the Boeing 747", AGARD Fluid Dynamic of Aircraft Stalling, November 1972.
12. Schuringa, T., "Aerodynamics of Wing Stall of the Fokker F-28", AGARD Fluid Dynamics of Aircraft Stalling, November 1972.
13. RAe.S Data Sheets, Flaps 02.01.06.
14. RAe.S Data Sheets, Flaps 02.01.07.

15. "Airworthiness Standards; Transport Category Airplanes", Federal Aviation Regulations Part 25.
16. Nissim, E., "Flutter Suppression Using Active Controls Based on the Concept of Aerodynamic Energy", NASA TN D6199, March 1971.